CHEMICAL REVIEWS

Review

Cite This: *Chem. Rev.* 2019, 119, 7444−7477

pubs.acs.org/CR

Perovskites for Next-Generation Optical Sources

Li Na Quan,[†] Barry P. Rand,[‡] Richard H. Friend,[§] Subodh Gautam Mhaisalkar,[∥] Tae-Woo Lee,[⊥] and Edward H. Sargent*,[†]

[†]Department of Electrical and Computer Engineering, University of Toronto, 10 King's College Road, Toronto, Ontario M5S 3G4, Canada

[‡]Department of Electrical Engineering and Andlinger Center for Energy and the Environment, Princeton University, Princeton, New Jersey 08544, United States

[§]Cavendish Laboratory, University of Cambridge, JJ Thomson Avenue, Cambridge CB3 0HE, United Kingdom

[∥]Energy Research Institute, Nanyang Technological University, Research Techno Plaza, X-Frontier Block, Level 5, 50 Nanyang Drive, 637553 Singapore, Singapore

[⊥]Department of Materials Science and Engineering, Research Institute of Advanced Materials, Seoul National University, 1 Gwanak-ro, Gwanak-gu, Seoul 08826, Republic of Korea

Downloaded via SEOUL NATL UNIV on December 22, 2020 at 06:48:54 (UTC).
See https://pubs.acs.org/sharingguidelines for options on how to legitimately share published articles.

ABSTRACT: Next-generation displays and lighting technologies require efficient optical sources that combine brightness, color purity, stability, substrate flexibility. Metal halide perovskites have potential use in a wide range of applications, for they possess excellent charge transport, bandgap tunability and, in the most promising recent optical source materials, intense and efficient luminescence. This review links metal halide perovskites' performance as efficient light emitters with their underlying materials electronic and photophysical attributes.

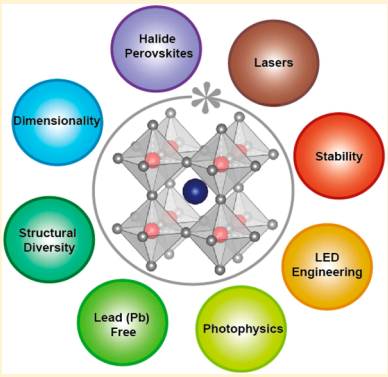

CONTENTS

1. Introduction: Overview of Perovskites and Their Optoelectronic Properties 7445
2. Chemical and Structural Diversity in Perovskites 7445
2.1. Effect of Organic and Inorganic Compounds 7446
2.2. Effect of Dimensionality in Perovskites 7447
2.2.1. Three-Dimensional Perovskites 7447
2.2.2. Two-Dimensional Perovskites 7448
2.2.3. Zero-Dimensional Perovskites 7448
2.3. Lead-Free Perovskites 7449
3. Perovskite Photophysical Properties 7451
3.1. Recombination Mechanisms 7451
3.2. Exciton and Free Carrier Dynamics 7453
3.3. Photoluminescence Quantum Yield 7453
4. Perovskite Light Emitting Diodes (LEDs) 7454
4.1. Perovskite Material Engineering for LEDs 7454
4.1.1. Modulating Dimensionality in Perovskite for LEDs 7454
4.1.2. Colloidally-Synthesized Perovskite NCs for LEDs 7456
4.2. Engineering Perovskite LEDs toward High Efficiency 7459
4.2.1. Engineering Interfacial Layers 7459
4.2.2. Comparison of Perovskite LED with QLED and OLEDs 7461
4.3. Stability of Perovskite LEDs 7462
4.3.1. Status and Mechanisms Underpinning Stability in Perovskite LEDs 7462
4.3.2. Strategies to Improve LED Stability 7465
5. Perovskites for Lasing 7465
5.1. Optical Amplification Using Perovskites 7465
5.1.1. Original Reports of Perovskite Lasing 7466
5.1.2. Effects of Perovskite Crystal Structures 7466
5.2. Laser Cavity Structures in Perovskite Lasers 7467
6. Conclusions and Outlook 7468
Associated Content 7469
Special Issue Paper 7469
Author Information 7469
Corresponding Author 7469
ORCID 7469
Notes 7469
Biographies 7469
Acknowledgments 7469
References 7469

Received: February 15, 2019
Published: April 25, 2019

 © 2019 American Chemical Society

DOI: 10.1021/acs.chemrev.9b00107
Chem. Rev. 2019, 119, 7444−7477

1. INTRODUCTION: OVERVIEW OF PEROVSKITES AND THEIR OPTOELECTRONIC PROPERTIES

Hybrid perovskites are an emerging class of semiconducting materials exhibiting outstanding optoelectronic properties. The general chemical formula for perovskite is ABX_3, in which A and B are cations and X are anions that octahedrally coordinate to B. The large A-site cations and the smaller B-site cations, allowing $[BX_6]^{4-}$ octahedra to corner-share in a 3D framework, with the A-site cations located in the framework cavities. The canonical perovskite material is calcium titanate, discovered in by Gustav Rose in 1839 and named in honor of Lev Perovski (1792−1856).

Diverse perovskite materials exhibit ferroelectricity, superconductivity, and magnetoresistance, to name a few of their intriguing properties. Metal halide perovskites exhibit high absorption coefficients (in $CH_3NH_3PbI_3$ of order 10^4 cm^{-1}), high charge-carrier mobilities (exceeding 10 cm^2 V^{-1} s^{-1}), long minority carrier diffusion lengths (1 μm and greater), and low trap densities (lower than 10^{16} cm^{-3}). These impressive properties make halide perovskites excellent semiconductors for solar cells. Since Miyasaka and co-workers introduced halide perovskites in liquid-electrolyte solar cells in 2009, thousands of researchers have turned their attention to perovskite solar cells (PSCs) (Figure 1).[1−6] The certified power conversion efficiency of PSCs has risen in nine years from approximately 3% to greater than 23%[7] (Figure 2).

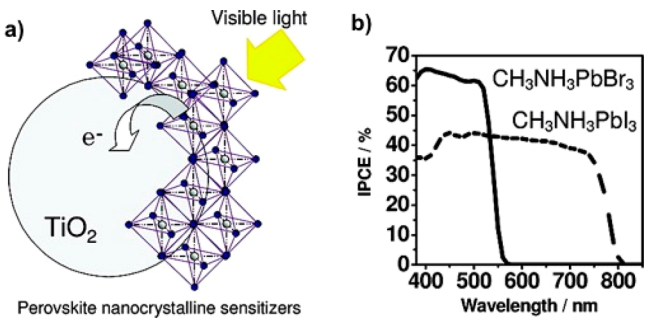

Figure 1. Perovskites (a) sensitizers of TiO_2 in solid-state dye-sensitized solar cells. (b) Incident photon to current quantum conversion efficiency spectra of $CH_3NH_3PbBr_3$ and $CH_3NH_3PbI_3$.[1] Reproduced with permission from ref 1. Copyright 2009 American Chemical Society.

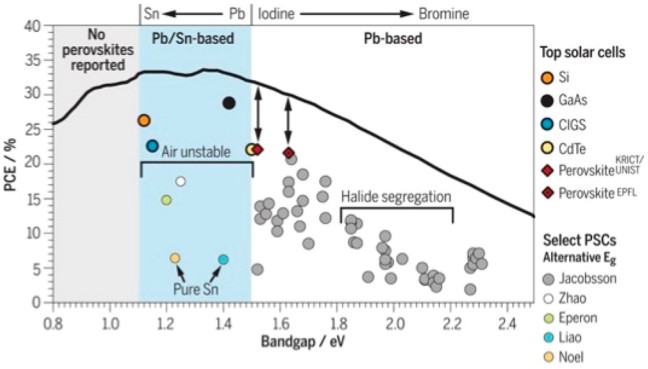

Figure 2. State-of-art perovskite solar cell efficiencies as a function of bandgap energy.[8] Reprinted with permission from ref 8. Copyright 2017 AAAS.

Halide perovskites also possess materials properties of interest for optical sources: bright photoluminescence, narrow light emission line width, tunable exciton binding energy, and balanced charge carrier mobility.[9,10] In the early 1990s, researchers applied layered structured halide perovskites (e.g., Ruddlesden−Popper phases) to create light-emitting diodes (LEDs) that operated at liquid nitrogen temperature.[11] In 2012, room temperature halide perovskite LEDs were reported.[12] In 2015, the first efficient perovskite LEDs (EQE ∼ 8.5%) were reported.[13] Studies of perovskite optical sources have similarly intensified in the past six years.

This Review discusses the structural and materials processing degrees of freedom available in perovskites and their impact on light emission and photophysical properties. We discuss cases for, and the challenges in, the use of perovskites in optical sources. We address device architectures in perovskite LEDs as well as interface engineering therein. We seek to connect device performance with underlying photophysics and perovskites' distinctive optical properties.

2. CHEMICAL AND STRUCTURAL DIVERSITY IN PEROVSKITES

Three lattice positions in perovskites are referred to as the A, B, and X sites. The highest symmetry phase perovskite occupies the *Pm3m* space group in which the ions are perfectly packed and their ionic radii follow $r_A + r_X = \sqrt{2}(r_X + r_X)$ where r_A, r_B, and r_X are the ionic radii of A, B, and X. To study the stability of perovskites, Goldschmidt proposed the tolerance factor t and the octahedral factor μ. The tolerance factor indicates the state of distortion by $t = (r_A + r_X)/\sqrt{2}(r_X + r_X)$ and the octahedral factor is determined by the ratio of $\frac{r_B}{r_X}$ for the BX_6 octahedron. In general, hybrid perovskites present $0.44 < \mu < 0.90$ and $0.81 < t < 1.11$. For the perovskite cubic structure, t falls between 0.9 and 1.0, whereas the 0.71−0.90 range exhibits tetragonal and orthorhombic structures (Figure 3). Many properties of perovskites are affected by structural distortions and, as a consequence, partial or full cation and/or anion substitution can be used to tune the physical properties. In metal halide perovskites, the B-site metal is typically a divalent cation (e.g., Pb^{2+}, Sn^{2+}, Ge^{2+}, Mg^{2+}, Ca^{2+}, Sr^{2+}, Cu^{2+}, Ni^{2+}), the A-site is a monovalent cation (e.g., Cs^+, $CH_3NH_3^+$ (MA), $HC(NH_2)_2^+$

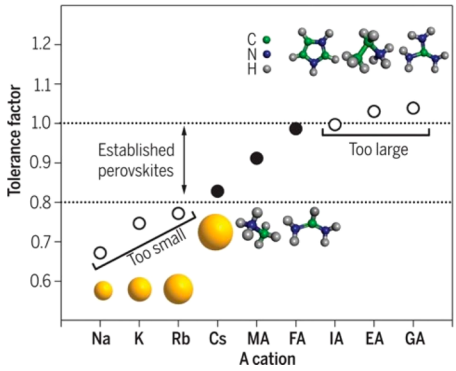

Figure 3. Tolerance factor in $APbI_3$ perovskites prohibits the use of Na, K, and Rb as A cations; whereas Cs, MA, and FA are widely used, and imidazolium (IA), ethylamine (EA), and guanidinium (GA)] are too large to fit into the 3D cage.[14] Reprinted with permission from ref 14. Copyright 2016 AAAS.

DOI: 10.1021/acs.chemrev.9b00107
Chem. Rev. 2019, 119, 7444−7477

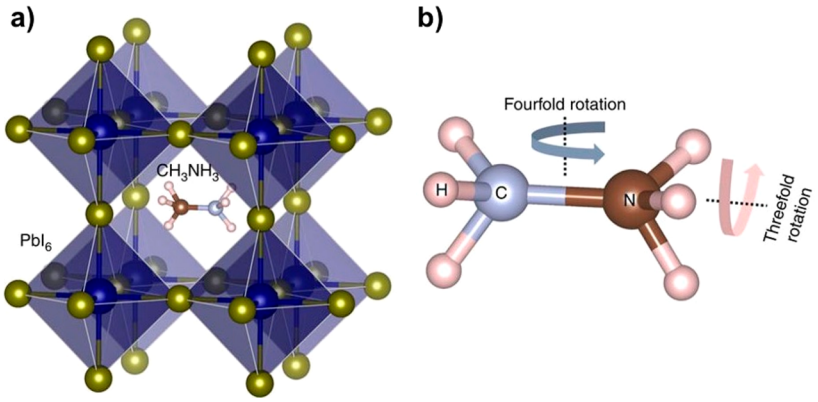

Figure 4. (a) Schematic of the perovskite crystal structure. The figure depicts orientational disorder of organic cations in the center of PbI_6 octahedral cage. (b) Geometry of methylammonium illustrating 3-fold and 4-fold jumping rotational modes.[24] Reprinted with permission from ref 24. Copyright 2017 Nature Publishing Group.

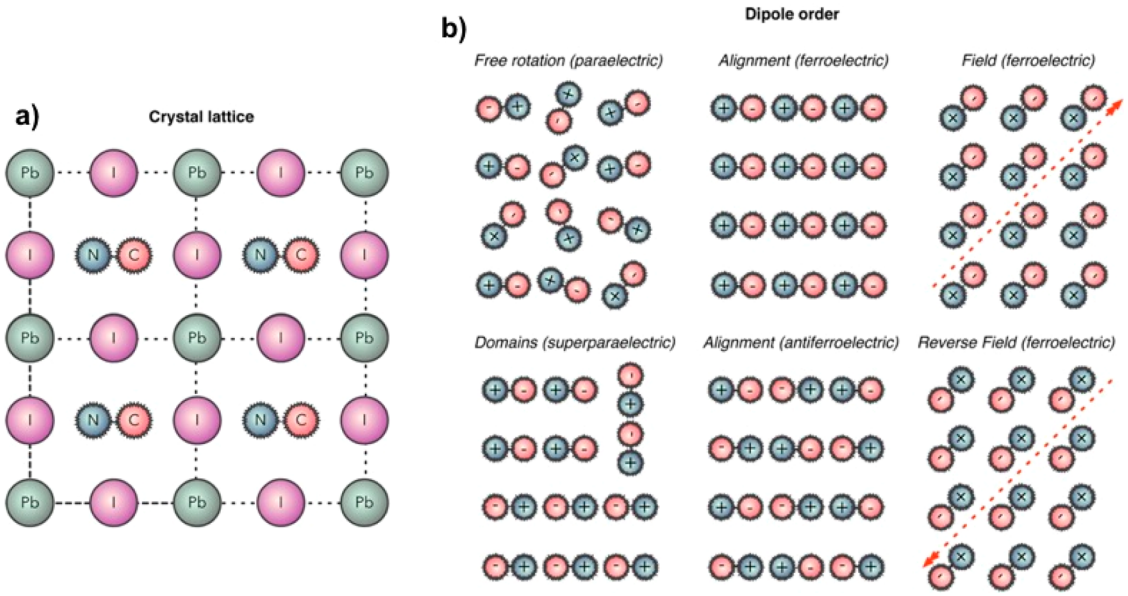

Figure 5. Schematic illustration of crystal structure in $MAPbI_3$. (a) Molecular dipole orientation in perovskite lattice. (b) The molecular dipole of MA is 2.3 D, distinguishing it from spherical/symmetric cations in inorganic perovskites such as $CsSnI_3$.[16] Reproduced with permission from ref 16. Copyright 2014 American Chemical Society.

(FA) and the X-site is a halide or pseudohalide anion (e.g., I^-, Br^-, Cl^-, etc).

Accessing the lower-dimensional structural family, such as one-dimensional (1D) chained architectures and zero-dimensional (0D) isolated octahedra, adds further tuning through chemical and structural engineering. Modification of composition and structure in low-dimensional perovskites enables tuning of electronic bandgaps, exciton binding energies, and electronic transport properties.

2.1. Effect of Organic and Inorganic Compounds

To describe the symmetry of halide perovskites, one needs to consider the dynamic motion of organic A-sites and X-sites. Disordered A-site organic cations change hydrogen bonding and thus affect symmetry variations. The specific alignment of the A-site polar organic cation is induced by hydrogen bonding in the perovskite lattice, a fact that may result in bulk electric ordering.[15] This electronic ordering is dependent on the dipole moments of the A-site and the strength of the hydrogen bonds (Figure 4). Organic cations (MA ions) possess an electrical dipole of 2.3D,[16] an aspect that impacts the observed properties and behavior of perovskite solar cells (Figure 5). For example, the dipolar disorder of MA cations contributes to high dielectric constants in $MAPbX_3$, a fact that assists in screening charged states.[17] The incorporation of MA does not necessarily reduce the formation of defects, but the incorporation of the dipolar MA cation in mixed cation mixed halide wide-bandgap perovskites heals deep trap defects, resulting in a more defect-tolerant material.[18] Quasielastic neutron scattering (QENS) measurements have directly measured the motions of MA ions within the inorganic lattice of the perovskite. Density functional theory (DFT) on lattice dynamics indicates that low-energy phonons are composed entirely of the motion of metals and halides[19−23] and that these are readily excited at lower temperatures and determine the ensuing physical properties.

In an ideal cubic halide perovskite, the B-site divalent metal is located at the body-centered position of the cube, and the anions occupy the six face-centered locations, forming an octahedral surrounding for the divalent metal, with the monovalent cations situated at the cube vertices. The chemical

DOI: 10.1021/acs.chemrev.9b00107
Chem. Rev. 2019, 119, 7444−7477

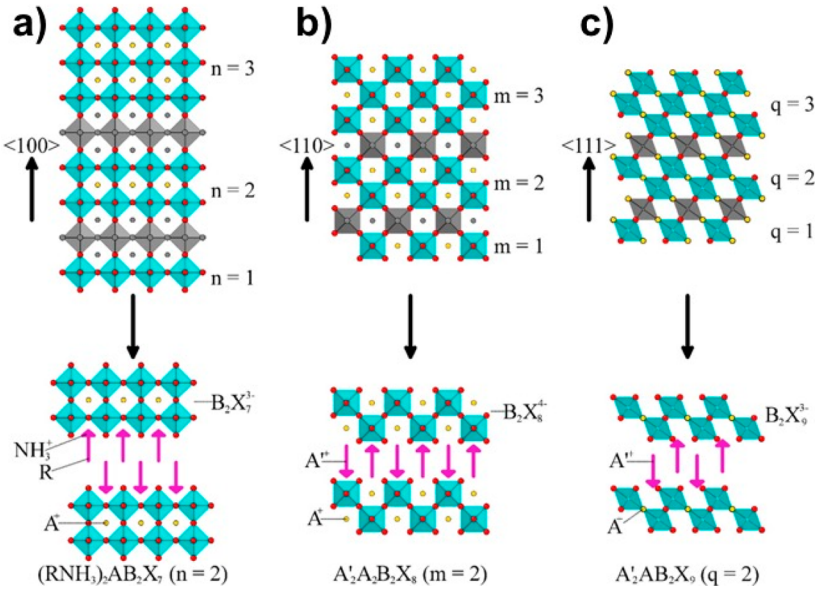

Figure 6. Crystal structures of low dimensional perovskites having different orientations. (a) The ⟨100⟩-oriented layered perovskites $(RNH_3)_2A_{n-1}B_nX_{3n+1}$. (b) The ⟨110⟩ oriented layered perovskites $A'_2A_mB_mX_{3m+2}$. (c) The ⟨111⟩-oriented perovskites $A'_2A_{q-1}B_qX_{3q+3}$. Reproduced with permission from ref 27. Copyright 2016 American Chemical Society.

bonding between the metal and the halogen determines the bandgap and the dispersion of the energy bands in the material. Larger electronegativity differences correspond to a more ionic bond character, resulting in an electronic cloud less dispersed along the bond and located closer to the nuclei.

The inorganic metal cation at the B site is often chosen to be Pb^{2+} in light of the superior optoelectronic properties and solar cell performance of the resultant material. There is interest in finding ions to replace Pb in light of its environmental/toxicological properties.[25] Engineering the choice of the B site cation also affects the dimensionality of the perovskite structure, particularly so in the case of trivalent and tetravalent metal cations.

The bandgap energy of perovskites is varied by the alternation of the anion (typically I^- and/or Br^-) and the use of mixed anions. For example, the absorption spectrum of the $MAPbI_{3-x}Br_x$ perovskites blue-shifts as the bromide concentration is increased, a fact related to the lower electronegativity of the smaller halogen atoms. The optical absorption is therefore readily tuned, via bandgap engineering in halide perovskites, across the visible spectrum.

2.2. Effect of Dimensionality in Perovskites

Reducing perovskite materials' dimensionality also modulates their optical properties.[26] The structural freedom in reduced dimensional perovskites creates the possibility to create tunable photophysical and electronic properties. The ABX_3 structure has rigid structural constraints due to the corner-shared BX_6 octahedral crystal structure, whereas the reduced dimensional perovskites allow for increased structural flexibility, influenced by the length of interlayer organic cations. As the ABX_3 perovskite structure is cut into layers, the size limitation and the tolerance factor seen in the bulk perovskites can be widely engineered. In two-dimensional (2D) derivatives of the perovskites, the interlayer A cation lengths are more easily tuned, and in the zero-dimensional (0D) derivatives, size restrictions are not applicable, as the isolated MX_6 octahedra shift readily in relative position (Figure 6).

2.2.1. Three-Dimensional Perovskites.

Early embodiments of perovskite solar cells were demonstrated using three-dimensional (3D) $MAPbI_3$ compounds in 2009. The 3D perovskites exhibits a sharp optical absorption onset, with an absorption coefficient (α) exceeding 10^4 cm^{-1} near the band edge.[27] The bandgap of $MAPbI_3$ is evaluated to be 1.50−1.55 eV using UV photoelectron spectroscopy. The $MAPbI_3$ single crystals shows exceptionally low trap-state densities on the order of 10^9 cm^{-3} to 10^{10} cm^{-3}, deep values comparable to those in crystalline silicon, and charge carrier diffusion lengths on the order of 3−10 μm have been reported.[9,28] Charge mobilities in thin film $MAPbI_3$ were obtained as high as 0.5 $cm^2/(V\ s)$ using field-effect transistor measurements (FETs).[29] However, the volatile nature of MA cations in perovskites may cause instability against moisture and heat; evaporation may be possible at temperatures as low as 85 °C, and indeed such materials have been seen to degrade after exposure to moisture, heat, and light soaking.

Replacing MA with other organic or inorganic cations tunes the bandgap of 3D lead halide perovskites. A new choice of A site cation changes the bandgap because of the modification of the lattice constant: FA is larger than MA, which in turn is larger than Cs, resulting in an increase of bandgap going from FA to Cs through MA. The A-site cation also influences the extent of metal-halide orbital overlap. This change in metal-halide bonding has a direct impact on valence and conduction band positions.[30]

When one uses formamidinium ($HC(NH_2)_2$) as the A cite cation, the perovskite bandgap reduces by about 0.07 eV compared with MA perovskite, a fact that has been exploited in achieving the most recent photovoltaic performance advances. Because FA produces more thermally stable materials, FA-based perovskites are also promising materials for high efficiency photovoltaics. However, the phase instability of $FAPbI_3$ perovskites makes it difficult to maintain the desired photoactive black phase at room temperature. This has led to a considerable recent focus on 3D perovskites in which the A cation is replaced with Cs^+, and mixed triple cations (Cs/FA/

DOI: 10.1021/acs.chemrev.9b00107
Chem. Rev. 2019, 119, 7444−7477

MA) are employed to improve phase/thermal stability and performance in devices.[31]

Mixed halide perovskites are of interest also in view of their continuous bandgap tunability (approximately 1.7−1.9 eV). Unfortunately, bandgap instability due to photoinduced ion segregation occurs even when mixed halides are used in mixed-cation perovskites.[32] Recently, Stranks and co-workers demonstrated passivation of surface and grain boundaries in perovskite films to mitigate both nonradiative losses and photoinduced ion migration.[33] Bandgap instability was substantially suppressed using interface approaches: Rand and co-workers reported a strategy to suppress halide ion migration using long organic alkyl ammonium capping layers to reduce perovskite grains at the nanometer size scale.[34]

Substituting Pb with Sn in the halide perovskites has been demonstrated to narrow the bandgap to 1.2−1.4 eV. Mixed Sn/Pb perovskites with the composition $CsPb_{1-x}Sn_xIBr_2$ have been fabricated via one-step antisolvent spin-coating methods.[35] Sn substitution alters the driving force for phase segregation and increases the barrier for ionic diffusion, a factor that may contribute to enhanced phase stability.

The remarkable performance of perovskite solar cells and LEDs is correlated with their long excited state lifetimes and high photoluminescence (PL) efficiencies. High-quality perovskite films exhibit longer PL lifetimes, and it has been demonstrated that grain boundaries play an important role in determining physical properties. Ginger and co-workers used confocal fluorescence microscopy correlated with scanning electron microscopy to resolve spatially the PL decay dynamics of $MAPbI_3(Cl)$ perovskite films. They observed that PL intensity and lifetime differ among the grains in the perovskite films. The grain boundaries in the perovskite film were dimmer and exhibited faster nonradiative decay. Chemical treatment with pyridine activated the dark grain boundaries and provided passivation that led to brighter materials.[36]

2.2.2. Two-Dimensional Perovskites. Long-chain alkyl ammonium organic/inorganic lead halide perovskites were fabricated, early in perovskite studies, producing materials with the formula of A'_2MX_4 and often known as two-dimensional (2D) perovskites. Here A′ is the long organic alkylammonium cation, M a divalent metal cation, and X a halide anion. Most reported 2D perovskite derivatives feature mono- and diammonium cations, with general formula of $(NH_3RNH_3)MX_4$ or $(RNH_3)_2MX_4$, R represents an organic functional group. The crystal structure is expressed with reference to the orientation and configuration of the organic.[37]

Low-dimensional perovskites are formed by slicing the 3D compounds in different crystallographic directions, and the organic cation and reaction stoichiometry play an important role in determining the crystal orientation. Tuning of the dimensionality affects physical properties: the bandgap of the compounds increases as the dimensionality of the structure is reduced, as in thin quantum wells other semiconductors. Early research on low-dimensional perovskites included pioneering reports on the compound $(C_4H_9NH_3)_2(CH_3NH_3)_{n-1}Sn_nI_{3n+1}$.[38] The 3D perovskite $CH_3NH_3SnI_3$ is a small-bandgap semiconductor, whereas the $n = 1$ compound $(C_4H_9NH_3)_2SnI_4$ is a larger bandgap semiconductor.[38] Unfortunately, $(C_4H_9NH_3)_2SnI_4$ is sensitive to air, and degradation occurs within several hours. Material synthesis to device testing must be carried out in an inert atmosphere.

These low-dimensional materials are natural quantum-well structures, and they possess large exciton binding energies (>100 meV) due to strong electron−hole interactions originating from the distinct dielectric environment in the well vs the barrier. This enhances photoluminescence intensity, and the high quantum yield also benefits from diminished forbidden electronic transitions. The strong confinement in a wide range of structurally flexible, low-dimensional perovskites are well-suited to light-emitting applications.

Electroluminescence (EL) was observed from $(C_6H_5C_2H_4NH_3)_2(CH_3NH_3)Pb_2I_7$ in early 1990; however, this was observed only at 200 K and with the application of a 10 kV/cm electric field.[39] Thermal quenching of the exciton was the main reason for the reduction of EL near room temperature.[40]

More recently, low-dimensional perovskites have attracted renewed interest for solid-state lighting applications. Higher-number layered compounds $(A'_2A_{n-1}Pb_nX_{3n+1})$ with $n = 2, 3, 4$, etc. are formed through mixture of cations of different sizes, capable of forming mixed 3D and layered perovskite structures.[41−43] By making films consisting of a range of n, one can produce energy funneling through a collection of grains having different bandgaps. This has been found to enhance luminescence properties at room temperature.[41−45]

Low-dimensional perovskites with the formula $(A')_2(CH_3NH_3)_{n-1}Pb_nX_{3n+1}$ have also been demonstrated to stabilize solar cell performance against moisture, a finding explained by the increased formation energy compared with their 3D bulk perovskite counterparts.[26,46,47] The low-dimensional perovskites typically feature different cuts from the 3-D structure along the ⟨100⟩, ⟨110⟩, and ⟨111⟩ directions. ⟨100⟩-Oriented perovskites are obtained by removing the metal (Pb) component from the inorganic framework. In contrast to the ⟨100⟩-oriented perovskite hybrid that represents today the most richly explored member of the reduced-dimensional perovskite family, the ⟨110⟩- and ⟨111⟩-oriented perovskites have rarely been reported. ⟨110⟩-Oriented organic−inorganic perovskites have the formula $[NH_2-C(I)]NH_2]_2(CH_3NH_3)_nSn_nI_{3n+1}$ ($n = 1-4$) and were reported by Mitzi and co-workers.[48] These perovskites were stabilized via the incorporation of methylammonium and iodoformamidinium cations. Differently dimensioned inorganic sheets are obtained by modulating the proportions of the two ligands. When $n > 2$, the methylammonium cations occupy the channel position defined by the corner-sharing metal halide octahedra. The iodoformamidinium cations play an important role in directing the self-assembly of ⟨110⟩-oriented perovskites.

The ⟨111⟩-oriented perovskites are obtained with the formula of $A'_2A_{n-1}B_nX_{3n+3}$, where A′ and A are interlayer and intralayer organic cations. An example $n = 1$ member is $(H_23\text{-AMP})_2PbBr_6$ (AMP = (aminomethyl)pyridinium). These have a higher presence of the more distorted $PbBr_6$ octahedra, increasing the bandgap. Reported $n = 2$ members, including $(NH_4)_3Sb_2I_9$, $(CH_3NH_3)_3Bi_2Br_9$, $[NH_2(CH_3)_2]_3Sb_2Cl_9$, $[NH(CH_3)_3]_3Sb_2Cl_9$, and $(CH_3NH_3)_3Sb_2I_9$, also feature small inorganic cations with $Cs_3Sb_2I_9$.[49−52]

2.2.3. Zero-Dimensional Perovskites. Structurally distorted perovskites can be considered zero-dimensional (0D) analogues. Karunadasa and co-workers reported (NMEDA)-$PbBr_4$ and $(EDBE)PbX_4$ (N-MEDA = *N*1-methylethane-1,2-diammonium, EDBE = 2,2-(ethylenedioxy)bis-(ethylammonium)), materials that exhibited white light

DOI: 10.1021/acs.chemrev.9b00107
Chem. Rev. 2019, 119, 7444−7477

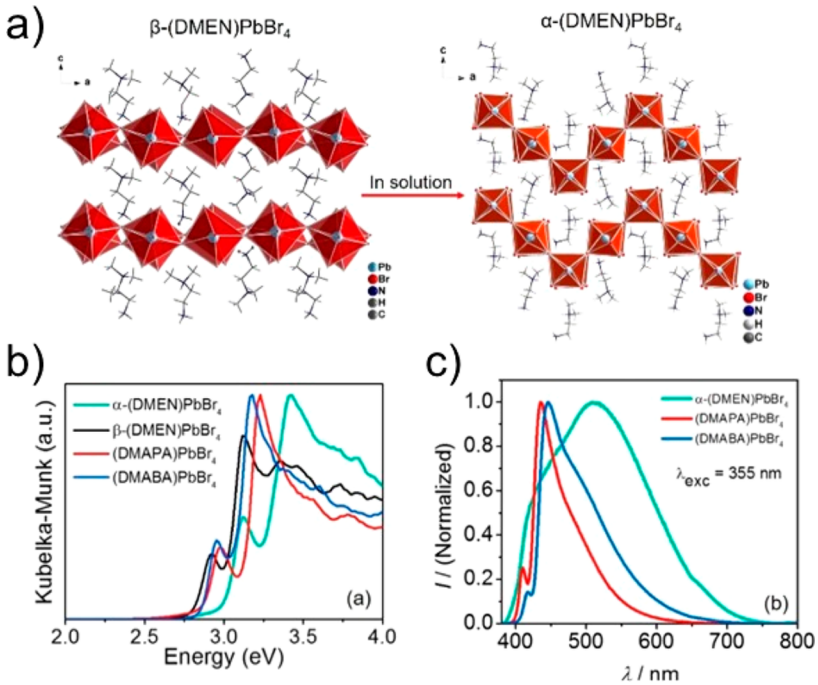

Figure 7. Structural distortion induced 0D perovskites with white light emission.[57] (a) Transformation of β-(DMEN)$PbBr_4$ to α-(DMEN)$PbBr_4$ in the liquor solution. (b) Optical absorption spectra of α-(DMEN)$PbBr_4$, β-(DMEN)$PbBr_4$, (DMAPA)$PbBr_4$, and (DMAPA)$PbBr_4$. (c) Steady-state PL emission spectra of α-(DMEN)$PbBr_4$, (DMAPA)$PbBr_4$, and (DMABA)$PbBr_4$ excited at 355 nm. Reproduced with permission from ref 57. Copyright 2017 American Chemical Society.

emission.[53,54] The wide PL line width was impacted by the structural distortion, indicated by the distortion of the $PbBr_6$ octahedron.[55] White light emission was attributed to self-trapped excitons localized in the inorganic lattice. Mao et al. reported white light-emitting perovskites with composition (DMEN)$PbBr_4$ (DMEN = 2-(dimethylamino)ethylamine), (DMAPA)$PbBr_4$ (DMAPA = 3-(dimethylamino)-1-propylamine), and (DMABA)$PbBr_4$ (DMABA = 4-dimethylamino-butylamine)[56] (Figure 7). Among these compounds, (DMEN)$PbBr_4$ has the largest distortion (Δd_{avg} = 17.4 × 10^{-4}) and showed broad emission.

The perovskite-related Cs_4PbBr_6 structure, first synthesized in 1999 by Nikl et al.,[58] presents a zero-dimensional (0D) crystalline structure in which adjacent $[PbBr_6]^{4-}$ octahedra do not share corners (Figure 8). Manna and co-workers pioneered a facile fabrication strategy to produce Cs_4PbBr_6, starting from $CsPbBr_3$ nanocrystals (NCs): they added different amines to obtain 0D Cs_4PbBr_6 NCs at room temperature.[59] The stability of these NCs in solution was rather low; the particles aggregated in a few minutes. The optical properties measured after the transformation from $CsPbBr_3$ NCs reveal a sharp absorption at 317 nm, which indicates transformation to the Cs_4PbBr_6 phase. Cs_4PbBr_6 NCs have also been prepared in a Cs-rich environment via a hot-injection method.[60] Chemical transformation from nonluminescent Cs_4PbX_6 to emissive $CsPbX_3$ was triggered by chemical transformation, and this was accompanied by increased air stability and tunable optical properties. The extraction of CsX from Cs_4PbX_6 can be achieved either by thermal annealing (a physical approach) or by a chemical reaction with Prussian Blue (chemical approach).[61] Alivisatos and co-workers have synthesized another derivative of $CsPbBr_3$ NCs: they formed lead-halide-depleted perovskite derivative Cs_4PbBr_6 NCs. The transformation is governed by a two-step dissolution−recrystallization mechanism and mediated by the influence of the ligand shell environment on the crystal surface.[62]

Because Cs_4PbBr_6 shows a large bandgap, researchers recently explored the incorporation of perovskite NC emitters into another crystalline transport phase.[63] $CsPbBr_3$ NCs embedded in a robust and air-stable Cs_4PbBr_6 microcrystal phase resulted in high luminescence properties, specifically PLQY exceeding 90% in the solid state. The authors demonstrated the role of a lattice match between $CsPbBr_3$ and the Cs_4PbBr_6 matrix. Chen et al. reported a related study involving $CsPbBr_3$ embedded in a Cs_4PbBr_6 matrix and reported high efficiency and wide color gamut prototype white LEDs.[64]

2.3. Lead-Free Perovskites

The regulated nature of lead (Pb) may limit the application of otherwise-promising perovskites. Therefore, there is considerable interest in identifying promising lead-free alternatives. One such case is a class of materials known as double perovskites, in which two metals (e.g., metals with 1^+ and 3^+ oxidation states) are combined to yield the overall charge balance as seen in conventional single-metal-cation perovskites.[65−67] One example is the cubic $Fm\bar{3}m$ double perovskite synthesized in the form of $Cs_2AgBiBr_6$, having an estimated indirect bandgap of 1.95 eV (as obtained from UV−vis spectroscopy).[68]

Tin (Sn), closely analogous in many respects to Pb, has been investigated as a possible alternative to produce lead-free perovskites. Pb and Sn have a similar ionic radii (Pb 1.49 Å and Sn 1.35 Å) and analogous relativistic effects.[69] Sn can therefore substitute Pb with no significant perturbation in the lattice structure. However, Sn^{2+} can be easily oxidized to Sn^{4+} in air, and this can progress further to produce unacceptably high free carrier densities. Seok and co-workers reported a method to bind SnF_2 strongly with pyrazine: the SnF_2 accepts

DOI: 10.1021/acs.chemrev.9b00107
Chem. Rev. 2019, 119, 7444−7477

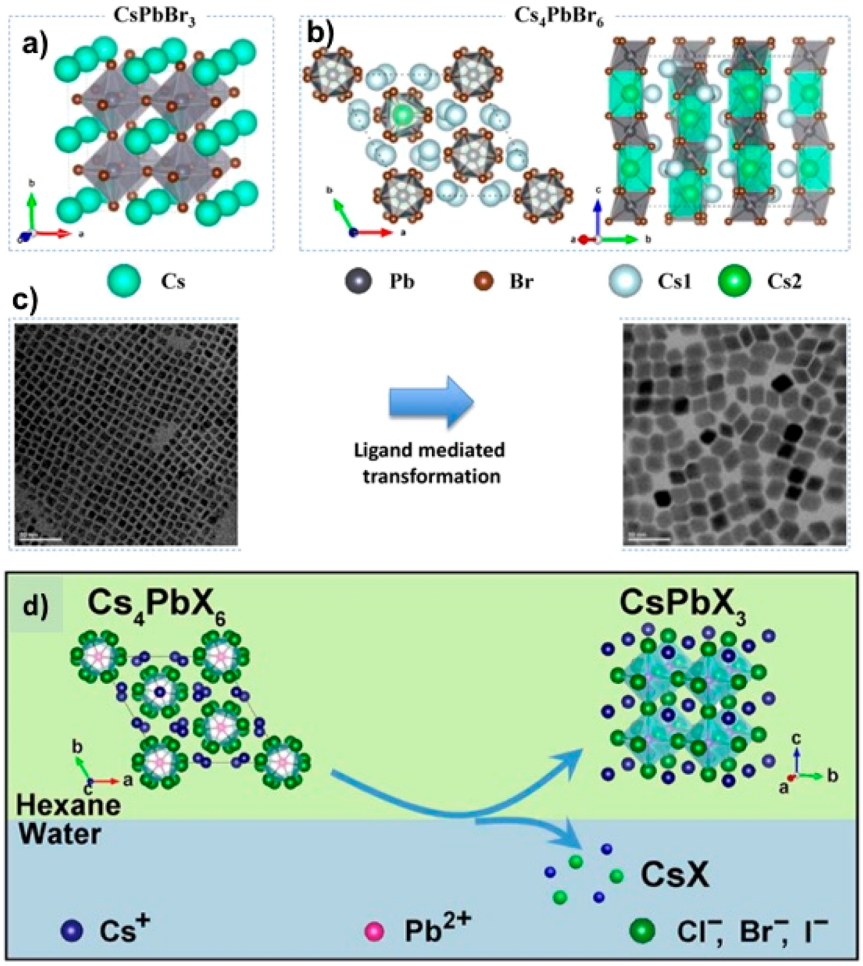

Figure 8. Schematic crystal structure of (a) $CsPbBr_3$ and 0D Cs_4PbBr_6 (b) along and perpendicular to *c* axis. (c) Typical TEM image of $CsPbBr_3$ and Cs_4PbBr_6 NCs, and images of NCs dispersed in hexane.[62] Reproduced with permission from ref 62. Copyright 2017 American Chemical Society. (d) Schematic illustration of change in the crystal structure going from Cs_4PbBr_6 to $CsPbBr_3$.[60] Reproduced with permission from ref 60. Copyright 2017, American Chemical Society.

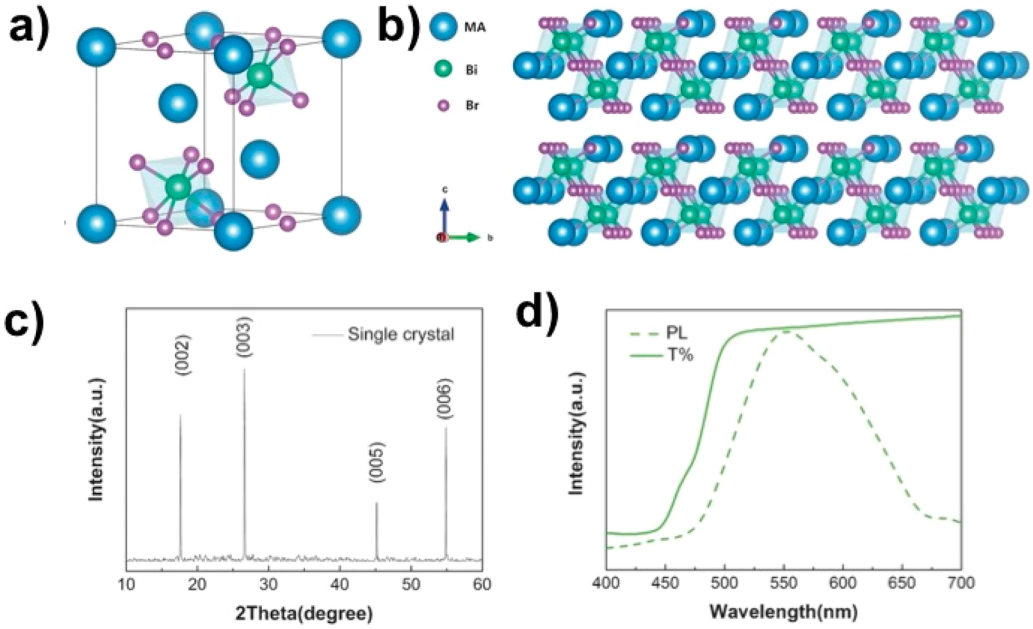

Figure 9. (a,b) Schematic structure of single-crystalline $MA_3Bi_2Br_9$. (c) Powder X-ray diffraction (XRD) spectra of single crystal $MA_3Bi_2Br_9$. (d) Transmission (solid) and PL (dashed) spectra of $MA_3Bi_2Br_9$ single crystal.[77] Reprinted with permission from ref 77. Copyright 2016 Wiley-VCH.

DOI: 10.1021/acs.chemrev.9b00107
Chem. Rev. 2019, 119, 7444−7477

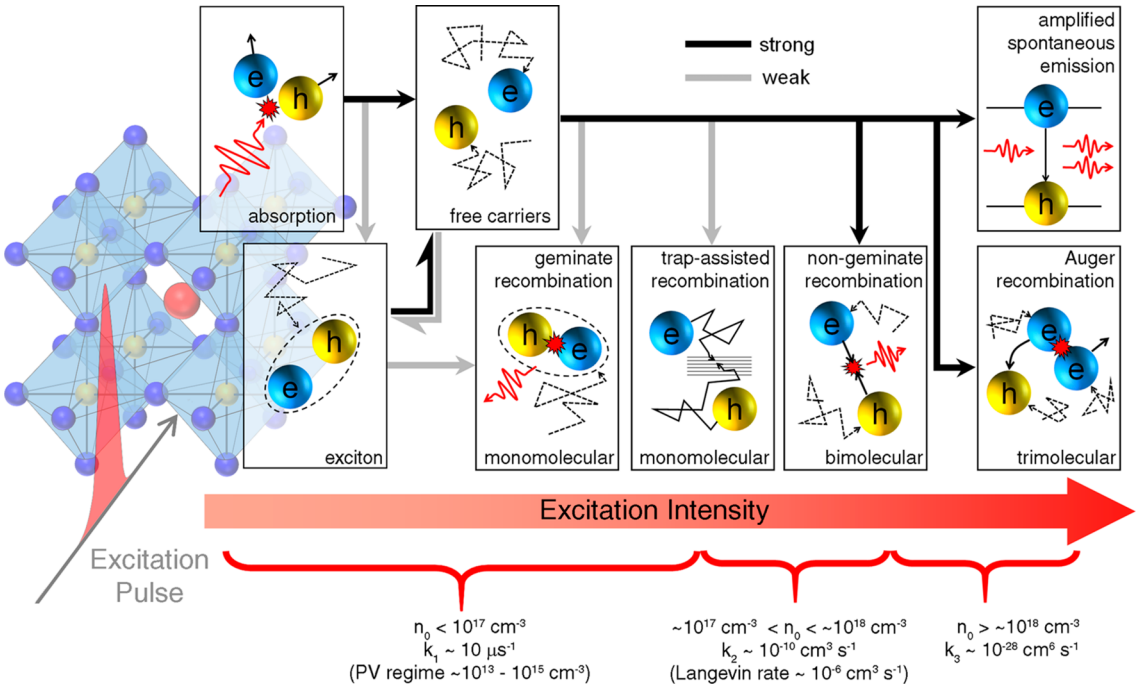

Figure 10. Rates of recombination, and photophysical processes, in $MAPbI_3$ over a range of carrier densities, n_0.[82] Reproduced with permission from ref 82. Copyright 2016 American Chemical Society.

lone pairs from the N atoms in pyrazine, and this combination of SnF_2−pyrazine reduces Sn vacancies.[70] The additive SnF_2 furthermore prevented Sn^{2+} from being oxidized to Sn^{4+}, reducing the charge carrier density in $FASnI_3$ perovskites.[71]

All-inorganic $CsSnX_3$ perovskites have been reported and applied to LEDs.[72] Thin SnX_2 and CsX films were sequentially deposited by vapor deposition then annealed to form uniform $CsSnX_3$ films via interdiffusion. Smooth, uniform films of $CsSnBr_3$ exhibiting full coverage and very small grain size (60 nm) were achieved; these exhibited an external quantum efficiency (EQE) of 0.34% in red-emitting diodes.

The 2D $(PEA)_2SnI_4$ exhibits superior PL properties compared to conventional 3D $CH_3NH_3SnI_3$, as reported by Haque and co-workers. These authors found that the 2D $(PEA)_2SnI_4$ perovskite displays improved stability compared to $CH_3NH_3SnI_3$ when aged in an air ambient in the dark.[73] Kanatzidis and co-workers used $CsGeI_3$ perovskites based on the trigonal pyramidal $[GeI_3]^-$ building block by tuning A-cations.[74] Moreover, Ge-based perovskites exhibit a large second harmonic generation (SHG) due to the sp-hybrid orbitals of germanium and iodide.

Ternary Sb^{3+} and Bi^{3+} have also attracted considerable interest in view of their structural flexibility and low toxicity. The $A_3Bi_2I_9$ perovskites involve a 1/3 bideficient layered perovskite with bioctahedral $(Bi_2I_9)^{3-}$ clusters surrounded by A^+ (Cs^+ or MA^+). However, trivalent bismuth and antimony perovskites result in 2D structure and show wider bandgaps than their 3D analogues. To maintain the 3D perovskite structure, an alternative approach was developed, one wherein Pb^{2+} was replaced to form a double perovskite structure of $A^I{}_2B^IB^{III}X_6$, by combining a monovalent cation and a trivalent cation having an ordered metal site arrangement.[75] However, from Tauc plot measurements, the perovskite showed an indirect bandgap, indicating that it may not be well-suited to efficient light emission. Solis-Ibarra and co-workers developed $Cs_4CuSb_2Cl_{12}$ perovskite, a mixed-metal ⟨111⟩-oriented layered structure incorporating Cu^{2+} and Sb^{3+} into layers (n = 3).[76] This material was a semiconductor with a direct bandgap 1.0 eV and a conductivity 1 order of magnitude greater than that of $MAPbI_3$.

Recently, $MA_3Bi_2X_9$ (X = Cl, Br, I) perovskite NCs were synthesized by Tang and co-workers[77] (Figure 9). These authors used a strategy based on reprecipitation assisted by ligands that enabled them to tune the PL emission peak wavelength from 360 to 540 nm via halide compositional control. The $MA_3Bi_2Br_9$ NCs had diameter ca. 3 nm and, for emission at 430 nm, the PLQY was an encouraging with 12%.

3. PEROVSKITE PHOTOPHYSICAL PROPERTIES

Of critical importance in the operation of electronic devices are processes such as the generation of charge carriers, excitons and also the diffusion and recombination of these photoexcited states. The rates of recombination of electrons and holes are lower than in prior singe-crystalline inorganic semiconductors.[78] Films based on polycrystalline perovskite constituents have shown impressive diffusion lengths (L_D > 1 μm) for minority carriers and correspondingly extended excited-state lifetimes ($\tau \geq 1$ μs). They have combined these features with excellent mobilities ($\mu \approx 1-100$ cm^2 V^{-1} s^{-1}),[78−81] even in the presence of realistic defect states (traps).

Here we review the nature of photogenerated exciton/carriers within perovskites (Figure 10).

3.1. Recombination Mechanisms

Using transient absorption (TA) and time-resolved photoluminescence (TRPL) measurements, one may determine the bimolecular recombination rate.[83−87] In $MAPbI_3$ perovskites, the results of early spectroscopic investigations were accounted for by invoking the charge separated states or excited charge transfer states.[87] It is now widely held that excitons dissociate spontaneously into separated electrons and holes, a fact that

DOI: 10.1021/acs.chemrev.9b00107
Chem. Rev. 2019, 119, 7444−7477

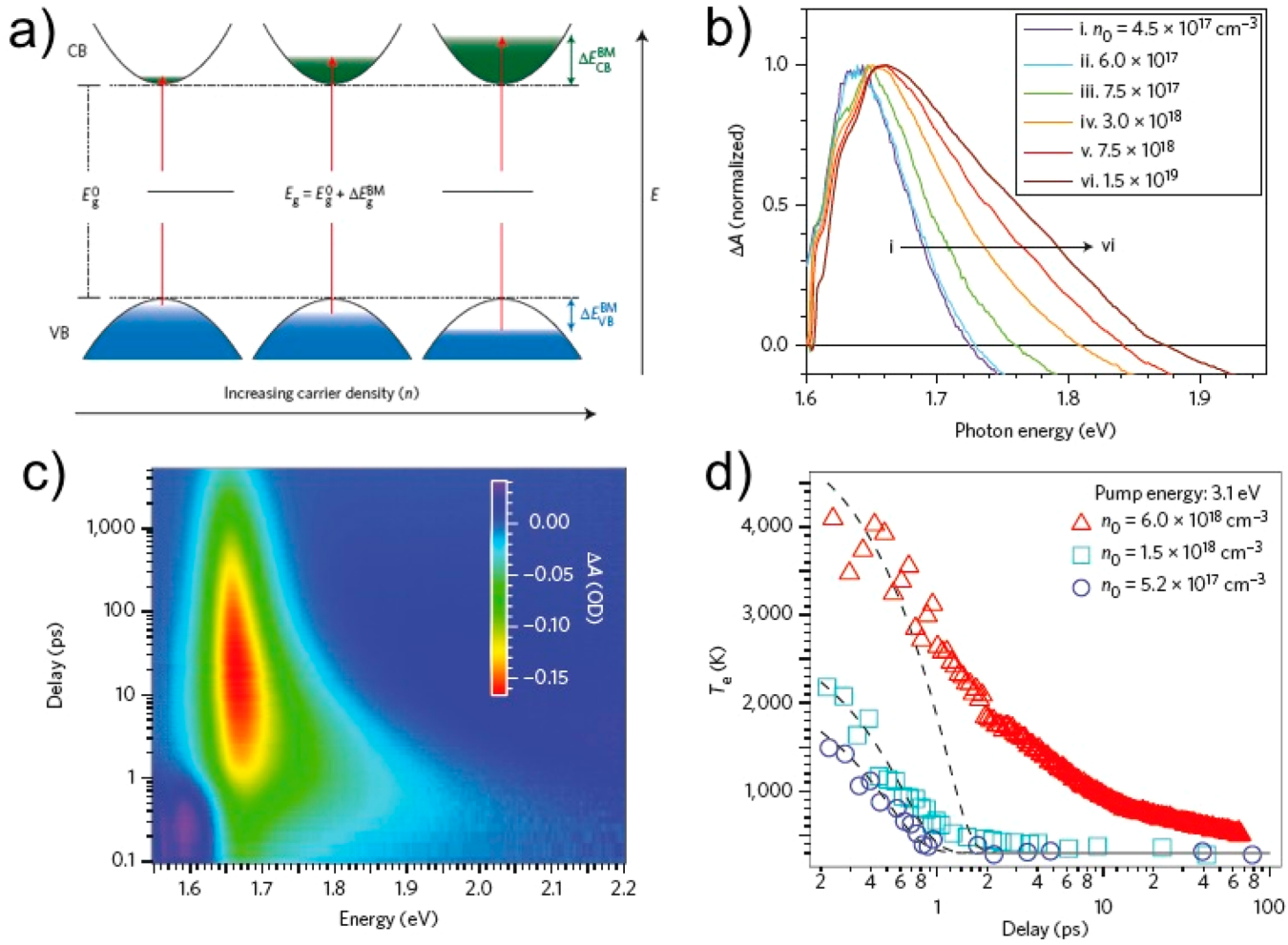

Figure 11. (a) Schematic illustration of the Burstein–Moss effect in $MAPbI_3$ perovskites.[83] Reprinted with permission from ref 83. Copyright 2014 Nature Publishing Group. (b) Normalized spectra (TA) of the band edge transition in $MAPbI_3$.[83] (c) Pseudocolor representation TA spectra shows hot carrier thermalization in $MAPbI_3$ Reprinted with permission from ref 91. Copyright 2015 Nature Publishing Group. (d) Time-dependent T_e with the same n_0 but varying $\hbar\omega_{pump}$, dashed lines are calculated cooling curves.[91] Reprinted with permission from ref 91. Copyright 2015, Nature Publishing Group.

contributes to the impressive performance of perovskite devices.

The photophysics of perovskites depends on excitation level. When the conditions of photoexcitation produce low carrier densities in the range $n_0 \approx 10^{13}$–10^{15} cm^{-3}, these are of the level relevant to solar cells, monomolecular trap-assisted recombination or geminate recombination are each low in efficiency. They have a low first-order recombination coefficient in the vicinity of $k_1 \approx 10\ \mu s^{-1}$.[88]

In contrast, when the photocarrier densities are higher at $n_0 \approx 10^{16}$–10^{18} cm^{-3}, effects associated with multiparticle processes, such as nongeminate recombination (bimolecular) and Auger recombination processes (trimolecular), gain in importance and indeed begin to dominate the excited state lifetime.[89,90]

We write the rate equation for charge-carrier recombination in a way that takes account of both monomolecular and also higher-order processes (eq 4):

$$\frac{dn}{dt} = G - k_1 n - k_2 n^2 - k_3 n^3 = G - nR_T(n) \quad (4)$$

In this equation, G is the charge-density generation rate. The term k_1 provides the coefficient associated with monomolecular recombination. The coefficient k_2 functions as the constant of proportionality informing the bimolecular electron–hole recombination rate. Finally, k_3 quantifies the Auger rate.

Kamat and co-workers found that strong band-filling effects and bandgap renormalization observed from $MAPbI_3$ at high pump fluences.[83] Ultrafast relaxation processes in thin films of the hybrid perovskite $MAPbI_3$ indicated a carrier-density-dependent blue-shift and broadening of the 760 nm photogenerated ground-state bleach, indicating charge carrier accumulation and explained on the basis of a Burstein–Moss shift (a dynamic one in this instance). The band edge states lead to higher-energy optical transitions, a fact connected to the Pauli exclusion principle (Figure 11).

Yang et al., have quantitatively correlated the TA spectra with photophysical properties including carrier density, the carrier temperature, bandgap renormalization, and exciton binding energy, which demonstrated the interplay between free-carrier induced bleaching of the excitonic and continuum transitions near the band edge.[91] The carrier temperature can be extracted from the TA spectra and help to illuminate carrier cooling dynamics. Measurements have indicated slow hot-carrier cooling with high excitation density, attributed to a hot-

DOI: 10.1021/acs.chemrev.9b00107
Chem. Rev. 2019, 119, 7444–7477

phonon bottleneck. The observed phonon bottleneck slows hot carrier cooling above a critical injection carrier density of $\sim 5 \times 10^{17}$ cm^{-3}.

3.2. Exciton and Free Carrier Dynamics

Because hybrid halide perovskites at room temperature show free carriers, monomolecular recombination originating from trap-assisted processes are influenced by crystal formation processes and ensuing crystalline quality. In a direct bandgap semiconductor, the bimolecular recombination process is an intrinsic property, and its coefficient resides typically between 0.6×10^{-10} and 14×10^{-10} cm^3 s^{-1} at room temperature.[78,88,92]

Photoinduced terahertz conductivity measurements of $MAPbI_3$ and $MAPbI_{3-x}Cl_x$[88] revealed the time-resolved behavior of excitations in perovskites, identified as free charge carriers. In the presence of free charges, the measured relative change in THz electric field transmission is proportional to the photoinduced conductivity in the material. The observed dynamics can be accounted for by invoking the photoconductivity of free charges alone.

Auger recombination is a many-body process involving charge carriers and momentum transfer to another electron or hole.[93] The average range of Auger recombination values in halide perovskite is about $k_3 = (0.2-1.6) \times 10^{-28}$ cm^6 s^{-1}),[78,88,92] which is on average ~25 times higher than the Auger rate constant for GaAs.[94]

The binding energies for excitons (E_b) in perovskites have seen considerable investigation.[95−103] At room temperature, the E_b are typically lower than the thermal energy kT required to dissociate excitons. E_b in $MAPbI_3$ perovskites is sufficiently low to be classed as the Wannier−Mott type (eq 5):

$$E_n = -\frac{m_r^* e^4}{8h^2\varepsilon 0^2 \varepsilon^2}\frac{1}{n^2} = -\frac{E_b}{n^2} \tag{5}$$

From the above eq 5, $MAPbI_3$ with a bandgap energy of (~1.6 eV) has an estimated exciton binding energy in the range 2−20 meV. The range of experimentally reported values of E_b for $MAPbI_3$ is in good agreement with this, spanning 2−62 meV.[95−97,99,103] The temperature dependence of luminescence can also be used to determine the exciton binding energy. Temperature-activated exciton dissociation induces a decrease in photoluminescence by increasing temperature. Here values have ranged from E_b of 19 meV[104] to 32 meV[101] for $MAPbI_3$ and a higher 62 meV for $MAPbI_{3-x}Cl_x$.[102]

Another approach that one can use to obtain the exciton binding energy utilizes analysis of the absorption spectrum, focusing especially near the band edge.[100] From knowledge of the bandwidth of the bandedge absorption, and also when one obtains temperature-dependent measurements, one reaches the conclusion of an exciton binding energy in the range (55 ± 20) meV. A considerable diversity in E_b emerged again from the application of this method due to the incorporation of a line shape broadening process, which add to fitting uncertainties.[103] An alternative approach based on fits to the absorption spectra near the onset and normalized to a particular energy, is still sensitive to line shape broadening.[103]

Another way to measure the exciton binding energy has been reported based on high-field interband magneto-absorption measurements[99] (Figure 12). The measurements allow determination of the reduced effective mass, and this enables the study of multiple excitonic transitions for added precision.

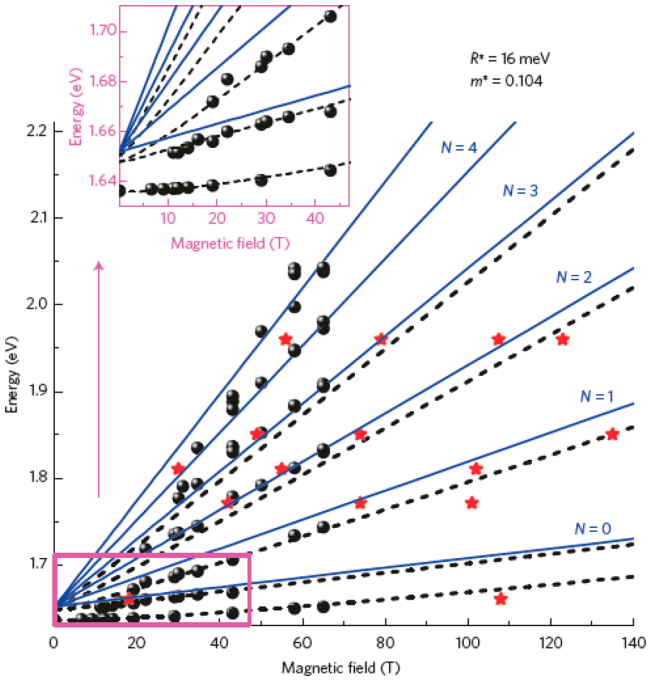

Figure 12. Measurement of exciton binding energy as a function of increase in magnetic field.[99] Reprinted with permission from ref 100. Copyright 2015, Nature Publishing Group.

In single grains of polycrystalline $MAPbI_3$ thin films, spatial heterogeneities on the nm length scale were investigated through study of free-carrier and exciton populations.[105] Using transient absorption microscopy, Harel and co-workers directly observed shifts of the bandedge absorption in different grains. Both excitons and free carriers were found to exist together but segregated on the ~100 nm scale. In the case of low-dimensional perovskites, the confinement of excitons to the wells can be accounted for via the sizable difference in dielectric constant for the organic barrier compared to the inorganic well. The exciton binding energies are high, 100s of meV, and the high radiative rate ensures that the low-dimensional perovskites are of particular interest in light-emission applications. Grozema and co-workers carried out a detailed temperature-dependent study of mobility and exciton dissociation in these materials[106] and reported an increase in charge carrier mobility when the temperature was lowered and bound excitons were favored. They saw as a result a further increase in the photoluminescence quantum yield (PLQY) at lower temperatures. This interconversion process is governed by E_b that depends strongly on the number of inorganic layers (n) in low-dimensional perovskites, ranging from ~370 to ~80 meV as a function of n from 1 to 4.

3.3. Photoluminescence Quantum Yield

Measurements of the PLQY of high refractive index materials, such as thin films of polymeric semiconductors, take account of the angular distribution of emission, reflectivity, and absorbance. Adding to this complication are optical interference effects and potential photon recycling (reabsorption of emitted photons) that can occur in metal halide perovskites. A quantitative measurement of external PL efficiency[107] η is defined as

$$\eta = \frac{\text{number of photons emitted}}{\text{number of photons absorbed}}$$

DOI: 10.1021/acs.chemrev.9b00107
Chem. Rev. 2019, 119, 7444−7477

The power-dependent PLQY of thin films of $MAPbI_{3-x}Cl_x$ perovskites on glass were particularly revealing.[108] The PLQY grew to an impressive 70% at high power excitation (100 mW/cm^2), a result of radiative outcompeting nonradiative recombination: bimolecular radiative recombination dominated at the higher excitation intensities and defects became filled.

A variety of approaches have been applied to maximize PLQY, including strategies seeking to increase E_b and the oscillator strengths of the excitons. Charge confinement was introduced in $MAPbBr_3$ by reducing the grain size, which increased the radiative rate, and 36% PLQY was achieved in the visible region at 530 nm[13]. In the 2D PEA_2PbI_4 perovskites, the PLQY was as low as 1% at room temperature, ascribed to thermal quenching of excitons.[40,41] Mixed-phase low-dimensional perovskites exhibit much higher PLQY and LED performance at room temperature.[41,42,44] Surface traps in perovskite NCs can cause a low PLQY, and passivating halide-ion pair ligands has been shown to improve performance.[109] Near unity PLQY for $CsPbI_3$ perovskite NCs reported by Liu et. al were achieved by improving a synthetic protocol that involves the use of trioctylphosphine, an approach that also improved stability for the resulting $CsPbI_3$ NC solutions.[110]

4. PEROVSKITE LIGHT EMITTING DIODES (LEDS)

4.1. Perovskite Material Engineering for LEDs

Material engineering of perovskites is crucial to achieve highly luminescent PL properties; a material's crystal structure, composition, domain size, and surface chemistry all influences optical properties. Below, we discuss the effect of each on fundamental optical properties and also device-level performance (Table 1).

4.1.1. Modulating Dimensionality in Perovskite for LEDs. In the early 1990s, the Nurmikko and Saito groups[11,39,111] reported LEDs based on layered perovskites. The authors used a layered perovskite composition $(C_6H_5C_2H_4NH_3)_2PbI_4$ and measured the electroluminescence (EL) spectrum at liquid nitrogen temperatures ∼77 K (Figure 13). An increased scattering rate due to phonons at higher temperatures accounted for the observed thermal quenching.

In 2014, Friend and co-workers[12] reported room-temperature perovskite LEDs based on $CH_3NH_3PbI_{3-x}Cl_x$ having an EQE of 0.76% and radiance of 13.2 W sr^{-1} m^{-2} at a current density of 363 mA cm^{-2}. Lee and co-workers reported perovskite LEDs based on $MAPbBr_3$ and exhibiting a current efficiency (CE) of 0.577 cd A^{-1}, an EQE of 0.125%, and a maximum luminance of 417 cd m^{-2} (Figure 14).[112] Multicolored LEDs were demonstrated by leveraging the mixing of halides ($CH_3NH_3PbCl_xBr_yI_{3-x-y}$). The perovskite thin films were thin enough to confine electrons and holes for bimolecular recombination, enhancing electron−hole capture and increasing radiative recombination. Making pinhole-free films containing crystalline particles, with overall thickness less than 50 nm, was a challenge. One method to overcome this film-formation challenge is to blend the perovskite precursors with a polymer that is also soluble in the solvents needed to process the metal halide and ammonium halide salts. For example, Li et al. blended perovskites with insulating polyimide and deposited uniform thin films.[113] The perovskite grains provided for charge transport and light emission, while the dielectric polymer filled the surrounding pinholes and thus filled potential shunt paths. A similar approach with mixed perovskite/poly(ethylene oxide) films also facilitated perovskite film formation, producing LEDs with relatively high brightness (4,064 cd m^{-2}).[114] As the presence of metallic Pb atoms in $MAPbBr_3$ has been offered as a cause of trap-induced nonradiative recombination, Lee and co-workers addressed the film nonuniformity issue by providing excess MABr, reducing grain size and suppressing exciton quenching (Figure 15).[13] The spatially confined $MAPbBr_3$ grains (average diameter of ≤100 nm) were formed by a NC pinning process with additional TPBi (2,2′,2″-(1,3,5-benzinetriyl)-tris(1-phenyl-1*H*-benzimidazole)) dissolved in the solvent used for the antisolvent quench. Perovskite LEDs based on this approach had a maximum current efficiency of 43 cd A^{-1} corresponding to an EQE of 8.5%. Park et al. further investigated the introduction of TPBi diluted in a volatile nonpolar solvent during the perovskite NC pinning process.[115]

Mixed Cs and FA cation perovskite LEDs developed by Cho et al. incorporated Cs^+ cations in $FAPbBr_3$ to reduce significantly the average grain size (from a wide 100−600 nm distribution to a more tightly controlled average of 200 nm for FA:Cs = 90:10) and trap density and increased the PLQY and PL lifetime in $FA_{1-x}Cs_xPbBr_3$ films and, correspondingly, the device performance increased from 1.7 to 3.1%. Incorporation of Cs also increased photostability of $FA_{1-x}Cs_xPbBr_3$ films due to the suppression of light-induced metastable states.[116]

Further exciton and carrier confinement was achieved using low-dimensional perovskites, as reported by Yuan et al., who used a perovskite composed of a series of differently quantum-size-tuned grains that funneled photoexcitations to the lowest-bandgap emitters in the mixture upon photoexciation[41] (Figure 16). Quasi-2D perovskites with a composition of $PEA_2(CH_3NH_3)_{n-1}Pb_nI_{3n+1}$ (PEA = $C_8H_9NH_3$) were used to tune the average layer numbers $\langle n \rangle$ by changing the ratio between PEAI and CH_3NH_3I. Transient absorption (TA) and time-resolved PL spectroscopy enabled characterization of transport and recombination dynamics at ultrafast time scales. These studies of excitation dynamics revealed how multi-phased perovskite materials channel energy across an inhomogeneous energy landscape, concentrating excitons into the smaller-bandgap emitters (larger n). Perovskite LEDs with $\langle n \rangle = 5$ perovskite exhibited the best performance within this study, with an EQE of 8.8% and radiance of 80 W sr^{1-} m^{-2}, emission at wavelength 750 nm.

The energy landscape in quasi-2D perovskites was further engineered by manipulating the crystallization process. Quan et al. tailored the composition of mixed-bandgap perovskites to direct energy transfer into the lowest-bandgap minority phase, a process that occurred faster than loss due to nonradiative centers, thus helping to increase PLQY.[44] By optimizing the domain distribution, the authors achieved a high PLQY of 60% at low excitation fluences (1.8 mW cm^{-2}) in materials exhibiting green emission.

Multiple quantum well strategies explored by Wang et al. used a mixture of 1-naphthylmethylammonium iodide (NMAI) and formamidinium iodide (FAI)[43,117] (Figure 17). The mixed material showed a high PLQY of 60% because photogenerated excitons in small-n quantum wells (QWs) were efficiently energy-transferred to large-n QWs. The mixed QWs perovskite LEDs achieved narrow emission peaks at 736, 685, 664, 611, or 518 nm via Br:I ratio tuning. The best-performing perovskite LEDs turned on at 1.3 V, and the devices achieved an EQE of 11.7% at 2.6 V with a current

DOI: 10.1021/acs.chemrev.9b00107
Chem. Rev. 2019, 119, 7444−7477

Table 1. Device Performance of Perovskite LEDs (from Blue to Near-Infrared Wavelengths)

perovskite materials	device structure	EL wavelength (nm)	max EQE (%)	max brightness (cd m^{-2}) R_{max} (W sr^{-1} m^{-2})	ref
	Blue				
$(PEA)_2PbBr_4$	ITO/PEDOT:PSS/perov/TPBi/Ca/Al	410	0.04		141
IPA:PEA_2MA:$Cs_{n-1}Pb_nBr_{3n+1}$	ITO/PEDOT:PSS/perov/TPBi/LiF/Al	490	1.5	2480	142
$Cs_{10}MA_{0.17}FA_{0.83}Pb(Cl_{1-x}Br_x)_3$	ITO/ZnO/perov/NPD/MoO_3/Al	475	1.7	3567	143
$CsPbX_3$ NCs	ITO/PEDOT:PSS/PVK/perov/TPBi/LiF/Al	490	1.9	35	144
$CsMnPb(Br_{1-x}Cl_x)_3$	ITO/PEDOT:PSS/TFB:PFI/perov/TPBi/LiF/Al	466	2.12	245	145
$CsPbCl_{0.9}Br_{2.1}$	ITO/PEDOT:PSS/perov/TPBi/LiF/Al	480	5.7	3780	146
	Green				
$MAPbBr_3$	ITO/PEDOT:PSS:PFI/perov/TPBi/LiF/Al	540	0.13	417	147
$MAPbBr_3$:PIP	ITO/PEDOT:PSS/perov/F8/Ca/Ag	534	1.2	200	148
$FAPbBr_3$	ITO/ZnO/perov/poly-TPD/MoO_3/Al	540	1.16	13062	149
$CsPbBr_3$/PEO	ITO/PEDOT:PSS/perov/TPBi/LiF/Al	521	4.26	53525	150
$CsPbBr_3$NCs	ITO/PEDOT:PSS/poly-TPD/perov/TPBi/LiF/Al	515	6.27	15000	151
$Cs_{10}MA_{0.17}FA_{0.83}Pb(Br_{1-x}I_x)_3$	ITO/ZnO/perov/NPD/MoO_3/Al	569	7.3	19420	115
$(PEABr)_{0.2}$ $MAPbBr_3$	ITO/PVK/perov/TPBi/LiF/Al	515	7.0	11400	152
$MAPbBr_3$	Glass/PEDOT:PSS:PFI/perov/TPBi/LiF/Al	542	8.53	10000	153
$(BABr)_{0.2}MAPbBr_3$	ITO/PVK/perov/TPBi/LiF/Al	513	9.3	2900	42
$Cs_{0.87}MA_{0.13}PbBr_3$	ITO/ZnO/PVP/perov/CBP/MoO_3/Al	520	10.43	91000	135
$MAPbBr_3$/phenylmethylamine	ITO/PEDOT:PSS/perov/TPBi/LiF/Al	535	12.1	55400	154
$MAPbBr_3$NCs	ITO/PEDOT:PSS/perov/B3PYMPM:TPBi/B3PYMPM: Cs_2CO_3 /Al	524	12.9	22830	155
$(OA)_2(FA)_{n-1}Pb_nBr_{3n+1}$ and $FAPbBr_3$	ITO/PEIE/perov/PO-T2T/Ca/Al	530	13.4	56143	129
$PEA_2CsPb_2Br_7$	ITO/PVK/perov/TPBi/LiF/Al	512	13.9	8789	156
$PEA_2(FAPbBr_3)_{n-1}PbBr_4$	ITO/PEDOT:PSS/perov/TPBi/LiF/Al	530	14.36	14000	157
$CsPbBr_3$/PEABr/polyethylene glycol	ITO/PEDOT:PSS/perov/TPBi/LiF/Al	514	13.14	45990	158
$CsPbBr_3$/PEABr/1,4,7,10,13,16-hexaoxacyclooctadecane	ITO/poly-TPD/perov/TPBi/LiF/Al	510	15.5	7000	159
$CsPbBr_3$/PPABr NCs	ITO/PEDOT:PSS/PVK/perov/TPBi/LiF/Al	512	15.2	18600	160
$CsPbBr_3/ZnBr_2$ NCs	ITO/PTAA/PVK/perov/TPBi/LiF/Al	518	16.5	76940	161
$CsPbBr_3$/MABr	ITO/PEDOT:PSS/perov/PMMA/B3PYMPM/TPBi/LiF/Al	525	20	14000	162
	Red				
$CsPbI_3$NCs	ITO/ZnO/perov/TFB/MoO_3/Ag	698	5.7	206	163
$CsPbI_{2.25}Br_{0.75}$NCs	ITO/ZnO/perov/TFB/MoO_3/Ag	619	1.4	1559	163
$MAPbI_{1.05}Br_{1.95}$	ITO/PEDOT:PSS/perov Ca:ZnO/Ca/Al	635	5.8	1000	164
$CsPbI_3$/Ag doped NCs	ITO/PEDOT:PSS/perov/TCTA/MoO_3/Au	690	11.2	1106	165
$CsPbI_3$/Sr doped NCs	ITO/ZnO/PEI/perov/TCTA/MoO_3/Au	691	13.5	1152	166
$CsPbBr_xI_{3-x}$	ITO/PEDOT:PSS/poly-TPD/peorv/TPBi/LiF/Al	649	21.3	794	167
	NIR				
$MAPbI_{3-x}Cl_x$	ITO/TiO_2/perov/F8/MoO_x/Au	773	0.76	^{R}13.2	168
$MAPbI_{3-x}Cl_x$	ITO/ZnO/PEIE/perov/TFB/MoO_x/Au	768	3.5	^{R}28	169
$(FPMAI)_{0.2}$ $MAPbI_3$	ITO/polyTPD/perov/TPBi/LiF/Al	749	7.9	^{R}72	152
$PEA_2MA_4Pb_5I_{16}$	ITO/TiO_2/perov/F8/MoO_x/Au	750	8.8	^{R}80	170
$(BAI)_{0.2}MAPbI_3$	ITO/polyTPD/perov/TPBi/LiF/Al	748	10.4	^{R}30	42
$FAPbI_3$/5AVA	ITO/ZnO:PEIE/perov/TFB/MoO_x/Au	800	20.7	^{R}390	171

DOI: 10.1021/acs.chemrev.9b00107
Chem. Rev. 2019, 119, 7444−7477

Table 1. continued

perovskite materials	device structure	EL wavelength (nm)	max EQE (%)	max brightness (cd m^{-2}) R_{max} (W sr^{-1} m^{-2})	ref
	NIR				
$FAPbI_3$/EDEA	ITO/ZnO:PEIE/perov/TFB/MoO_3/Au	800	21.6	[R]308	172

[a]ITO = indium tin oxide; PEDOT:PSS = poly(3,4-ethylenedioxythiophene:polystyrenesulfonate); TPBi = [2,2′,2″-(1,3,5-benzinetriyl)-tris(1-phenyl-1*H*-benzimidazole)]; PEIE = polyethylenimine ethoxylated; TFB = poly(9,9-dioctylfluorene-*alt*-*N*-(4-s-butylphenyl)-diphenylamine); NPD = *N*,*N*′-bis(naphthalen-1-yl)-*N*,*N*′-bis(phenyl)benzidine; poly-TPD = poly(4-butylphenyl-diphenyl-amine); CBP = 4,4-*N*,*N*′-dicarbazole-1,1′-biphenyl; B3PYMPM = 4,6-bis(3,5-di(pyridin-3-yl)phenyl)-2-methylpyrimidine; TPD = *N*,*N*′-bis(3-methylphenyl)-*N*,*N*′-diphenylbenzidine; PVK = poly(9-vinylcarbazole); PPA = Br-phenylalanine bromide; EDEA = 2,2′-(ethylenedioxy)diethylamine; TCTA = 4,4,4″-tris(carbazol-9-yl)triphenylamine; SAVA = 5-aminovaleric acid; R = radiance.

density of 38 mA cm^{-2} with an emission peak at 763 nm. Grain size engineering was further explored by Xiao et. al.[42] Ammonium halides were added to the stoichiometric 3D perovskites, and these acted as surfactants that constrained the growth of 3D perovskites during film crystallization, resulting in perovskite grains exhibiting dimensions as small as 10 nm and ultrasmooth films with roughness of less than 1 nm (Figure 18). These nanometer-sized perovskite grains coated with longer-chain organic cations (butylammonium halides) yielded efficient perovskite emitters: the resulting LEDs operated with EQEs of 10.4% and 9.3% for perovskite films based on $MAPbI_3$ and $MAPbBr_3$, respectively. They also featured significantly improved device stability. The self-assembled long-chain butylammonium cations at the crystallite surface impeded ion migration during device operation, significantly reducing hysteresis.

For pure red-emitting ($\lambda \approx 650$ nm) perovskite LEDs, mixed halides (Br/I) allow the needed tuning of the electronic bandgap. However, because of instability of MA and FA iodide/bromide perovskites,[118] new approaches have been sought to suppress halide redistribution. These include the use of self-assembled large group ammonium capping layers at nanometer-sized grain surfaces.[34] In mixed halide perovskite films, halide migration is suppressed by nanometer-sized grains and the use of long organic ligands as capping layers. Stable mixed-halide perovskite films enable fabrication of efficient and wavelength-tunable perovskite LEDs spanning the infrared to the green. Sneha et al. tailored 3D perovskites to provide a near-monodispersed nanoparticle film prepared using a one-step in situ deposition method.[119] Partially replacing MABr with OABr (octylammonium bromide; $CH_3(CH_2)_7NH_3Br$) in the perovskite precursor solution enabled controlled nanoparticle formation. An improved maximum brightness of L_{max} = 4578 cd m^{-2} was achieved using this strategy.

4.1.2. Colloidally-Synthesized Perovskite NCs for LEDs. Kovalenko and co-workers pioneered all-inorganic cesium lead halide ($CsPbX_3$; X = Cl, Br, and I) NCs, which exhibited excellent optical properties with tunable bandgap and high PLQY[120] (Figure 19).

Tan and co-workers applied a cross-linking method to stabilize perovskite NC films. They were able as a result to deposit charge-injection layers but prevent damage to the perovskite layer.[121] The perovskite film showed excellent coverage, and efficient confinement of injected electron−holes led to an EQE of 5.7%.

Song et al. then reported perovskite LEDs that utilized $CsPbX_3$ NCs. High-quality $CsPbX_3$ NCs were synthesized via the hot injection of the cesium precursor into a $PbBr_2$ precursor solution at high temperature.[122] The emission wavelength was tuned through both perovskite NC size and halide composition (Cl, Br, and I). Quantum yields were impressive, in the range 60%−90%, especially strong in the case of the $CsPbBr_3$ films. In the blue, green, and orange spectral regions, LEDs based on a ITO/PEDOT:PSS/PVK/NCs/TPBi/LiF/Al (PVK, poly(9-vinylcarbazole); TPBi, PEDOT:PSS, (poly(ethylenedioxythiophene):polystyrenesulfonate)) stack led to perovskite NC LEDs having a highest luminances of 528 cd m^{-2}, with EQE of 0.09%. The insulating organic ligands on the surface of NCs suppressed, in these early studies, the efficient injection of current, accounting for these initial device performance levels.

Replacing these long ligands (usually oleylamine (OAm) and oleic acid (OA), used for protecting the surface of

DOI: 10.1021/acs.chemrev.9b00107
Chem. Rev. 2019, 119, 7444−7477

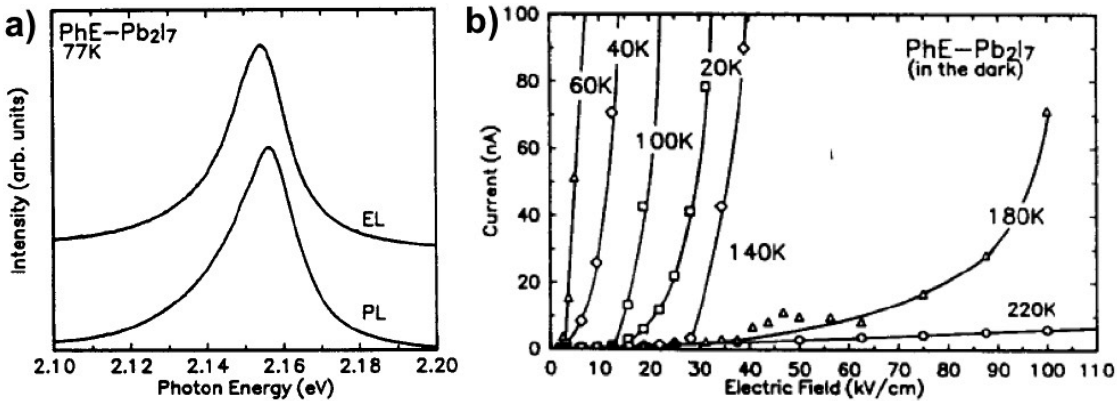

Figure 13. (a) Electroluminescence and photoluminescence spectra of perovskite LEDs with $n = 2$ layered perovskites. (b) Current along the well plane as a function of electric field for PhE-Pb_2I_7 perovskite at different temperatures.[39] Reprinted with permission from ref 39. Copyright 1992, Elsevier.

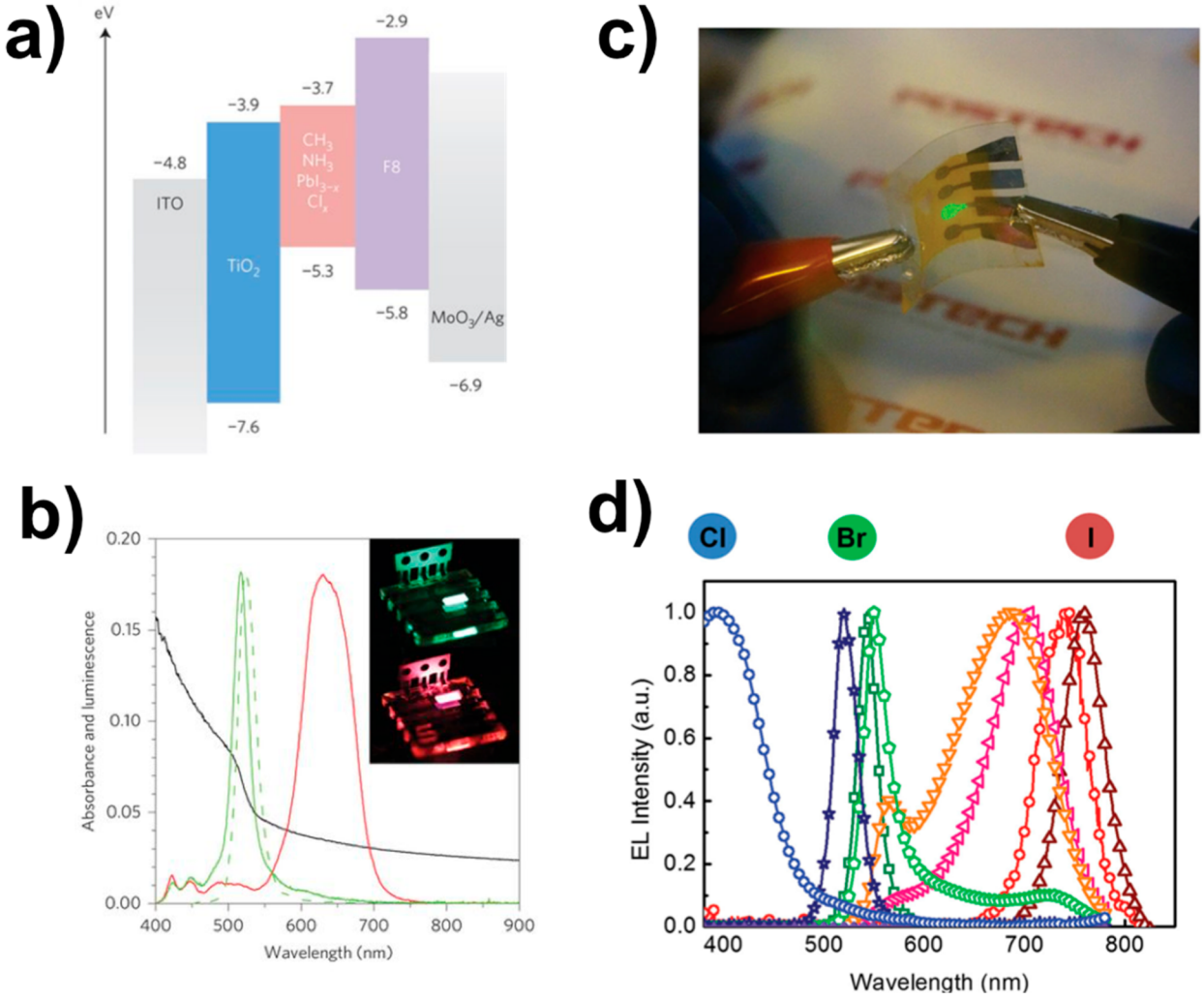

Figure 14. (a) Device architecture of $CH_3NH_3PbI_{3-x}Cl_x$ perovskite LEDs. (b) Electroluminescence spectrum of perovskite LED with $CH_3NH_3PbBr_2I$.[12] Reprinted with permission from ref 12. Copyright 2014 Nature Publishing Group. (c) Photograph of perovskite LEDs on flexible PET substrate during bending. (d) Electroluminescence spectra of perovskite LEDs with $CH_3NH_3PbCl_xBr_yI_{3-x-y}$.[112] Reprinted with permission from ref 115. Copyright 2015 Wiley-VCH.

$CsPbX_3$), with shorter ligands, remains a challenge: it is imperative to achieve this without degrading or destabilizing perovskite NC films. Pan et al. realized increased stability of $CsPbX_3$ NCs capped by using a halide ion pair (didodecyl dimethylammonium bromide (DDAB)), a relatively short ligand that facilitates carrier transport in NC films and enhances thereby LED device performance.[109] The ligand-exchange strategy included an intermediate step to desorb

DOI: 10.1021/acs.chemrev.9b00107
Chem. Rev. 2019, 119, 7444−7477

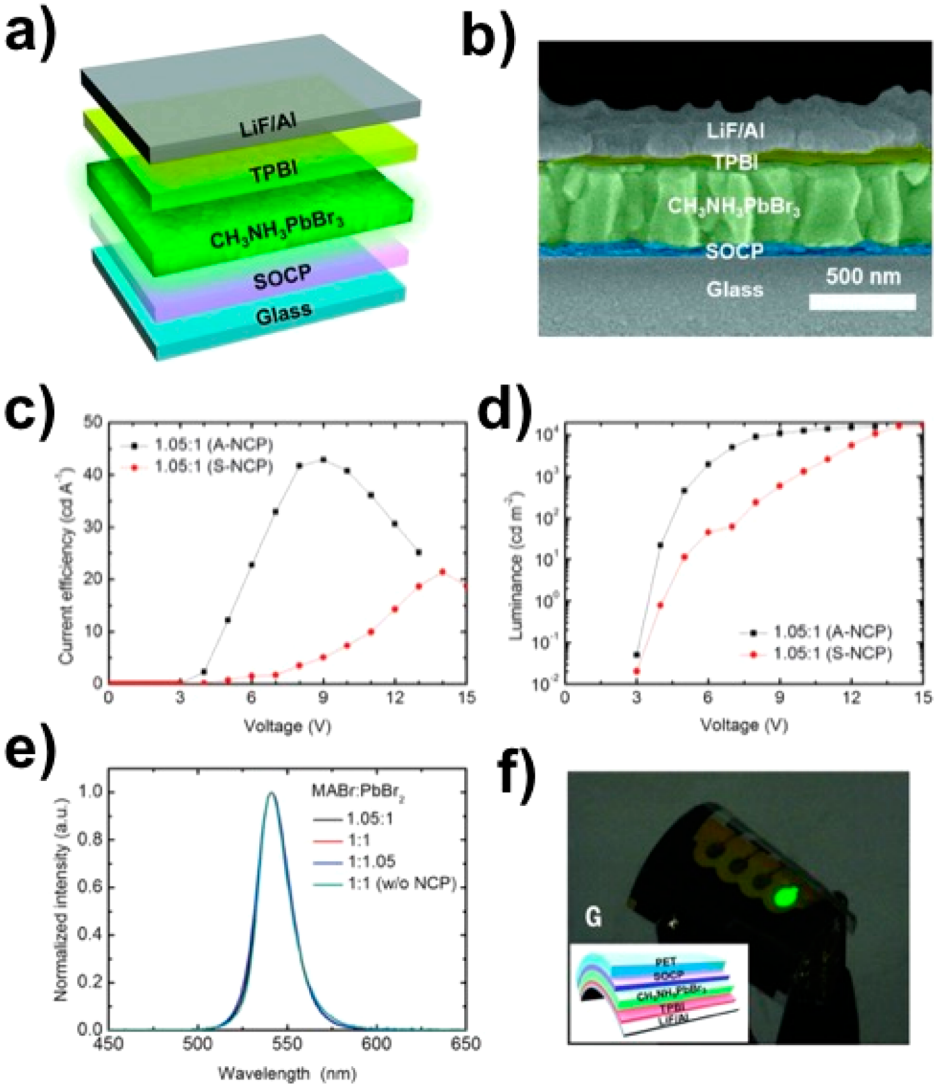

Figure 15. (a) Device structure of perovskite LEDs and (b) cross-sectional SEM image of perovskite LEDs. (c,d) Current efficiency and luminance efficiency as a function of voltage in perovskite LEDs based on grainsized controlled $MAPbBr_3$. (e) EL spectra of perovskite LEDs. (f) Photograph of a flexible perovskite LEDs and (g) its device structure.[13] Reprinted with permission from ref 13. Copyright 2015 AAAS.

protonated OAm. As a result of new ligand-exchange strategies, halide-ion-pair-capped $CsPbBr_3$ NCs have enabled fabrication of LEDs with the device structure indium tin oxide (ITO)/PEDOT:PSS/poly(9-vinylcarbazole)/NCs/TPBi/LiF/Al and achieved a maximum EQE and luminance of 3% and 330 cd m^{-2}, respectively.

Further progress toward $CsPbBr_3$ perovskite NC LEDs was made by Zeng and co-workers, who balanced surface passivation and carrier injection by controlling ligand density on perovskite NCs.[123] Using a hexane/ethyl acetate mixed solvent system, the authors controlled the surface ligand density: excess ligands had previously led to films with poor carrier injection and transport in devices, while insufficient ligands caused the NCs to have low PLQY and poor stability. The mixture of hexane/ethyl acetate was found to achieve improved control over the ligand density on NC surfaces, mainly due to the relationship between the polarity of solvents and the ionicity of perovskites. Perovskite NC LED performance reached >6% in EQE and an emission peak of 512 nm. Mixed-cation strategies in perovskites have also employed NCs based on $FA_{(1-x)}Cs_xPbBr_3$:[124] the composition $FA_{0.8}Cs_{0.2}PbBr_3$ led to LEDs exhibiting an increased luminance of 55000 cd m^{-2} and a current efficiency exceeding 10 cd A^{-1}.

Most recently, core−shell $CsPbBr_3$ films were created using one-step precursor coating.[125] The QDs were of small size (4.5 nm) and thus confined injected electron−holes. This enables green perovskite LEDs with EQE exceeding 15%.

Red-emitting $CsPbI_3$ NCs have shown phase transformation into a nonluminescent, wide-bandgap 1D polymorph phase, and $MAPbI_3$ exhibits poor chemical stability. Seeking to overcome this issue, Kovalenko and co-workers pursued a facile colloidal synthesis that led to $FAPbI_3$ and FA-doped $CsPbI_3$ NCs having a uniform size distribution. These exhibited dramatically higher robustness than the corresponding MA and Cs, with only perovskites having similar sizes and morphologies.[126] The $FAPbI_3$ NCs have shown a cubic crystal structure, while the $FA_{0.1}Cs_{0.9}PbI_3$ NCs had an orthorhombic structure and the PLQY reached 70% and spanned the red (690 nm, $FA_{0.1}Cs_{0.9}PbI_3$) and near-infrared (780 nm, $FAPbI_3$) regions. The PLQY was stable for several months, both in the colloidal state and in films. An EQE of 2.3% at current density 0.67 mA cm^{-2} was achieved in these $FAPbI_3$ NC LEDs.

DOI: 10.1021/acs.chemrev.9b00107
Chem. Rev. 2019, 119, 7444−7477

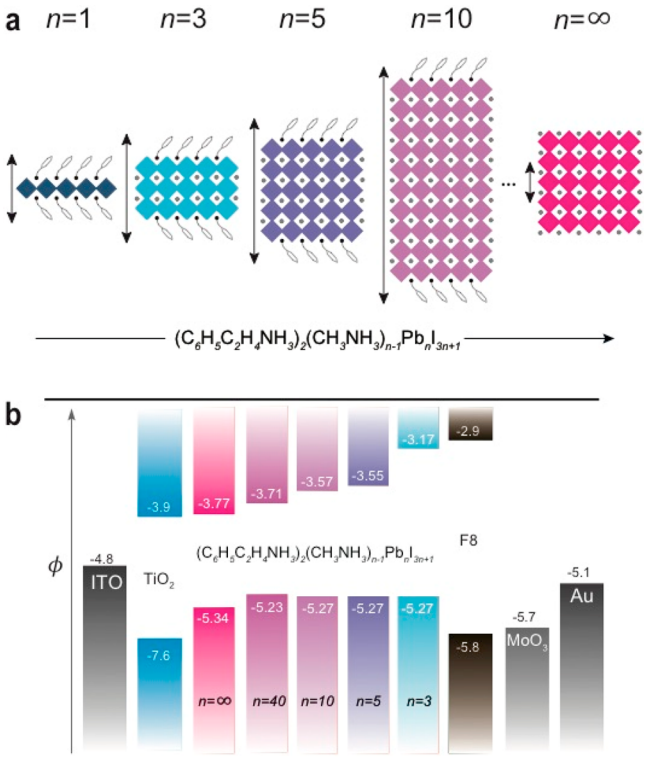

Figure 16. (a) Schematic illustration of $(C_8H_9NH_3)_2(CH_3NH_3)_{n-1}Pb_nI_{3n+1}$ perovskite structure with different $\langle n \rangle$ values, from 2D (n = 1) to 3D (n = ∞). (b) Electronic bandstructure of perovskites with different $\langle n \rangle$ values, and electronic bandstructure of each layer used in LEDs, ϕ, electric potential.[41] Reprinted with permission from ref 41. Copyright 2016 Nature Publishing Group.

Organic–inorganic hybrid based NCs have also been advanced in LEDs. Perovskites based on formamidinium lead bromide perovskite ($FAPbBr_3$) nanoparticles were improved with the aid of surface engineering.[127] Work with the surface ligand in nanocrytals allowed researchers to improve the charge injection in LEDs. They provided a current efficiency of 9 cd/A in an LED, an important milestone. Researchers also advanced $MAPbBr_3$ nanoparticles having dimensions exceeding the exciton Bohr diameter (BD, regime beyond quantum size) by using a multifunctional buffer hole injection layer.[128] These led to PLQYs exceeding 60% and did not rely on complex post-treatments nor multilayers. They gave an impressive current efficiency of 15.5 cd/A.

Self-assembly of 3D $FAPbBr_3$ NCs of graded size (mixed microplatelets of octylammonium lead bromide perovskites) were synthesized by Chin et al., enabling an energy cascade that yielded high efficiencies in green-emitting LEDs[129] (Figure 20). Transient optical spectroscopy revealed an energy cascade from high-bandgap 2D $(OA)_2(FA)_{n-1}Pb_nBr_{3n+1}$ platelets into progressively lower-bandgap $FAPbBr_3$ NCs, giving rise to high luminescence efficiency. Mesoscopic thin films comprising large plate-like domains of $(OA)_2(FA)_{n-1}Pb_nBr_{3n+1}$ were sandwiched between electron and hole transporting layers that enabled an EQE of 13.4% and 56000 cd m^{-2} luminance.

4.2. Engineering Perovskite LEDs toward High Efficiency

Numerous approaches used to improve perovskite LED efficiency, in addition to those focused on enhancing PLQY and/or film morphology or composition, have relied on improving electron and/or hole injection. We discuss strategies that improve perovskite LEDs by engineering interfacial layers in device structures and differences of perovskite LEDs compared with alternative thin film quantum dot LEDs (QLEDs) and organic LEDs (OLEDs).

4.2.1. Engineering Interfacial Layers. In the early stage of developing perovskite LEDs, device architectures were inspired from perovskite solar cells: they often employed ITO/TiO_2/perovskite/F8(poly(9,9′-dioctylfluorene)/MoO_3/Ag and also leveraged inverted structures such as ITO/PEDOT:PSS/perovskite/TPBi/LiF/Al (Figure 21). Wide-bandgap ZnO NCs have been employed as electron-transporting/hole-blocking layers in solar cells and LEDs because of the combination of high electron mobility, excellent optical transparency, and a deep valence-band energy level. However, perovskites deposited atop ZnO decompose due to the residual hydroxyl groups and acetate ligands on the surface of alkaline ZnO.[130]

Wang et al. developed perovskite LED structures that incorporate a multifunctional polyethylenimine (PEI) interlayer between the electron transporting layer (ETL) and the perovskite layer.[131] Deposition of the PEI interlayer on top of ZnO following washing with *N*,*N*-dimethylformamide (DMF) enhanced the quality of the perovskite film during crystallization. The structure ultimately combined (ITO)/PEI-modified zinc oxide (ZnO, 20 nm)/$CH_3NH_3PbI_{3-x}Cl_x$ (50 nm)/poly(9,9-dioctyl-fluorene-*co*-*N*-(4-butylphenyl)-diphenylamine)(TFB, 25 nm)/molybdenum oxide (MoOx, 8 nm)/gold (Au, 100 nm). Using this interfacial engineering approach, the authors achieved green-emitting perovskite LEDs exhibiting a maximum luminous efficiency of 4.0 lm W^{-1} at a maximum luminance of 20 000 cd m^{-2} and a low voltage of 2.8 V.

The low efficiency observed in perovskite LEDs was traced to high leakage current due to poor perovskite morphology and also to high nonradiative recombination at interfaces and perovskite grain boundaries that led to imbalanced charge injection. Zhang et al. incorporated a small amount of MA into the $CsPbBr_3$ lattice and also deposited a hydrophilic and insulating polyvinylpyrrolidine atop the ZnO electron-injection layer, all to overcome these issues.[135] Perovskite LEDs that used this strategy exhibited a high brightness of 91000 cd m^{-2} and an EQE of 10.4% when the mixed-cation perovskite $Cs_{0.87}MA_{0.13}PbBr_3$ was used as the emitting layer. The polymer buffer layer and the MABr additive significantly reduced the injection current in device, suppressed current leakage, and enhanced charge injection balance. The turn-on voltage was also slightly increased after inserting a (thin but insulating) polymer buffer layer.

A suitably designed *n*-type semiconductor consisting of Ca-doped ZnO nanoparticles was then developed for use as the electron transport layer in perovskite NC LEDs. The bandstructure of ZnO was modulated via Ca doping, creating a cascade of conduction energy levels from the cathode to the perovskite. The electron mobility was observed to increase progressively with increased doping of Ca in the ZnO nanoparticles. The carrier mobility in undoped ZnO was found to be 2.4×10^{-3} cm^2 V^{-1} s^{-1} and increased with the Ca doping level to a peak value of $\mu_{max} = 5.7 \times 10^{-2}$ cm^2 V^{-1} s^{-1} at 50% doping. Red-emitting perovskite LEDs exhibited significantly improved luminance with 19 cd A^{-1} and EQE of 5.8%.

DOI: 10.1021/acs.chemrev.9b00107
Chem. Rev. 2019, 119, 7444−7477

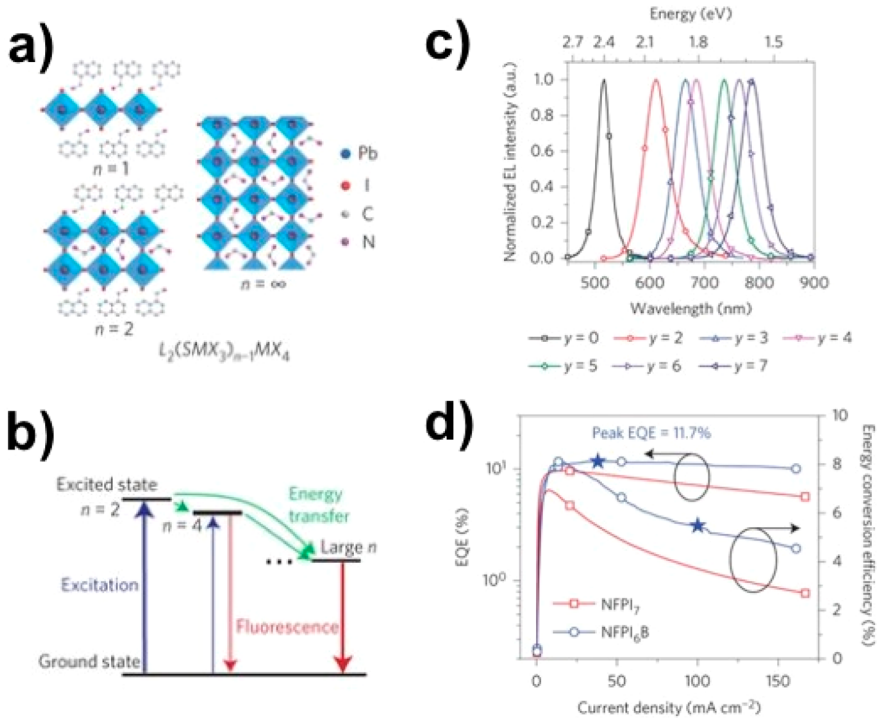

Figure 17. (a) Schematic representation of layered lead halide perovskites with $n = 1$, $n = 2$, and $n = \infty$. (b) Schematic of cascade energy transfer in multiquantum well perovskites. Excitation energy is transferred downhill from smaller-n quantum wells to larger-n quantum wells, and the emission is mainly from larger-n quantum wells. (c) EL spectra of MQW LEDs based on the $NFPI_yB_{7-y}$ films, $y = 0$, 2, 3, 4, 5, 6, and 7, respectively. (d) EQE and energy conversion efficiency versus current density.[43] Reprinted with permission from ref 43. Copyright 2016 Nature Publishing Group.

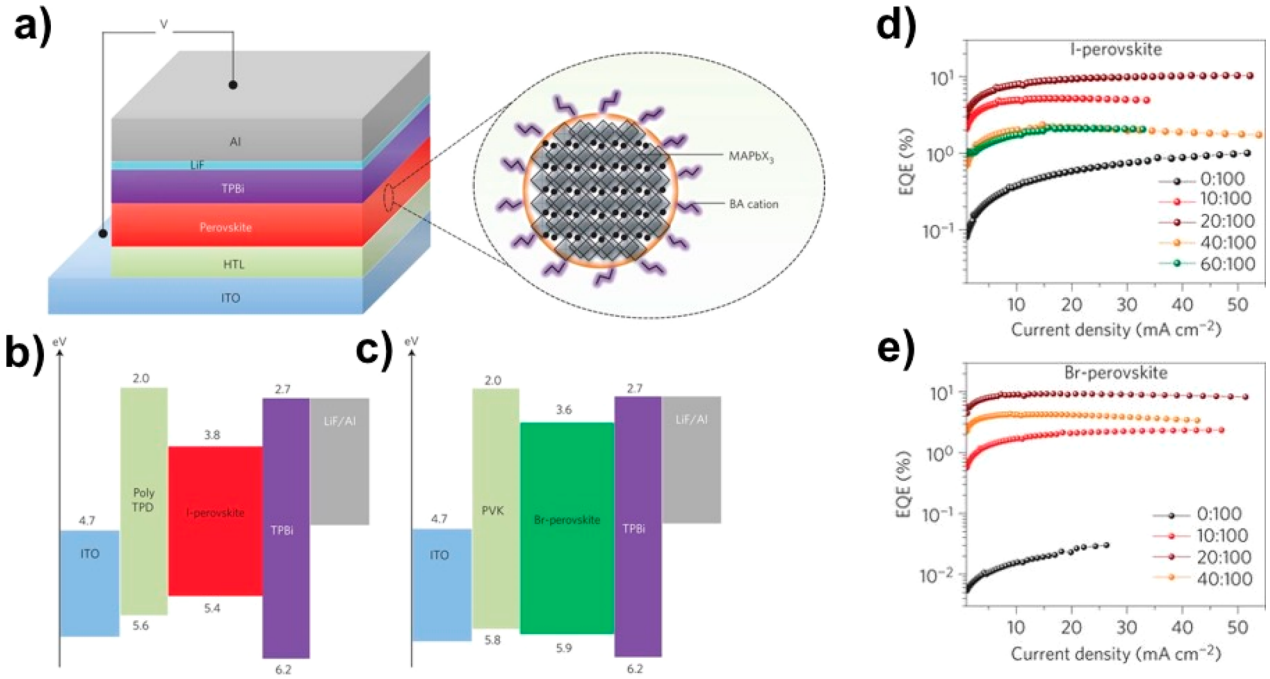

Figure 18. (a) Device structure of perovskite LEDs with nanometre-sized perovskite grains. (b,c) Energy diagram of I-perovskite and Br-perovskite LEDs. (d) Device performance of I-perovskite LEDs with different BAI:$MAPbI_3$ molar ratios. (e) Device performance of Br-perovskite LEDs with different BABr:$MAPbBr_3$ molar ratios.[42] Reprinted with permission from ref 42. Copyright 2016 Nature Publishing Group.

In the inverted device structure, TPBi is a widely employed electron injection layer. Yan and co-workers used the blended electron injection layer B3PYMPM (4,6-bis(3,5-di(pyridin-3-yl)phenyl)-2-methylpyrimidine) and TPBi to tune the energy barrier between the ETL and the perovskite.[136] In devices with TPBi as an ETL, the low electron conductivity (4.2×10^{-10} S cm^{-1}) and high energy barrier for electron injection caused by the high LUMO level of TPBi led to a higher driving voltage than in the B3PYMPM ETL device. Perovskite LEDs (PeLEDs) with mixed ETLs showed reduced driving current

DOI: 10.1021/acs.chemrev.9b00107
Chem. Rev. 2019, 119, 7444−7477

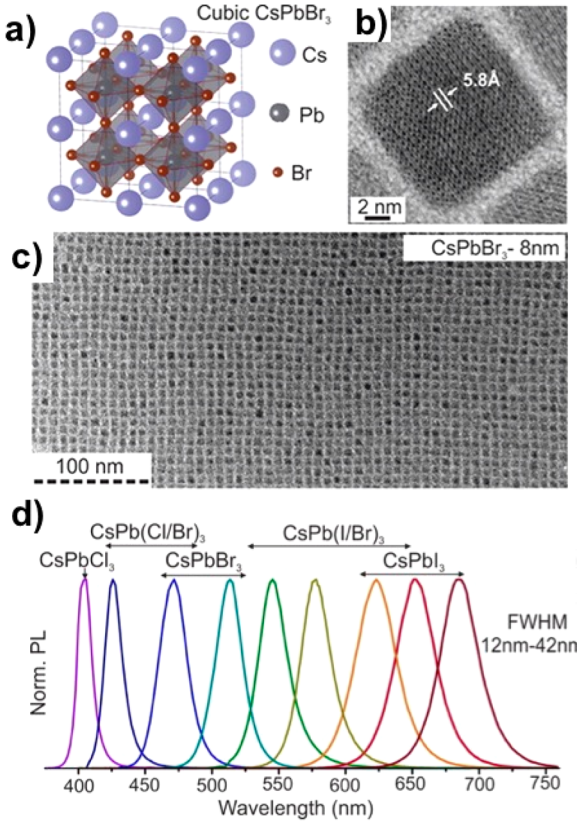

Figure 19. (a) Schematic of the perovskite structure. (b,c) Transmission electron microscopy (TEM) images of $CsPbBr_3$ NCs. (d) Representative PL spectra of different halide perovskite NCs.[120] Reproduced from ref 123. Copyright 2015 American Chemical Society.

density and an EQE_{max} of 12.9%, with a high η_{max} of 30.4 lm W^{1-} at high brightness above 1000 cd m^{-2}.

The judicious selection of hole transporting layers is important to balance charge injection and to form an ohmic contact with the active layer. The polymer F8, which has a deep ionization potential and a shallow electron affinity, was used to confine holes within the perovskite active layer, blocking electron losses. The high-work function MoO_3/Ag anode provided ohmic hole injection into the device.[137] Many perovskite LEDs and solar cells rely on expensive, unstable, and low-conductivity fluorenes for charge transport, such as spiro-OMeTAD (2,2′,7,7′-tetrakis(*N*,*N*-di-*p*-methoxyphenylamine)-9,9′-spiro-bifluorene) or F8.[138] Exploring new electrode materials that overcome these limitations is an important challenge. Dan and co-workers used atomic layer-deposited ZnO films that formed at 60 °C and were deposited directly onto $MAPbBr_3$ perovskite.[139] The electron injection barrier with the perovskite was reduced by incorporating Mg into ZnO to produce $Zn_{1-x}Mg_xO$. This decreased the electron affinity from −3.6 to −3.35 eV relative to vacuum and reduced the LED turn-on voltage.

Insertion of a buffer layer between electrode and semiconducting layers is a widely employed strategy to control interfacial properties and ultimately improve device characteristics. Perovskite NC films on conventional PEDOT:PSS hole injection layers (HILs) often led to an inhomogeneous surface morphology. Pinholes and aggregated nanoplatelets reduced LED device efficiency. Also, exciton quenching at the PEDOT:PSS/perovskite film interface needed to be addressed, and interface engineering provided an attractive approach. Kim et al. used a multifunctional HIL to minimize exciton quenching at the perovskite/HIL interface.[128] With the above strategies, a high PLQY (∼60%) in compact perovskite particle films was achieved without further post-treatment, and LEDs based on colloidal perovskite NCs reached a high current efficiency of 15.5 cd/A.

Other attempts at transport layers include the use of inorganic NiOx as a HIL. Chih et al. reported that a NiO_x electrode interlayer enhances emission from a $MAPbBr_3$ film active layer, this finding attributed to suitable hole level alignment and improved electron blocking, together, that increased the probability of radiative recombination in the active layer.[140] Conjugated polyelectrolytes have been employed as the hole injection layer by Friend and co-workers.[134] PCPDT-K (poly[2,6-(4,4-bis-potassium butanylsulfonate)-4*H*-cyclopenta-[2,1-*b*;3,4-*b*′]-dithiophene)]) polyelectrolytes transfer holes efficiently, block electrons, and reduce luminescence quenching at the perovskite/PCPDT-K interface. Perovskite LEDs with PCPDT-K demonstrated a factor of approximately 4 increase in EQE compared to control devices that used PEDOT:PSS, reaching EQE of 5.7%, and with improved device stability.

4.2.2. Comparison of Perovskite LED with QLED and OLEDs. We turn now to a discussion of traditional II−VI quantum dots (QDs) and organic materials compared to perovskites in light-emitting applications (Table 2). QDs' tunable bandgap, as governed by the quantum size effect, also poses challenges, for it mandates a high monodispersity in the population of QDs.

A precisely tailored spectrum can be used to generate a specific color temperature of white light. The quality of white light is measured via the correlated color temperature (CCT) and color rendering index (CRI). For lower-CCT illumination at high temperature, high luminous efficiency and color quality are hard to achieve: the red luminophores require a very narrow emission line width. Conventional red phosphors have emission spectra that are very broad (>60 nm fwhm). The narrow spectral emission (∼30 nm fwhm) of QDs offer more selective optical down-conversion of a portion of a backlight's blue emission into red-shifted light, leading to a CRI of >90% and a superior CCT of 2700 K while maintaining a high luminance efficiency.[173] This allows QDs to increase color quality while lowering power consumption in solid state light sources. QDs can also be utilized as backlights in high-color-quality liquid-crystal displays.

QDs do come with challenges. The importance of monodispersity in QDs for electronics arises because a rough energy landscape impedes transport and enhances recombination due to the presence of small-bandgap inclusions. Charging can occur when under current injection, and this charging retards further injection, reducing EL efficiency. The time scales associated with QD charging range from minutes to days.[183] While the PLQY of QDs solution routinely often exceeds 95%, QDs deposited in a close-packed thin film exhibit lower (often by 1 order of magnitude) luminescence efficiency. Embedding QDs into an insulating polymer matrix decreases QD emission quenching;[184,185] however, the electrical conductivity in these QD-polymer composites is impeded by the low conductance of the wide bandgap polymers. Förster resonant energy transfer (FRET) between closed-packed QDs can also reduce the PLQY of QD films.[186]

DOI: 10.1021/acs.chemrev.9b00107
Chem. Rev. 2019, 119, 7444−7477

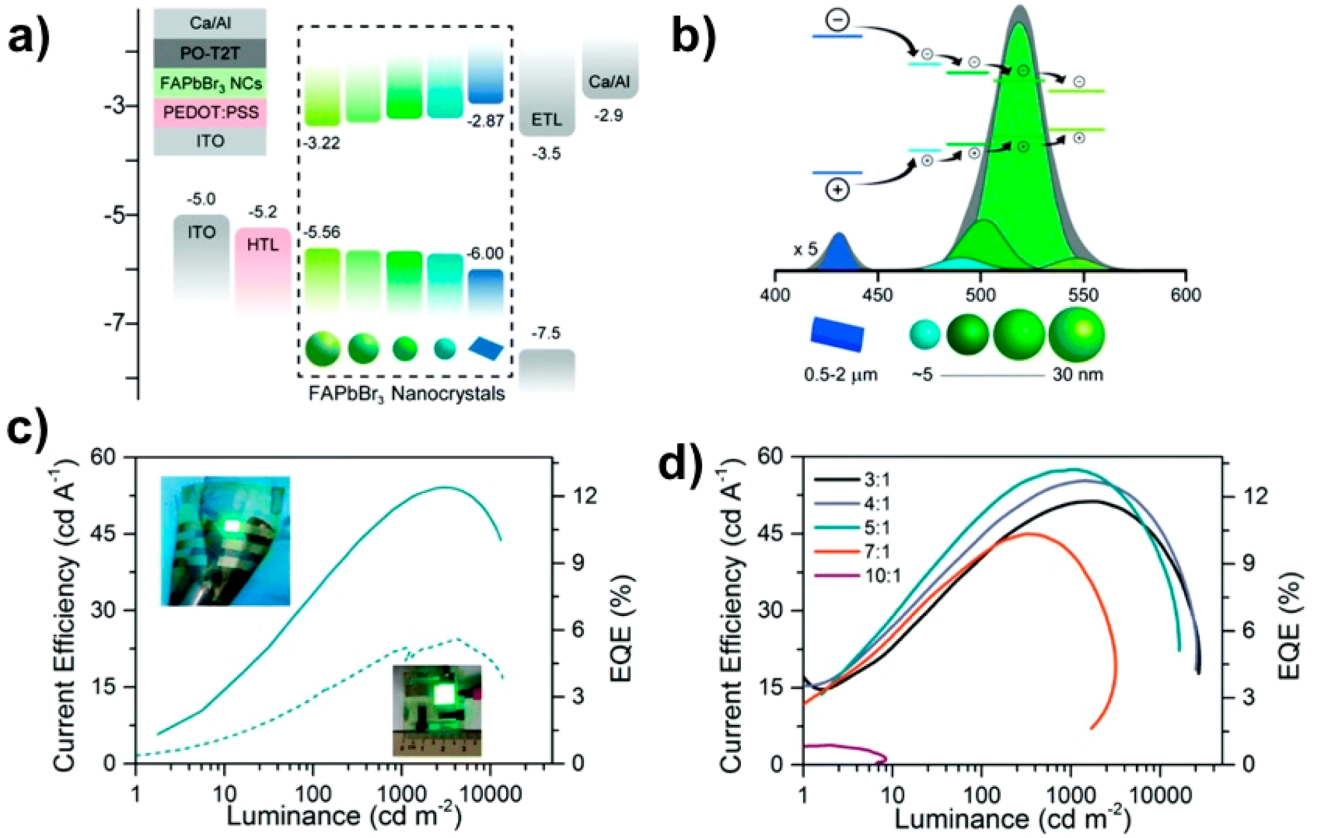

Figure 20. (a) Band diagram of perovskite NC LEDs with energy cascade materials. (b) The energy cascade from 2D microplatelets to $FAPbBr_3$ NCs of graded size, where the deconvolution of the steady-state PL spectrum clearly displays the different PL contribution at varying NC sizes. (c) Current efficiency/EQE versus luminance of flexible (3 mm^2) and large area (95.2 mm^2) LED devices. (d) Characteristic current efficiency/EQE versus luminance.[129] Reprinted with permission from ref 132. Copyright 2018 Royal Society of Chemistry.

While QDs are beginning to be deployed in applications such backlights in displays, organic LEDs (OLEDs) are already a multibillion dollar industry, with applications in displays, lighting, and consumer devices.[187] Most applications of OLEDs could benefit from a solution-processed approach (instead of the prevailing vacuum sublimation process), where roll-to-roll solution-processing and inkjet printing could potentially be employed.[188−191] To achieve this, new high-performance active materials that are solution-processable would accelerate adoption. Efficiency roll-off represents another remaining area for improvement in OLEDs. This corresponds to both a lowered power conversion efficiency as well as added electrical stress to achieve a given brightness, which works against device lifetime.

Perovskites offer pathways to color-saturated emission in view of their narrow emission line widths (<30 nm) and manifest the possibility for future high-color-purity emitters. Ready wavelength tuning, and efficient charge injection/transport property with perovskites, have been studied as promising features to enable next-generation light emitters. Perovskite LEDs also have shown sub-bandgap turn-on voltages, implying the possibility of achieving low operating voltages and high power conversion efficiencies in display applications. Perovskite LEDs, because they can be processed from the solution phase, can potentially be inkjet printed. Processing temperatures will likely be quite low (less than 150 °C), making fabrication compatible with flexible and light-weight plastic substrates.

4.3. Stability of Perovskite LEDs

The device stability in QD LEDs exhibit on the order of 100−1000 h when operated at relatively modest brightness (1000 cd m^{-2}).[175] In contrast, the device stability of state-of-art OLEDs is in the range of 10000 to 100000 h. Instability in early generation OLED was triggered by dark-spot effects; however, device encapsulation and optimization enabled the community to overcome these issues.[192] The stability of lead halide based perovskite LEDs remains a major issue in this early stage materials platform.[193] Here we will discuss this challenge including recent studies toward increased device stability.

4.3.1. Status and Mechanisms Underpinning Stability in Perovskite LEDs. Perovskite solar cells' device lifetimes now exceeds 1000 h under continuous operation while biased at the maximum power point.[194] Perovskite LEDs are at a less mature stage from the point of view of reliability: often devices have ∼subhour consistent operation under continuous electrical stress before degradation becomes observable at a brightness level higher than 100 cd m^{-2}.

Some issues in perovskite LEDs are likely shared with perovskite solar cells. From PV, it became clear that some compositions of thin films lack chemical and structural stability, especially in the presence of moisture or heat. The strong ionic character of perovskites is linked to phase segregation and ion migration as well as to various electro-chemical reactions[195−198] (Figure 22).

In early 2014, stability issues in perovskites for PV gained the attention of a number of research groups. Fundamental studies on instability in perovskite thin films in the presence of

DOI: 10.1021/acs.chemrev.9b00107
Chem. Rev. 2019, 119, 7444−7477

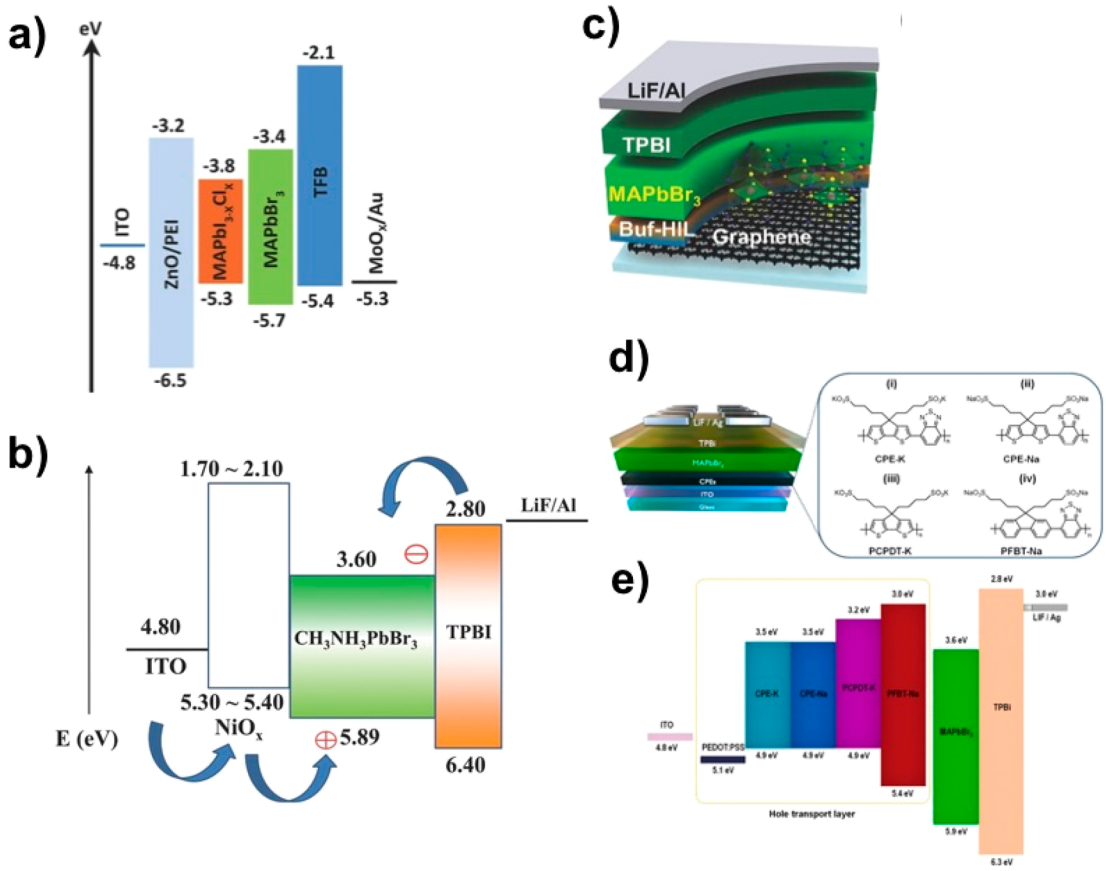

Figure 21. (a) Flat-band energy level diagram of perovskite LEDs using modified ZnO using PEI.[131] Reprinted with permission from ref 134. Copyright 2015 Wiley-VCH. (b) Energy diagram of perovskite devices using NiO_x as a HIL.[132] Reprinted with permission from ref 135. Copyright 2016 Wiley-VCH. (c) Device structure of perovskite LED with graphene electrode and $MAPbBr_3$ emitter.[133] Reprinted with permission from ref 136. Copyright 2017 Wiley-VCH. (d) Schematic illustrations of perovskite LED devices with various conjugate polymers as HIL and (e) related energy diagrams.[134] Reproduced from ref 137. Copyright 2018 American Chemical Society.

Table 2. Comparison of Perovskite LED, QD LED, and OLEDs

	PeLEDs	QD LEDs	OLEDs
fwhm (nm)	~20	~28	>70
$ELQY^{red}$ (%)	13[174]	20.5[175]	29[176]
L_{max}^{red} (cd/m^2)	82 Wsr^{-1} m^{-2}[43]	42000[175]	1000000[176]
$ELQY^{green}$ (%)	14[157]	14.5[177]	73100[178]
L_{max}^{green} (cd/m^2)	9120[157]	10000[177]	27.5[178]
$ELQY^{blue}$ (%)	1.5[179]	10.7[177]	36.7[180]
L_{max}^{blue} (cd/m^2)	2480[179]	4000[177]	10000[180]
operational stability (h)	10[181]	100000[175]	600000[182]
color tunability	400 nm−near IR	400 nm−near IR	400−700 nm

moisture and the surrounding environment were reported by Niu et. al.[200] Device fabrication needs to be carried out under controlled atmospheric conditions and with a humidity of <1% as shown by Gratzel and co-workers.[201] The degradation process was proposed to follow this route:

$$MAPbI_3 \leftrightharpoons MAI + PbI_2 \quad (1)$$

$$MAI \leftrightharpoons MA + HI \quad (2)$$

$$4HI + O_2 \leftrightharpoons 2I_2 + 2H_2O \quad (3\text{-}1)$$

$$2HI \leftrightharpoons H_2 + I_2 \quad (3\text{-}2)$$

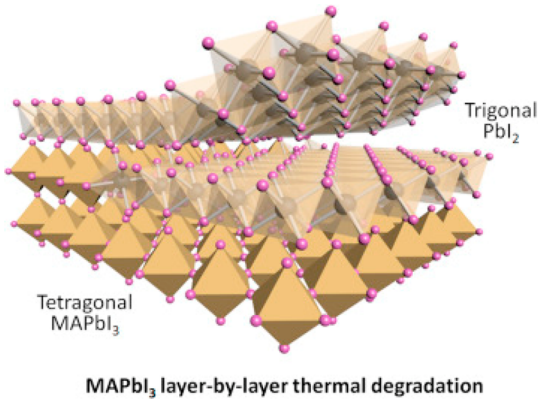

Figure 22. Structural degradation in $MAPbI_3$.[199] Reprinted with permission from ref 162. Copyright 2017, Wiley-VCH.

In reaction 1, $MAPbI_3$ decomposes into MAI and PbI_2 in the presence of H_2O (Figure 23). In this process, the equilibrium constant is $k(1) = c(MAI)$ and the Gibbs free energy is $\Delta G(1) = -RT \ln k(1)$. In reaction 2, MAI solution decomposes into MA solution and HI solution. Then the equilibrium constant is $k(2) = c(MA) \times c(HI)/c(MAI)$ and Gibbs free energy is $\Delta G(2) = -RT \ln k(1)$. In reaction 3, there are two ways for HI to react. Reaction 3-1 represents the redox reaction and can move forward readily. Reaction 3-2 represents the photochemical reaction, experimental evidence revealed that HI can

DOI: 10.1021/acs.chemrev.9b00107
Chem. Rev. 2019, 119, 7444−7477

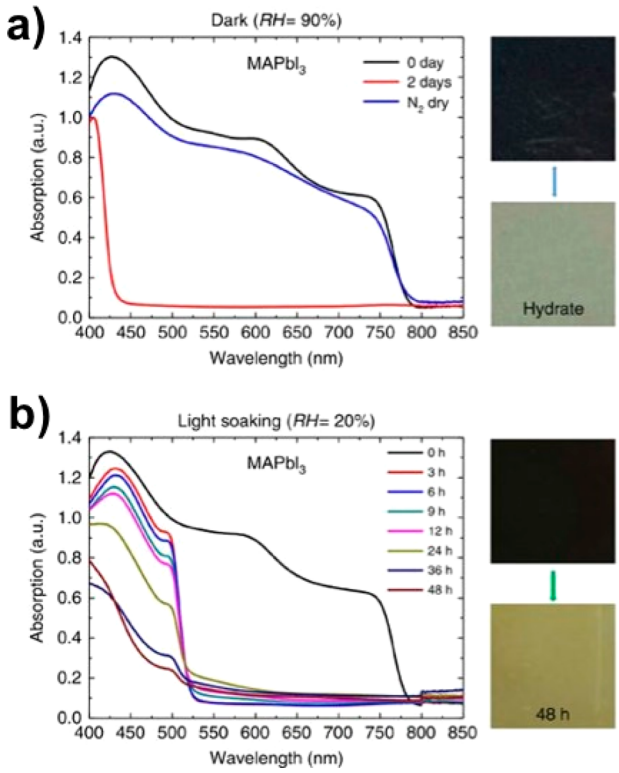

Figure 23. Hydration and light-induced degradation of perovskite materials. (a) Absorption spectra and pictures of the $MAPbI_3$ perovskite film. (b) Time evolution of absorption spectra and pictures of $MAPbI_3$ (h) before and (i) after degradation under light soaking at 20% RH.[204] Reprinted with permission from ref 167. Copyright 2016, Nature Publishing Group.

easily decompose into H_2 and I_2 under optical excitation. Ab initio molecular dynamics simulations further predicted surface reconstruction and light-assisted formation of hydrated species of $MAPbI_3{\cdot}H_2O$, a finding that agrees with the observation that exposure to water and light accelerates the degradation of perovskites.[202,203]

Charge trapping at the interface between perovskites and charge extraction materials are responsible for irreversible degradation due to moisture.[204] To understand charge-driven degradation mechanisms, it was important to develop controlled stability experiments both for commonly used $MAPbI_3$, which is known to form structurally distorted tetragonal crystals, and also for mixed perovskite materials having more enhanced structural stability. It was found that the mixed perovskite $MA_{0.6}FA_{0.4}PbI_{2.9}Br_{0.1}$ still degraded, although its degradation speed was slower than that of conventional $MAPbI_3$. It was further shown that the irreversible degradation of the perovskites was triggered by trapped charges.

Oxygen, in addition to moisture, can also trigger degradation.[205] Darkening in PL also involved interaction with photogenerated carriers. The dynamics of PL in $MAPbI_3$ films were studied under continuous photoexcitation. The activation and darkening of the PL intensity was observed, and this was found to depend strongly on optical pump characteristics. When the optical photoexcitation intensity was increased, the perovskites PL increased linearly, and both activation and darkening dynamics increased.

Photoactivation fills subgap trap states that otherwise limit the PL of the perovskite.[206] These states can be either shallow or deep, and photoactivation is more efficient in the presence of O_2 than it is with N_2. When and if the photoactivation process is in fact relevant to the filling of charge traps, oxygen plays a role in the process. Perovskite films under prolonged

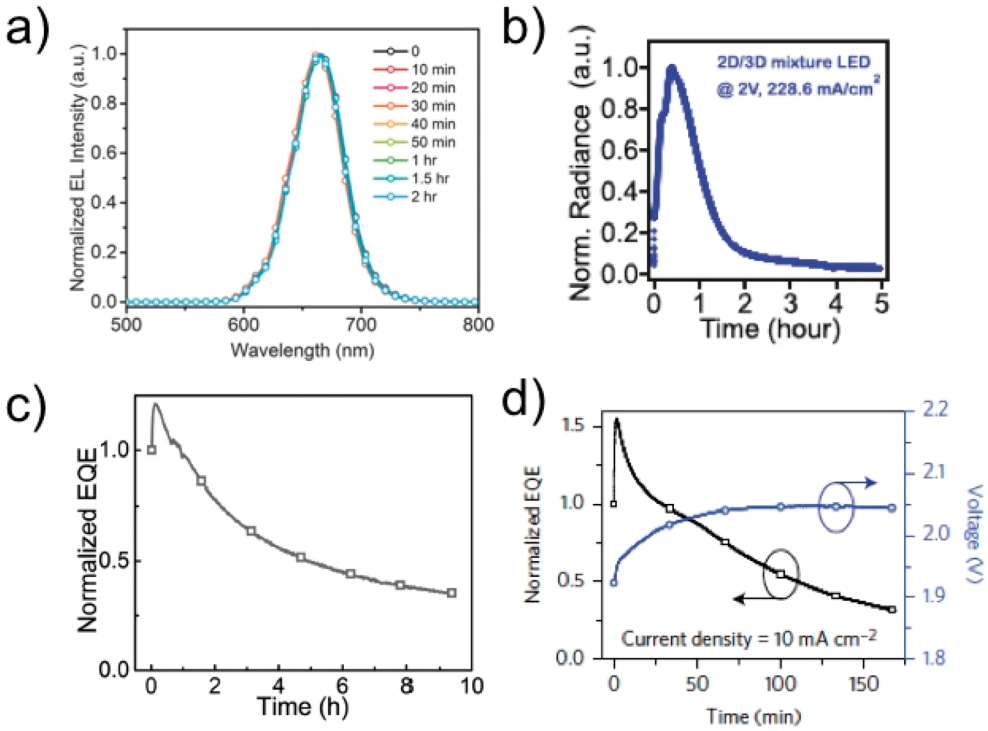

Figure 24. (a) Perovskite LED spectral stability[220] and (b−d) device operational stability under constant bias.[43,117,221] Reprinted with permission from ref 185. Copyright 2018 Wiley-VCH. Reprinted with permission from ref 43. Copyright 2018 Wiley-VCH. Reprinted with permission from ref 120. Copyright 2016 Nature Publishing Group. Reprinted with permission from ref 186. Copyright 2017 Wiley-VCH.

DOI: 10.1021/acs.chemrev.9b00107
Chem. Rev. 2019, 119, 7444−7477

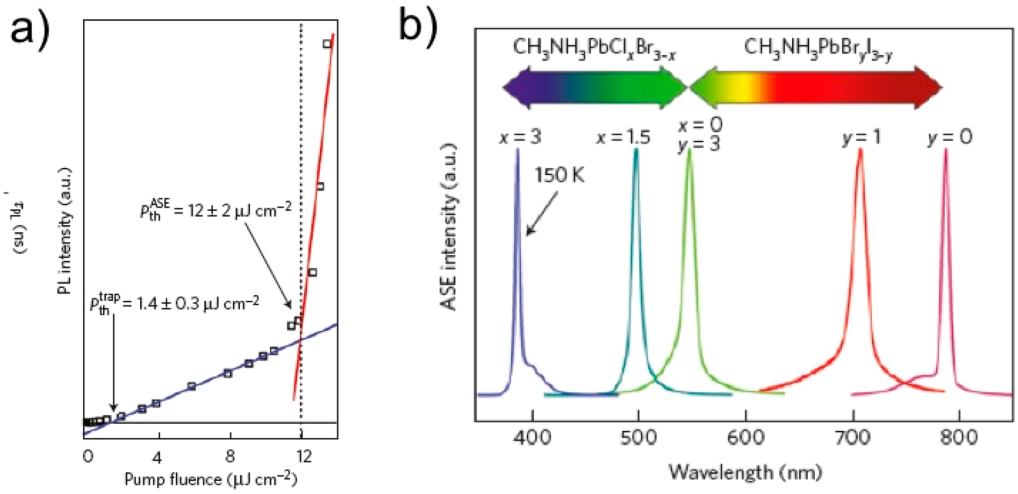

Figure 25. (a) PL intensity of $MAPbI_3$ film as increase the pump fluence. (b) ASE wavelength tunability across a wide visible wavelength range for the case of halide perovskite thin films.[224] Reprinted with permission from ref 189. Copyright 2014 Nature Publishing Group.

optical excitation may photodarken, a fact attributed to the decomposition of the perovskites under excitation. The hydrated compounds are easily formed upon photoexcitation, and this leads to a weakening of hydrogen bonds between PbI_6 and organic cations. This ultimately promotes the formation of complexes between H_2O and PbI_6.[207,208] Further research is required to understand the mechanisms of H_2O and O_2 in the photoactivated processes.

The mechanistic process of degradation has been studied using super-resolution luminescence microspectroscopy.[209] The degradation of the $MAPbI_3$ crystal structure starts locally due to the collapse to the layered PbI_2 structure; and then spreads across the crystal. The migration of MA ions can distort the perovskite lattice, and this leads to the loss of the crystal structure.

In addition to instabilities in perovskite materials, device instabilities can also come from interfacial layers and electrical stress during operation of device. Ionic processes, such as halide segregation, can destroy perovskites and generate defects,[210] some of which are voltage-induced and others spontaneous. Some examples include the corrosion/oxidation of electrodes,[211−214] degradation of charge-transport layers,[215] and the formation of charge-accumulated interfaces[204] and *p*−*i*−*n* junctions.[150,216−218] Furthermore, the diffusion of metallic species from electrodes, the origin of which is still unclear, can cause a significant decrease in device efficiency and accelerate the degradation of perovskite LEDs.

4.3.2. Strategies to Improve LED Stability. To improve perovskite LED stability, several approaches have been used. Inorganic $CsPbX_3$ based perovskites have been shown to improve LED stability compared with MA-based perovskites,[143] a finding associated with their enhanced thermal, structural, and chemical stability. The high thermal stability of $CsPbBr_3$ may improve the operational stability of perovskite LEDs by suppressing degradation caused by thermal stresses, including Joule heating. Schaller and co-workers reported temperature-dependent PL below 450 K, which strongly affected by halide composition.[219]

Another strategy to improve perovskite stability involves the use of layered perovskite structures. Perovskites of composition $(PEA)_2(MA)_2[Pb_3I_{10}]$ have shown increased stability against moisture, attributed in part to the hydrophobic nature of the PEA layers. Using a density functional theory (DFT) approach, Quan et al. proposed that the introduction of PEA layers can increase quantitatively van der Waals interactions. These provide an increased formation energy corresponding to improved materials stability.[26]

Recently, quasi-2D perovskite/poly(ethylene oxide) (PEO) composite thin films were reported as the light-emitting layer in work by Ma and co-workers[220] (Figure 24). Controlling the molar ratios of organic (benzylammonium iodide) to inorganic salts (CsI and PbI_2), the group obtained luminescent quasi-2D perovskite thin films exhibiting tunable emission colors from red to NIR. LEDs with an emission peaking at 680 nm exhibited a brightness of 1392 cd m^{-2} and an EQE of 6.2%. The EL intensity dropped by 20% relative following 4 h of continuous operation, and these devices exhibited enhanced spectral stability.

Kim et al., reported the charge carrier recombination and ion migration induced by photoexcitation by analyzing steady-state and transient PL and photoresponsivity in perovskite films.[222] These results indicate organic ligands in perovskite films efficiently prevent ion migration and ion-migration-induced defects. These efficient confinement of electron−hole pairs and prevention of ion migration in perovskite films induced high photostability, PLQY of the perovskite films.

5. PEROVSKITES FOR LASING

5.1. Optical Amplification Using Perovskites

Stimulated emission is the coherent photon emission process wherein an incident photon is amplified (gain) via downward radiative transitions from excited state levels. By studying charge transfer process in perovskite solar cells, researchers first observed stimulated emission in $MAPbX_3$ with the aid of ultrafast pump−probe spectroscopy.[2]

Optical amplification, measured via gain per unit length (in cm^{-1}), can be studied by measuring the absorption spectra from the photoexcited gain medium. In perovskite thin films, optical gains have been reported[223] in the range 3200 ± 800 cm^{-1}. This value is comparable to that of single-crystal GaAs and agrees with the known high absorption coefficient of perovskite. Gain has been shown to be as long as 200 ps, with a threshold of ∼16 μJ cm^{-2}. When one varies the pump fluence, the emitted spectral intensity yields a threshold for amplified

DOI: 10.1021/acs.chemrev.9b00107
Chem. Rev. 2019, 119, 7444−7477

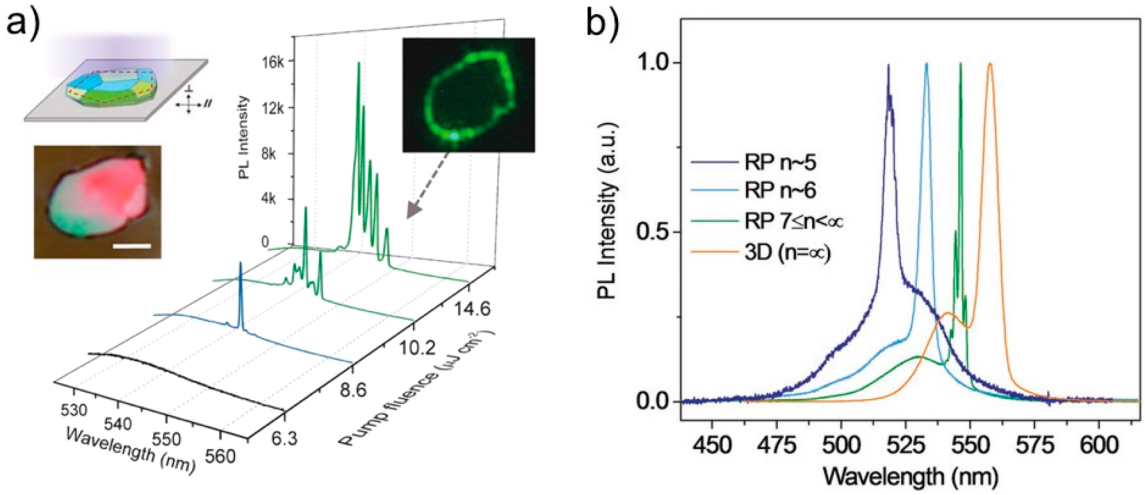

Figure 26. (a) Lasing from a single low-dimensional perovskite microplate. Pump-fluence-dependent PL spectra of a single microplate. Left inset: Optical image, scale bar 5 μm, and schematic illustration of lasing measurements of microplate on a substrate pumped by a 400 nm laser excitation (≈150 fs, 1 kHz). (b) Normalized lasing spectra from 3D perovskite film to quasi-2D perovskite microplates.[240] Reprinted with permission from ref 195. Copyright 2018 Wiley-VCH.

spontaneous emission (ASE). The luminescence becomes narrows and sharply increases above the ASE threshold. Reported ASE thresholds for halide perovskites are ranging from 12 μJ cm^{-2} under femtosecond excitation[224] to 60 μJ cm^{-2} under nanosecond photoexcitation conditions[225] and 7.6 μJ cm^{-2} at pulse durations as long as 5 ns with a liquid crystal reflector.[226]

5.1.1. Original Reports of Perovskite Lasing. Solution-processed $MAPbX_3$ perovskite films were studied with an eye to lasing by Xing et. al[224] (Figure 25). An increased pump fluence lead to the transition from spontaneous emission (SE) to ASE in $MAPbI_3$ thin film. Using the threshold fluence (12 ± 2 μJ cm^{-2}) and absorption coefficient (α = 5.7 × 10^4 cm^{-1} at 600 nm), the ASE threshold was calculated to be ∼1.7 × 10^{18} cm^{-3}. The Auger recombination process in perovskites, dominant at high pump fluence, leads to lifetimes in the range of a few ps to ns, depending on the photogenerated charge carrier density. The low ASE threshold in perovskites is attributed in significant part to the low trap density in the best such films.

The PLQY as a function of excitation fluence in $CH_3NH_3PbI_{3-x}Cl_x$ perovskite films was, as previously discussed, an impressive 70% at high excitation density. Friend and co-workers constructed and demonstrated the operation of vertical cavity lasers that employed a perovskite layer sandwiched between a dielectric mirror and a metal mirror.[108]

The relation between the phase-transition of the perovskite film, and ASE mechanisms, was investigated by studying behavior in different phase states.[227] A sharp ASE peak with the maximum spectral intensity occurs at the temperature of 120 K. PL emission spectra show a notable variation of the spectral characteristics when moving from temperatures 120 to 160 K, in which range the structural phase transformation from orthorhombic to tetragonal occurs. As the temperature exceeds 120 K, the lasing threshold continues to increase because of thermal broadening of the gain peak. Low-threshold ASE and lasing has also been reported from colloidal $CsPbX_3$ NCs having a 10 nm size.[228] Optical amplification in perovskite NCs was obtained with low pump thresholds (5 ± 1 mJ cm^2) and across the visible spectral range (440−700 nm). Conformally coated perovskite NCs on a high-finesse resonator, such as silica microspheres, have enabled the observation of whispering-gallery-mode lasing.

5.1.2. Effects of Perovskite Crystal Structures

$MAPbI_3$ exhibits a reversible phase transition between its tetragonal and cubic phases at ∼330 K and is sensitive to oxygen, moisture, and heat. As a result, all-inorganic $CsPbX_3$ has also been explored as an optical gain medium due to their narrow gain profiles and wavelength tunability.[228−231]

A film consisting of close-packed $CsPbBr_3$ NCs was photoexcited using a wavelength 400 nm in a stripe configuration. A narrower emission band located at 524 nm with fwhm of ≈5 nm appears on the longer wavelength side when the pump intensity exceeds ≈22 μJ cm^{-2}. These optical gain properties in $CsPbBr_3$ NCs suggest a material of interest in lasing, especially in the green and blue spectral range, where II−VI group quantum dots show lower gain performance than their red counterparts.[232] Nonradiative Auger recombination occurring at high excitation intensities has been recognized to be the main channel dissipating population inversion in quantum dots, hindering optical amplification. Excitation-intensity-dependent time-resolved PL measurements were performed on $CsPbBr_3$ NCs to explore Auger recombination.[229] The PL decay of the $CsPbBr_3$ is relatively slow single-exciton recombination under low excitation intensities (<4.5 μJ cm $^{-2}$), then a fast decay process emerges as the excitation intensity increases, corresponding to the Auger recombination, on the ∼100 ps time scale.

ASE in the optically pumped $FAPbI_3$ and MABr-stabilized $FAPbI_3$ films showed an impressively low threshold of 1.6 μJ/cm^2. $FAPbI_3$ films displayed more durable lasing emission than $MAPbI_3$.[233] The lasing threshold improved in $FAPbI_3$ films due to their low defect density and high thermal stability. High-quality low-dimensional single crystals with lower defect densities and reduced scattering will support further lowering threshold.

The solution growth of high-quality single-crystal phase $FAPbI_3$ nanowires led to black-phase $FAPbI_3$ alloy nanowires in the cubic perovskite phase. These were made by incorporating a small amount of MABr into $FAPbI_3$.[234] Optically pumped lasing was reported from MABr-stabilized

DOI: 10.1021/acs.chemrev.9b00107
Chem. Rev. 2019, 119, 7444−7477

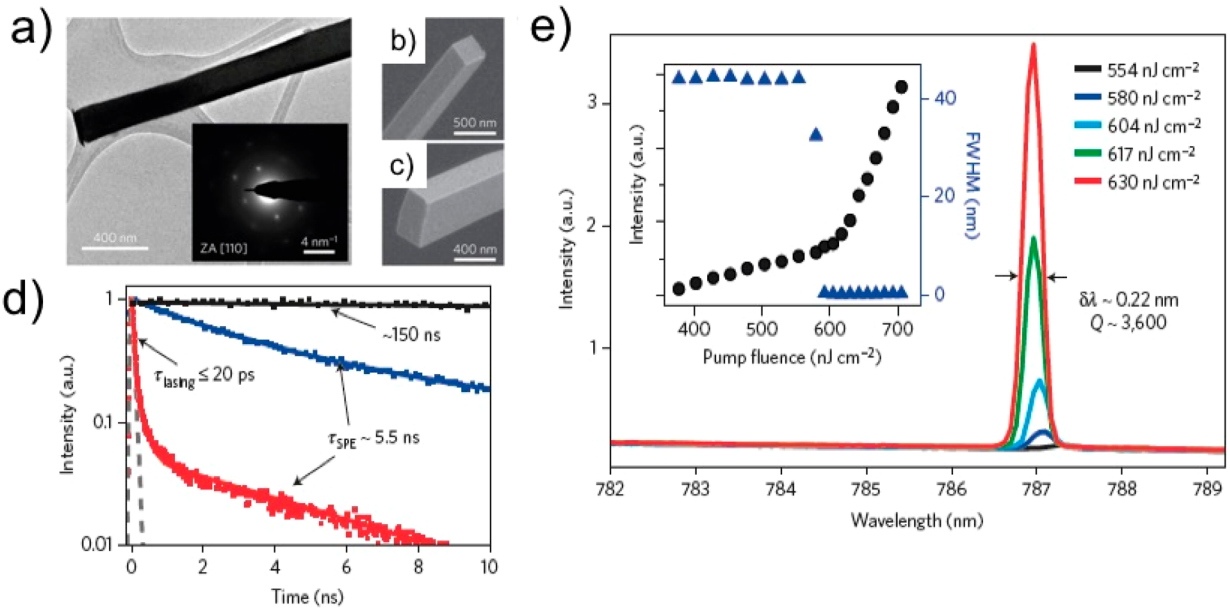

Figure 27. (a) TEM images and selected-area electron diffraction patterns along the [110] zone axis (ZA). (b,c) SEM images of perovskite nanowires. (d) Transient decay kinetics of perovskite nanowires with different excitation fluence ($P \sim 0.85P_{Th}$, blue; $P \sim 1.1P_{Th}$, red). (e) Emission spectra of perovskite nanowires near the lasing threshold.[241] Reprinted with permission from ref 206. Copyright 2015 Nature Publishing Group.

$FAPbI_3$ perovskites at room temperature with near-infrared (NIR) emission at ~800 nm, low lasing thresholds of a few $\mu J/cm^2$, and high quality factors of ~1500. These FA-based perovskite NWs displayed improved photostability and wavelength tunability compared to MA-based perovskite NWs.[234]

Solution-processed lead-free Sn-based halide perovskites such as $CsSnX_3$ exhibit relatively poor photovoltaic performance;[235−238] however, they possess remarkable optical gain properties in the NIR up to ≈1 μm. Ultralow-threshold (≈6 $\mu J\ cm^{-2}$), large-gain (200 cm^{-1}) stimulated emission was seen in 20% SnF_2-$CsSnI_3$ samples, providing performance comparable to Pb counterparts. Transient absorption spectroscopy on $CsSnI_3$ perovskite revealed that SnF_2 addition suppressed trap state and that lasing originated from bimolecular recombination of free electron−holes with a high rate of ≈ $10^{-8}\ cm^{-3}s^{-1}$ (i.e., 1−2 orders larger than $MAPbI_3$). Stable (>20 h), room-temperature NIR coherent light emission (700−1000 nm) was achieved as a reult. The ASE wavelength was tuned from 700 to 950 nm by varying bromide:iodide composition to obtain $CsSnBr_3$, $CsSnBr_2I$, $CsSnBrI_2$, and $CsSnI_3$ thin films.

Although multiquantum well structures of layered perovskites exhibit strong light−matter interactions, room temperature optical gain in layered perovskites have not been seen so far, likely a consequence of efficient nonradiative trapping of free excitons and/or biexcitons.[239]

Recently, $(OA)_2(MA)_{n-1}Pb_nBr_{3n+1}$ based mixed lower-dimensional perovskite layers (with larger bandgaps and smaller refractive index acting as cladding layers) provided enhanced exciton and photon confinement for higher-dimensional perovskite layers (the active layers)[240] (Figure 26). The achievement of low-threshold (~7.8 $\mu J\ cm^{-2}$) lasing from near-3D to quasi-2D perovskites is related to efficient exciton localization from lower-dimensional perovskite layers to the active layers in microplatelets.

5.2. Laser Cavity Structures in Perovskite Lasers

In semiconducting nanowires, waveguiding is provided along the axial direction, and the two end facets form a Fabry−Perot cavity. The growth of high-quality single-crystal nanowires from low-temperature solution-processing of $MAPbX_3$ perovskites was reported by Zhu and co-workers.[241] The perovskite nanowires exhibited low lasing thresholds (200 nJ/cm^{-2}), high quality factors ($Q \sim 3600$), near-unity quantum yield, and wavelength tunability from the NIR to the visible wavelengths (Figure 27).

Perovskite nanoplatelets were grown on mica substrates and formed whispering gallery mode (WGM) cavities as a result of the growth procedure.[242] Individual perovskite nanoplatelets were photoexcited using a femtosecond-pulsed laser, and a lasing threshold of 37 $\mu J\ cm^{-2}$ was achieved in $MAPbI_3$ nanoplatelets. Solution growth of $MAPbBr_3$ perovskite microdisks (also a means to WGM microresonators) exhibited a quality factor of ≈430.[243] Single-mode lasing at 558 nm was achieved in a $2 \times 2 \times 0.6\ \mu m^3$ square microdisk and exhibited a threshold of 3.6 ± 0.5 $\mu J\ cm^{-2}$. WGM lasers from planar perovskite nanoplatelets exhibit tunable optical modes and impressive optical gain and offer a pathway to integration with Si technologies.

In distributed feedback (DFB) cavity structures, optical feedback is provided via Bragg scattering from an interference grating built either directly into the active medium or in the vicinity of the resonator through periodic alternation of the refractive index. Jia et. al, reported a metal-clad, second-order DFB perovskite laser with a threshold of 5 kW/cm^2 for durations ≤25 ns. The work demonstrated that the substrate can be used to dissipate heat and offered thus a step in the direction of future electrically driven architectures.[244] Saliba et al., reported perovskite DFB cavities made by nanoimprinting a corrugated structure onto a polymer template, after which they then introduced a conformal perovskite layer.[245] Significant narrowing of the line width of the ASE peak was observed with increased excitation fluence, and the wavelength red-shifted as

DOI: 10.1021/acs.chemrev.9b00107
Chem. Rev. 2019, 119, 7444−7477

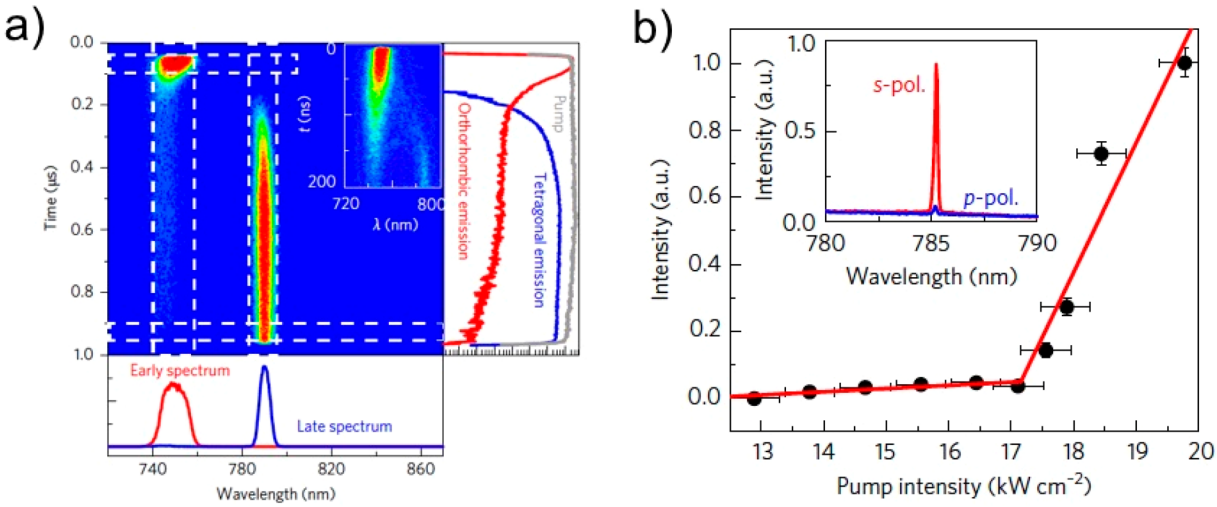

Figure 28. (a) Streak camera image of emission from the $MAPbI_3$ film under the pump intensity 37.5 kW/cm^{-2} with InGaN diode laser with instantaneous intensity. The substrate temperature is lowered to T = 106 K. In this case, ASE from the orthorhombic phase of $MAPbI_3$ is observed at early times but evolves within ~200 ns. (b) Input−output characteristic of the laser under continuous excitation by a λ = 445 nm InGaN pump diode at a substrate temperature of 102 K, demonstrating a clear threshold at IP ≈ 17 kW/cm.[247] Reprinted with permission from ref 212. Copyright 2017 Nature Publishing Group.

the grating periodicity of the DFB cavity increased. The fluence threshold diminished from 2.1 to 0.3 μJ cm^{-2} as the grating period decreased from 420 to 400 nm.

A new hybrid perovskite vertical cavity surface-emitting laser (VCSEL) was microfabricated based on a uniform perovskite thin (≈300 nm) film placed between two high-reflectivity (≈99.5%) distributed Bragg reflectors (DBRs).[246] This work leveraged gallium nitride semiconductor process innovations wherein a nanoporous-GaN (NP-GaN) provides the low-index layers in a NP-GaN/GaN (electrically conducting) multilayer stack. The perovskite VCSEL device enabled the study of gain dynamics on excitation time scales that are much longer than typically reported in femtosecond experiments in the perovskite literature. VCSEL lasing output as a function of pumping fluence indicated a lasing threshold of 7.6 μJ cm^{-2}.

Continuous-wave (CW) operation of a perovskite methylammonium lead iodide ($MAPbI_3$)[247] laser was recently reported (Figure 28). Under constant blue optical photoexcitation, devices emitted near-infrared (785 nm wavelength) laser light over the course of an hour when operated at 100 K. To achieve CW lasing, the authors sought a strategy to generate exciton/charge-trapping sites in the material. They took advantage of the phase transition in $MAPbI_3$: when the temperature is decreased to 160 K, the crystal structure of $MAPbI_3$ changes from tetragonal phase to the orthorhombic phase. A distributed feedback laser fabricated with $MAPbI_3$ was operated at 100 K, hence in orthorhombic phase. With a high excitation power (>17 kW cm^{-2}), the tetragonal phase can transform to the orthorhombic lattice within a few 100 ns, due to local heating, and this provides a local heterostructure inside the perovskite film.

6. CONCLUSIONS AND OUTLOOK

The efficiencies of perovskite solar cells have advanced from 3.8 to a certified 24.2% in less than a decade of concerted worldwide effort. The materials rely upon facile low-temperature processing. Their structural flexibility and excellent optoelectronic properties have yielded efficient LEDs as well as lasers.

In optical sources, one central theme in perovskite light emission has been the move from the bulk (3D) materials widely used in solar cells toward instead the application of reduced-dimensional structures. Taken together with judicious compositional engineering, this has advanced perovskites across a wide range of emission wavelengths to near-unity PLQY. The same defect-tolerance that serves these materials so well in photovoltaics is a major factor enabling their bright PL. It will be important to improve further the photostability of reduced-dimensional perovskites. The passivation of grain boundaries is a particularly important priority.

Among these reduced-dimensional perovskite emitters, colloidally synthesized nanometer-scale NCs have shown excellent quantum yield and combine with other classes of solution-processed materials, such as polymers and small molecules, to enhance optical and electronic functionalities. It will be essential to apply high-PLQY NCs in displays and generating new Pb-free materials options that exhibit excellent emission properties is a high priority as a result. Possibilities based upon Sn, Ge, Cu, Bi, and Sb have been explored, but lead-free perovskites today perform well below Pb-based device levels. Accelerated computational-experimental approaches could potentially contribute to addressing this important challenge.

Given the soft nature of the hybrid perovskite materials, their stability against moisture, heat, oxygen, and electric field will continue to be an area of intense activity. Here the versatile chemistry of hybrid organic−inorganic perovskites will be leveraged on the path to further progress. Recent advances on this front are encouraging, including operating stability of 1000 h under 1 sun illumination. Integrated encapsulation strategies have increased stability against external humidity and heat. Compared with solar cells, though, LEDs still rely on charge injection rather than extraction; and also see higher fields in light of the >3 V often used to drive devices. It will therefore be of urgent importance to enhance further the operational stability of perovskite LEDs.

Progress in perovskite LEDs has been uneven as a function of emission wavelength: the EQE in the green rapidly exceeded

DOI: 10.1021/acs.chemrev.9b00107
Chem. Rev. 2019, 119, 7444−7477

20%[43,135,159,162] but in the blue emission resides in the 3% and below range.[179] Recent reports of blue luminescence quantum yields of 80%[248] are certainly encouraging, but such materials need to be married with enhanced carrier transport and suitable interlayer band alignment to translate into high device performance. Highly emissive, stable, and conductive blue emitting perovskite materials remain a frontier area of great applied importance and fundamental interest.

On lasing, room-temperature CW performance is a next frontier. Perovskite single crystals are promising candidates for CW lasing and their slower Auger recombination and lower thresholds offer encouragement on this path. Electrically driven lasing is a next challenge: population inversion is required from a high-quality gain medium exhibiting slow Auger recombination. Electrical excitation demands high charge carrier mobilities as well as improved thermal stability, a larger gain and sharp absorption band tails. Perovskites have shown encouraging properties on many of these fronts, except that thermal stability and carrier mobility will likely need further improvement.

ASSOCIATED CONTENT

Special Issue Paper

This paper is an additional review for *Chem. Rev.* **2019**, volume *119*, issue 5, "Perovskites".

AUTHOR INFORMATION

Corresponding Author

*Phone: (416)946-5051. E-mail: ted.sargent@utoronto.ca.

ORCID

Li Na Quan: 0000-0001-9301-3764
Barry P. Rand: 0000-0003-4409-8751
Richard H. Friend: 0000-0001-6565-6308
Subodh Gautam Mhaisalkar: 0000-0002-9895-2426
Tae-Woo Lee: 0000-0002-6449-6725
Edward H. Sargent: 0000-0003-0396-6495

Notes

The authors declare no competing financial interest.

Biographies

Li Na Quan received her Ph.D. from Ewha Womans University, Korea, in 2016 under the supervision of Prof. Dong Ha Kim. From 2014 to 2017, she worked at the University of Toronto with Prof. Edward. H. Sargent as a graduate student and postdoctoral researcher. Since 2018, she has worked with Prof. Peidong Yang at the University of California, Berkeley, as a postdoctoral fellow. Her research focuses on low-dimensional materials for light harvesting and optical source applications and photophysical studies.

Barry P. Rand earned a B.E. in electrical engineering from The Cooper Union in 2001. Then he received M.A. and Ph.D. degrees in electrical engineering from Princeton University, in 2003 and 2007, respectively. From 2007 to 2013, he was at IMEC in Leuven, Belgium, ultimately as a principal scientist. Since 2013, he is in the Department of Electrical Engineering and Andlinger Center for Energy and the Environment at Princeton University, currently as an Associate Professor. He has authored more than 115 peer-reviewed journal publications, has 20 issued U.S. patents, and has received the 3M Nontenured Faculty Award (2014), DuPont Young Professor Award (2015), DARPA Young Faculty Award (2015), and ONR Young Investigator Program Award (2016).

Richard H. Friend is the Cavendish Professor of Physics at the University of Cambridge. His research interests relate to the optoelectonic properties of organic materials.

Subodh G. Mhaisalkar is the Tan Chin Tuan Centennial Professor in the School of Materials Science & Engineering at the Nanyang Technological University (NTU), Singapore. He is also the Executive Director of the Energy Research Institute at NTU (ERI@N), a pan-University multidisciplinary research institute for innovative energy solutions. Prior to joining NTU in 2001, he had over 10 years of research and engineering experience in the microelectronics industry. He received his Bachelors' degree from IIT-Bombay, India, and his M.S./Ph.D. degrees from The Ohio State University, USA.

Tae-Woo Lee is an associate professor in the Department of Materials Science and Engineering at Seoul National University, Korea. He received his Ph.D in Chemical Engineering from KAIST, Korea, in 2002. He joined Bell Laboratories, USA, as a postdoctoral researcher in 2002 and worked at Samsung Advanced Institute of Technology as a member of research staff (2003−2008). He was an assistant and associate professor in the Department of Materials Science and Engineering at Pohang University of Science and Technology (POSTECH), Korea, until August 2016. His research focuses on organic, organic−inorganic hybrid perovskite, and carbon materials, and their applications to flexible electronics, printed electronics, displays, solid-state lightings, solar energy conversion devices, and bioinspired neuromorphic devices.

Edward H. Sargent is University Professor in Electrical and Computer Engineering at the University of Toronto. He holds the Canada Research Chair in Nanotechnology and also serves as Vice President—International for the University. He was founder and CTO of InVisage Technologies Inc. of Menlo Park.

ACKNOWLEDGMENTS

B.P.R. acknowledges support from the U.S. Office of Naval Research Young Investigator Program (grant award no. N00014-17-1-2005). R.H.F. acknowledge support from the Engineering and Physical Sciences Research Council (EPSRC). S.G.M. acknowledges support from the U.S. Office of Naval Research (ONRGNICOP-N62909-17-1-2155) and from the Singapore National Research (program NRF-CRP14-2014-03). T.-W.L. acknowledges support from the National Research Foundation of Korea (NRF) grant funded by the Korea government (Ministry of Science, ICT & Future Planning) (NRF-2016R1A3B1908431). E.H.S. acknowledges support from the U.S. Office of Naval Research (grant award no.: N00014-17-1-2524).

REFERENCES

(1) Kojima, A.; Teshima, K.; Shirai, Y.; Miyasaka, T. Organometal Halide Perovskites as Visible-Light Sensitizers for Photovoltaic Cells. *J. Am. Chem. Soc.* **2009**, *131*, 6050−6051.

(2) Kim, H. S.; Lee, C. R.; Im, J. H.; Lee, K. B.; Moehl, T.; Marchioro, A.; Moon, S. J.; Humphry-Baker, R.; Yum, J. H.; Moser, J. E.; Grätzel, M.; Park, N.-G. Lead Iodide Perovskite Sensitized All-Solid-State Submicron Thin Film Mesoscopic Solar Cell with Efficiency Exceeding 9%. *Sci. Rep.* **2012**, *2*, 591.

(3) Lee, M. M.; Teuscher, J.; Miyasaka, T.; Murakami, T. N.; Snaith, H. J. Efficient Hybrid Solar Cells Based on Meso-Superstructured Organometal Halide Perovskites. *Science* **2012**, *338*, 643−647.

(4) Abrusci, A.; Stranks, S. D.; Docampo, P.; Yip, H. L.; Jen, A. K.; Snaith, H. J. High-Performance Perovskite-Polymer Hybrid Solar Cells Via Electronic Coupling with Fullerene Monolayers. *Nano Lett.* **2013**, *13*, 3124−3128.

DOI: 10.1021/acs.chemrev.9b00107
Chem. Rev. 2019, 119, 7444−7477

(5) Burschka, J.; Pellet, N.; Moon, S. J.; Humphry-Baker, R.; Gao, P.; Nazeeruddin, M. K.; Gratzel, M. Sequential Deposition as a Route to High-Performance Perovskite-Sensitized Solar Cells. *Nature* **2013**, *499*, 316−319.
(6) Liu, M.; Johnston, M. B.; Snaith, H. J. Efficient Planar Heterojunction Perovskite Solar Cells by Vapour Deposition. *Nature* **2013**, *501*, 395−398.
(7) *Best Research Cell Efficiencies*; National Renewable Energy Laboratory, 2019; https://www.nrel.gov/pv/cell-efficiency.html (accessed April 3, 2019).
(8) Correa-Baena, J.-P.; Saliba, M.; Buonassisi, T.; Grätzel, M.; Abate, A.; Tress, W.; Hagfeldt, A. Promises and Challenges of Perovskite Solar Cells. *Science* **2017**, *358*, 739−744.
(9) Stranks, S. D.; Eperon, G. E.; Grancini, G.; Menelaou, C.; Alcocer, M. J. P.; Leijtens, T.; Herz, L. M.; Petrozza, A.; Snaith, H. J. Electron-Hole Diffusion Lengths Exceeding 1 Micrometer in an Organometal Trihalide Perovskite Absorber. *Science* **2013**, *342*, 341−344.
(10) Sutherland, B. R.; Sargent, E. H. Perovskite Photonic Sources. *Nat. Photonics* **2016**, *10*, 295−302.
(11) Era, M.; Morimoto, S.; Tsutsui, T.; Saito, S. Organic-Inorganic Heterostructure Electroluminescent Device Using a Layered Perovskite Semiconductor (C6h5c2h4nh3)2pbi4. *Appl. Phys. Lett.* **1994**, *65*, 676−678.
(12) Tan, Z. K.; Moghaddam, R. S.; Lai, M. L.; Docampo, P.; Higler, R.; Deschler, F.; Price, M.; Sadhanala, A.; Pazos, L. M.; Credgington, D.; et al. Bright Light-Emitting Diodes Based on Organometal Halide Perovskite. *Nat. Nanotechnol.* **2014**, *9*, 687−692.
(13) Cho, H.; Jeong, S. H.; Park, M. H.; Kim, Y. H.; Wolf, C.; Lee, C. L.; Heo, J. H.; Sadhanala, A.; Myoung, N.; Yoo, S.; et al. Overcoming the Electroluminescence Efficiency Limitations of Perovskite Light-Emitting Diodes. *Science* **2015**, *350*, 1222−1225.
(14) Saliba, M.; Matsui, T.; Domanski, K.; Seo, J.-Y.; Ummadisingu, A.; Zakeeruddin, S. M.; Correa-Baena, J.-P.; Tress, W. R.; Abate, A.; Hagfeldt, A.; Gratzel, M. Incorporation of Rubidium Cations into Perovskite Solar Cells Improves Photovoltaic Performance. *Science* **2016**, *354*, 206−209.
(15) Ptak, M.; Mączka, M.; Gągor, A.; Sieradzki, A.; Stroppa, A.; Di Sante, D.; Perez-Mato, J. M.; Macalik, L. Experimental and Theoretical Studies of Structural Phase Transition in a Novel Polar Perovskite-Like [C 2 H 5 Nh 3][Na 0.5 Fe 0.5 (Hcoo) 3] Formate. *Dalton transactions* **2016**, *45*, 2574−2583.
(16) Frost, J. M.; Butler, K. T.; Brivio, F.; Hendon, C. H.; Van Schilfgaarde, M.; Walsh, A. Atomistic Origins of High-Performance in Hybrid Halide Perovskite Solar Cells. *Nano Lett.* **2014**, *14*, 2584−2590.
(17) Anusca, I.; Balčiūnas, S.; Gemeiner, P.; Svirskas, Š.; Sanlialp, M.; Lackner, G.; Fettkenhauer, C.; Belovickis, J.; Samulionis, V.; Ivanov, M.; Dkhil, B.; Banys, J.; Shvartsman, V. V.; Lupascu, D. C. Dielectric Response: Answer to Many Questions in the Methylammonium Lead Halide Solar Cell Absorbers. *Adv. Energy Mater.* **2017**, *7*, 1700600.
(18) Tan, H.; Che, F.; Wei, M.; Zhao, Y.; Saidaminov, M. I.; Todorović, P.; Broberg, D.; Walters, G.; Tan, F.; Zhuang, T.; Sun, B.; Liang, Z.; Yuan, H.; Fron, E.; Kim, J.; Yang, Z.; Voznyy, O.; Asta, M.; Sargent, E. H. Dipolar Cations Confer Defect Tolerance in Wide-Bandgap Metal Halide Perovskites. *Nat. Commun.* **2018**, *9*, 3100.
(19) Drużbicki, K.; Pinna, R. S.; Rudić, S.; Jura, M.; Gorini, G.; Fernandez-Alonso, F. Unexpected Cation Dynamics in the Low-Temperature Phase of Methylammonium Lead Iodide: The Need for Improved Models. *J. Phys. Chem. Lett.* **2016**, *7*, 4701−4709.
(20) Brivio, F.; Frost, J. M.; Skelton, J. M.; Jackson, A. J.; Weber, O. J.; Weller, M. T.; Goni, A. R.; Leguy, A. M.; Barnes, P. R.; Walsh, A. Lattice Dynamics and Vibrational Spectra of the Orthorhombic, Tetragonal, and Cubic Phases of Methylammonium Lead Iodide. *Phys. Rev. B: Condens. Matter Mater. Phys.* **2015**, *92*, 144308.
(21) Pérez-Osorio, M. A.; Milot, R. L.; Filip, M. R.; Patel, J. B.; Herz, L. M.; Johnston, M. B.; Giustino, F. Vibrational Properties of the Organic−Inorganic Halide Perovskite Ch3nh3pbi3 from Theory and Experiment: Factor Group Analysis, First-Principles Calculations, and Low-Temperature Infrared Spectra. *J. Phys. Chem. C* **2015**, *119*, 25703−25718.
(22) Mattoni, A.; Filippetti, A.; Saba, M.; Caddeo, C.; Delugas, P. Temperature Evolution of Methylammonium Trihalide Vibrations at the Atomic Scale. *J. Phys. Chem. Lett.* **2016**, *7*, 529−535.
(23) Leguy, A. M.; Goñi, A. R.; Frost, J. M.; Skelton, J.; Brivio, F.; Rodríguez-Martínez, X.; Weber, O. J.; Pallipurath, A.; Alonso, M. I.; Campoy-Quiles, M.; Weller, M. T.; Nelson, J.; Walsh, A.; Barnes, P. R. F. Dynamic Disorder, Phonon Lifetimes, and the Assignment of Modes to the Vibrational Spectra of Methylammonium Lead Halide Perovskites. *Phys. Chem. Chem. Phys.* **2016**, *18*, 27051−27066.
(24) Li, B.; Kawakita, Y.; Liu, Y.; Wang, M.; Matsuura, M.; Shibata, K.; Ohira-Kawamura, S.; Yamada, T.; Lin, S.; Nakajima, K.; Liu, S. F. Polar Rotor Scattering as Atomic-Level Origin of Low Mobility and Thermal Conductivity of Perovskite Ch3nh3pbi3. *Nat. Commun.* **2017**, *8*, 16086.
(25) Lotsch, B. V. New Light on an Old Story: Perovskites Go Solar. *Angew. Chem., Int. Ed.* **2014**, *53*, 635−637.
(26) Quan, L. N.; Yuan, M.; Comin, R.; Voznyy, O.; Beauregard, E. M.; Hoogland, S.; Buin, A.; Kirmani, A. R.; Zhao, K.; Amassian, A.; et al. Ligand-Stabilized Reduced-Dimensionality Perovskites. *J. Am. Chem. Soc.* **2016**, *138*, 2649−2655.
(27) De Wolf, S.; Holovsky, J.; Moon, S.-J.; Löper, P.; Niesen, B.; Ledinsky, M.; Haug, F.-J.; Yum, J.-H.; Ballif, C. Organometallic Halide Perovskites: Sharp Optical Absorption Edge and Its Relation to Photovoltaic Performance. *J. Phys. Chem. Lett.* **2014**, *5*, 1035−1039.
(28) Shi, D.; Adinolfi, V.; Comin, R.; Yuan, M.; Alarousu, E.; Buin, A.; Chen, Y.; Hoogland, S.; Rothenberger, A.; Katsiev, K.; et al. Low Trap-State Density and Long Carrier Diffusion in Organolead Trihalide Perovskite Single Crystals. *Science* **2015**, *347*, 519−522.
(29) Senanayak, S. P.; Yang, B.; Thomas, T. H.; Giesbrecht, N.; Huang, W.; Gann, E.; Nair, B.; Goedel, K.; Guha, S.; Moya, X.; McNeill, C. R.; Docampo, P.; Sadhanala, A.; Friend, R. H.; Sirringhaus, H. Understanding Charge Transport in Lead Iodide Perovskite Thin-Film Field-Effect Transistors. *Science Advances* **2017**, *3*, No. e1601935.
(30) Philippe, B.; Jacobsson, T. J.; Correa-Baena, J.-P.; Jena, N. K.; Banerjee, A.; Chakraborty, S.; Cappel, U. B.; Ahuja, R.; Hagfeldt, A.; Odelius, M.; Rensmo, H. Valence Level Character in a Mixed Perovskite Material and Determination of the Valence Band Maximum from Photoelectron Spectroscopy: Variation with Photon Energy. *J. Phys. Chem. C* **2017**, *121*, 26655−26666.
(31) Saliba, M.; Matsui, T.; Seo, J. Y.; Domanski, K.; Correa-Baena, J. P.; Nazeeruddin, M. K.; Zakeeruddin, S. M.; Tress, W.; Abate, A.; Hagfeldt, A.; et al. Cesium-Containing Triple Cation Perovskite Solar Cells: Improved Stability, Reproducibility and High Efficiency. *Energy Environ. Sci.* **2016**, *9*, 1989−1997.
(32) Abdi-Jalebi, M.; Andaji-Garmaroudi, Z.; Cacovich, S.; Stavrakas, C.; Philippe, B.; Richter, J. M.; Alsari, M.; Booker, E. P.; Hutter, E. M.; Pearson, A. J.; Lilliu, S.; Savenije, T. J.; Rensmo, H.; Divitini, G.; Ducati, C.; Friend, R. H.; Stranks, S. D. Maximizing and Stabilizing Luminescence from Halide Perovskites with Potassium Passivation. *Nature* **2018**, *555*, 497−501.
(33) Abdi-Jalebi, M.; Andaji-Garmaroudi, Z.; Cacovich, S.; Stavrakas, C.; Philippe, B.; Richter, J. M.; Alsari, M.; Booker, E. P.; Hutter, E. M.; Pearson, A. J.; Lilliu, S.; Savenije, T. J.; Rensmo, H.; Divitini, G.; Ducati, C.; Friend, R. H.; Stranks, S. D. Maximizing and Stabilizing Luminescence from Halide Perovskites with Potassium Passivation. *Nature* **2018**, *555*, 497−501.
(34) Xiao, Z.; Zhao, L.; Tran, N. L.; Lin, Y. L.; Silver, S. H.; Kerner, R. A.; Yao, N.; Kahn, A.; Scholes, G. D.; Rand, B. P. Mixed-Halide Perovskites with Stabilized Bandgaps. *Nano Lett.* **2017**, *17*, 6863−6869.
(35) Li, N.; Zhu, Z.; Li, J.; Jen, A. K. Y.; Wang, L. Inorganic Cspb1-Xsnxibr2 for Efficient Wide-Bandgap Perovskite Solar Cells. *Adv. Energy Mater.* **2018**, *8*, 1800525.
(36) de Quilettes, D. W.; Vorpahl, S. M.; Stranks, S. D.; Nagaoka, H.; Eperon, M. E.; Ziffer, H. J.; Snaith, D. S.; Ginger. Impact of

DOI: 10.1021/acs.chemrev.9b00107
Chem. Rev. 2019, 119, 7444−7477

Microstructure on Local Carrier Lifetime in Perovskite Solar Cells. *Science* **2015**, *348*, 683−686.
(37) Mitzi, D. B. Synthesis, Structure, and Properties of Organic-Inorganic Perovskites and Related Materials. *Prog. Inorg. Chem.* **2007**, 1−121.
(38) Mitzi, D. B.; Feild, C.; Harrison, W.; Guloy, A. Conducting Tin Halides with a Layered Organic-Based Perovskite Structure. *Nature* **1994**, *369*, 467−469.
(39) Hong, X.; Ishihara, T.; Nurmikko, A. Photoconductivity and Electroluminescence in Lead Iodide Based Natural Quantum Well Structures. *Solid State Commun.* **1992**, *84*, 657−661.
(40) Chondroudis, K.; Mitzi, D. B. Electroluminescence from an Organic- Inorganic Perovskite Incorporating a Quaterthiophene Dye within Lead Halide Perovskite Layers. *Chem. Mater.* **1999**, *11*, 3028−3030.
(41) Yuan, M.; Quan, L. N.; Comin, R.; Walters, G.; Sabatini, R.; Voznyy, O.; Hoogland, S.; Zhao, Y.; Beauregard, E. M.; Kanjanaboos, P.; et al. Perovskite Energy Funnels for Efficient Light-Emitting Diodes. *Nat. Nanotechnol.* **2016**, *11*, 872−877.
(42) Xiao, Z.; Kerner, R. A.; Zhao, L.; Tran, N. L.; Lee, K. M.; Koh, T.-W.; Scholes, G. D.; Rand, B. P. Efficient Perovskite Light-Emitting Diodes Featuring Nanometre-Sized Crystallites. *Nat. Photonics* **2017**, *11*, 108−115.
(43) Wang, N.; Cheng, L.; Ge, R.; Zhang, S.; Miao, Y.; Zou, W.; Yi, C.; Sun, Y.; Cao, Y.; Yang, R.; et al. Perovskite Light-Emitting Diodes Based on Solution-Processed Self-Organized Multiple Quantum Wells. *Nat. Photonics* **2016**, *10*, 699−704.
(44) Quan, L. N.; Zhao, Y.; Garcia de Arquer, F. P.; Sabatini, R.; Walters, G.; Voznyy, O.; Comin, R.; Li, Y.; Fan, J. Z.; Tan, H.; Pan, J.; Yuan, M.; Bakr, O. M.; Lu, Z.; Kim, D. H.; Sargent, E. H. Tailoring the Energy Landscape in Quasi-2d Halide Perovskites Enables Efficient Green-Light Emission. *Nano Lett.* **2017**, *17*, 3701−3709.
(45) Byun, J.; Cho, H.; Wolf, C.; Jang, M.; Sadhanala, A.; Friend, R. H.; Yang, H.; Lee, T. W. Efficient Visible Quasi-2d Perovskite Light-Emitting Diodes. *Adv. Mater.* **2016**, *28*, 7515−7520.
(46) Tsai, H.; Nie, W.; Blancon, J. C.; Stoumpos, C. C.; Asadpour, R.; Harutyunyan, B.; Neukirch, A. J.; Verduzco, R.; Crochet, J. J.; Tretiak, S.; et al. High-Efficiency Two-Dimensional Ruddlesden-Popper Perovskite Solar Cells. *Nature* **2016**, *536*, 312−316.
(47) Cao, D. H.; Stoumpos, C. C.; Farha, O. K.; Hupp, J. T.; Kanatzidis, M. G. 2d Homologous Perovskites as Light-Absorbing Materials for Solar Cell Applications. *J. Am. Chem. Soc.* **2015**, *137*, 7843−7850.
(48) Mitzi, D.; Wang, S.; Feild, C.; Chess, C.; Guloy, A. Conducting Layered Organic-Inorganic Halides Containing < 110>-Oriented Perovskite Sheets. *Science* **1995**, *267*, 1473−1476.
(49) Li, Y.; Zheng, G.; Lin, C.; Lin, J. Synthesis, Structure and Optical Properties of Different Dimensional Organic−Inorganic Perovskites. *Solid State Sci.* **2007**, *9*, 855−861.
(50) Sun, S.; Tominaka, S.; Lee, J.-H.; Xie, F.; Bristowe, P. D.; Cheetham, A. K. Synthesis, Crystal Structure, and Properties of a Perovskite-Related Bismuth Phase,(Nh4) 3bi2i9. *APL Mater.* **2016**, *4*, 031101.
(51) Zaleski, J.; Pietraszko, A. Structure at 200 and 298 K and X-Ray Investigations of the Phase Transition at 242 K of [Nh2(Ch3)2]-3sb2cl9(Dmaca). *Acta Crystallogr., Sect. B: Struct. Sci.* **1996**, *52*, 287−295.
(52) Kallel, A.; Bats, J. Tris (Trimethylammonium) Nonachlorodiantimonate (Iii),[Nh(Ch3)3]3[Sb2cl9]. *Acta Crystallogr., Sect. C: Cryst. Struct. Commun.* **1985**, *41*, 1022−1024.
(53) Dohner, E. R.; Hoke, E. T.; Karunadasa, H. I. Self-Assembly of Broadband White-Light Emitters. *J. Am. Chem. Soc.* **2014**, *136*, 1718−1721.
(54) Dohner, E. R.; Jaffe, A.; Bradshaw, L. R.; Karunadasa, H. I. Intrinsic White-Light Emission from Layered Hybrid Perovskites. *J. Am. Chem. Soc.* **2014**, *136*, 13154−13157.
(55) Hu, T.; Smith, M. D.; Dohner, E. R.; Sher, M.-J.; Wu, X.; Trinh, M. T.; Fisher, A.; Corbett, J.; Zhu, X.-Y.; Karunadasa, H. I.; Lindenberg, A. M. Mechanism for Broadband White-Light Emission from Two-Dimensional (110) Hybrid Perovskites. *J. Phys. Chem. Lett.* **2016**, *7*, 2258−2263.
(56) Mao, L.; Wu, Y.; Stoumpos, C. C.; Wasielewski, M. R.; Kanatzidis, M. G. White-Light Emission and Structural Distortion in New Corrugated Two-Dimensional Lead Bromide Perovskites. *J. Am. Chem. Soc.* **2017**, *139*, 5210−5215.
(57) Mao, L.; Wu, Y.; Stoumpos, C. C.; Wasielewski, M. R.; Kanatzidis, M. G. White-Light Emission and Structural Distortion in New Corrugated Two-Dimensional Lead Bromide Perovskites. *J. Am. Chem. Soc.* **2017**, *139*, 5210−5215.
(58) Nikl, M.; Mihokova, E.; Nitsch, K.; Somma, F.; Giampaolo, C.; Pazzi, G.; Fabeni, P.; Zazubovich, S. Photoluminescence of Cs4pbbr6 Crystals and Thin Films. *Chem. Phys. Lett.* **1999**, *306*, 280−284.
(59) Palazon, F.; Almeida, G.; Akkerman, Q. A.; De Trizio, L.; Dang, Z.; Prato, M.; Manna, L. Changing the Dimensionality of Cesium Lead Bromide Nanocrystals by Reversible Postsynthesis Transformations with Amines. *Chem. Mater.* **2017**, *29*, 4167−4171.
(60) Wu, L.; Hu, H.; Xu, Y.; Jiang, S.; Chen, M.; Zhong, Q.; Yang, D.; Liu, Q.; Zhao, Y.; Sun, B.; Zhang, Q.; Yin, Y. From Nonluminescent Cs4pbx6 (X= Cl, Br, I) Nanocrystals to Highly Luminescent Cspbx3 Nanocrystals: Water-Triggered Transformation through a Csx-Stripping Mechanism. *Nano Lett.* **2017**, *17*, 5799−5804.
(61) Palazon, F.; Urso, C.; De Trizio, L.; Akkerman, Q.; Marras, S.; Locardi, F.; Nelli, I.; Ferretti, M.; Prato, M.; Manna, L. Postsynthesis Transformation of Insulating Cs4pbbr6 Nanocrystals into Bright Perovskite Cspbbr3 through Physical and Chemical Extraction of Csbr. *ACS Energy Lett.* **2017**, *2*, 2445−2448.
(62) Liu, Z.; Bekenstein, Y.; Ye, X.; Nguyen, S. C.; Swabeck, J.; Zhang, D.; Lee, S.-T.; Yang, P.; Ma, W.; Alivisatos, A. P. Ligand Mediated Transformation of Cesium Lead Bromide Perovskite Nanocrystals to Lead Depleted Cs4pbbr6 Nanocrystals. *J. Am. Chem. Soc.* **2017**, *139*, 5309−5312.
(63) Quan, L. N.; Quintero-Bermudez, R.; Voznyy, O.; Walters, G.; Jain, A.; Fan, J. Z.; Zheng, X.; Yang, Z.; Sargent, E. H. Highly Emissive Green Perovskite Nanocrystals in a Solid State Crystalline Matrix. *Adv. Mater.* **2017**, *29*, 1605945.
(64) Chen, X.; Zhang, F.; Ge, Y.; Shi, L.; Huang, S.; Tang, J.; Lv, Z.; Zhang, L.; Zou, B.; Zhong, H. Centimeter-Sized Cs4pbbr6 Crystals with Embedded Cspbbr3 Nanocrystals Showing Superior Photoluminescence: Nonstoichiometry Induced Transformation and Light-Emitting Applications. *Adv. Funct. Mater.* **2018**, *28*, 1706567.
(65) Savory, C. N.; Walsh, A.; Scanlon, D. O. Can Pb-Free Halide Double Perovskites Support High-Efficiency Solar Cells? *ACS Energy Lett.* **2016**, *1*, 949−955.
(66) Xiao, Z.; Zhou, Y.; Hosono, H.; Kamiya, T. Intrinsic Defects in a Photovoltaic Perovskite Variant Cs2sni6. *Phys. Chem. Chem. Phys.* **2015**, *17*, 18900−18903.
(67) Jain, A.; Voznyy, O.; Sargent, E. H. High-Throughput Screening of Lead-Free Perovskite-Like Materials for Optoelectronic Applications. *J. Phys. Chem. C* **2017**, *121*, 7183−7187.
(68) Slavney, A. H.; Hu, T.; Lindenberg, A. M.; Karunadasa, H. I. A Bismuth-Halide Double Perovskite with Long Carrier Recombination Lifetime for Photovoltaic Applications. *J. Am. Chem. Soc.* **2016**, *138*, 2138−2141.
(69) Shi, Z.; Guo, J.; Chen, Y.; Li, Q.; Pan, Y.; Zhang, H.; Xia, Y.; Huang, W. Lead-Free Organic−Inorganic Hybrid Perovskites for Photovoltaic Applications: Recent Advances and Perspectives. *Adv. Mater.* **2017**, *29*, 1605005.
(70) Lee, S. J.; Shin, S. S.; Kim, Y. C.; Kim, D.; Ahn, T. K.; Noh, J. H.; Seo, J.; Seok, S. I. Fabrication of Efficient Formamidinium Tin Iodide Perovskite Solar Cells through Snf2−Pyrazine Complex. *J. Am. Chem. Soc.* **2016**, *138*, 3974−3977.
(71) Gupta, S.; Cahen, D.; Hodes, G. How Snf2 Impacts the Material Properties of Lead-Free Tin Perovskites. *J. Phys. Chem. C* **2018**, *122*, 13926−13936.
(72) Yuan, F.; Xi, J.; Dong, H.; Xi, K.; Zhang, W.; Ran, C.; Jiao, B.; Hou, X.; Jen, A. K. Y.; Wu, Z. All-Inorganic Hetero-Structured Cesium Tin Halide Perovskite Light-Emitting Diodes with Current

DOI: 10.1021/acs.chemrev.9b00107
Chem. Rev. 2019, 119, 7444−7477

Density over 900 a Cm-2 and Its Amplified Spontaneous Emission Behaviors. *Phys. Status Solidi RRL* **2018**, *12*, 1800090.
(73) Lanzetta, L.; Marin-Beloqui, J. M.; Sanchez-Molina, I.; Ding, D.; Haque, S. A. Two-Dimensional Organic Tin Halide Perovskites with Tunable Visible Emission and Their Use in Light-Emitting Devices. *ACS Energy Lett.* **2017**, *2*, 1662−1668.
(74) Stoumpos, C. C.; Frazer, L.; Clark, D. J.; Kim, Y. S.; Rhim, S. H.; Freeman, A. J.; Ketterson, J. B.; Jang, J. I.; Kanatzidis, M. G. Hybrid Germanium Iodide Perovskite Semiconductors: Active Lone Pairs, Structural Distortions, Direct and Indirect Energy Gaps, and Strong Nonlinear Optical Properties. *J. Am. Chem. Soc.* **2015**, *137*, 6804−6819.
(75) Filip, M. R.; Hillman, S.; Haghighirad, A. A.; Snaith, H. J.; Giustino, F. Band Gaps of the Lead-Free Halide Double Perovskites Cs2biagcl6 and Cs2biagbr6 from Theory and Experiment. *J. Phys. Chem. Lett.* **2016**, *7*, 2579−2585.
(76) Vargas, B.; Ramos, E.; Pérez-Gutiérrez, E.; Alonso, J. C.; Solis-Ibarra, D. A Direct Bandgap Copper−Antimony Halide Perovskite. *J. Am. Chem. Soc.* **2017**, *139*, 9116−9119.
(77) Leng, M.; Chen, Z.; Yang, Y.; Li, Z.; Zeng, K.; Li, K.; Niu, G.; He, Y.; Zhou, Q.; Tang, J. Lead-Free, Blue Emitting Bismuth Halide Perovskite Quantum Dots. *Angew. Chem., Int. Ed.* **2016**, *55*, 15012−15016.
(78) Wehrenfennig, C.; Liu, M.; Snaith, H. J.; Johnston, M. B.; Herz, L. M. Charge-Carrier Dynamics in Vapour-Deposited Films of the Organolead Halide Perovskite Ch3nh3pbi3-Xclx. *Energy Environ. Sci.* **2014**, *7*, 2269−2275.
(79) Stranks, S. D.; Eperon, G. E.; Grancini, G.; Menelaou, C.; Alcocer, M. J.; Leijtens, T.; Herz, L. M.; Petrozza, A.; Snaith, H. J. Electron-Hole Diffusion Lengths Exceeding 1 Micrometer in an Organometal Trihalide Perovskite Absorber. *Science* **2013**, *342*, 341−344.
(80) Brenner, T. M.; Egger, D. A.; Rappe, A. M.; Kronik, L.; Hodes, G.; Cahen, D. Are Mobilities in Hybrid Organic−Inorganic Halide Perovskites Actually "High"? *J. Phys. Chem. Lett.* **2015**, *6*, 4754−4757.
(81) Oga, H.; Saeki, A.; Ogomi, Y.; Hayase, S.; Seki, S. Improved Understanding of the Electronic and Energetic Landscapes of Perovskite Solar Cells: High Local Charge Carrier Mobility, Reduced Recombination, and Extremely Shallow Traps. *J. Am. Chem. Soc.* **2014**, *136*, 13818−13825.
(82) Sum, T. C.; Mathews, N.; Xing, G.; Lim, S. S.; Chong, W. K.; Giovanni, D.; Dewi, H. A. Spectral Features and Charge Dynamics of Lead Halide Perovskites: Origins and Interpretations. *Acc. Chem. Res.* **2016**, *49*, 294−302.
(83) Manser, J. S.; Kamat, P. V. Band Filling with Free Charge Carriers in Organometal Halide Perovskites. *Nat. Photonics* **2014**, *8*, 737−743.
(84) Saba, M.; Cadelano, M.; Marongiu, D.; Chen, F.; Sarritzu, V.; Sestu, N.; Figus, C.; Aresti, M.; Piras, R.; Geddo Lehmann, A.; Cannas, C.; Musinu, A.; Quochi, F.; Mura, A.; Bongiovanni, G. Correlated Electron−Hole Plasma in Organometal Perovskites. *Nat. Commun.* **2014**, *5*, 5049.
(85) Yamada, Y.; Nakamura, T.; Endo, M.; Wakamiya, A.; Kanemitsu, Y. Photocarrier Recombination Dynamics in Perovskite Ch3nh3pbi3 for Solar Cell Applications. *J. Am. Chem. Soc.* **2014**, *136*, 11610−11613.
(86) Manger, L. H.; Rowley, M. B.; Fu, Y.; Foote, A. K.; Rea, M. T.; Wood, S. L.; Jin, S.; Wright, J. C.; Goldsmith, R. H. Global Analysis of Perovskite Photophysics Reveals Importance of Geminate Pathways. *J. Phys. Chem. C* **2017**, *121*, 1062−1071.
(87) Stamplecoskie, K. G.; Manser, J. S.; Kamat, P. V. Dual Nature of the Excited State in Organic−Inorganic Lead Halide Perovskites. *Energy Environ. Sci.* **2015**, *8*, 208−215.
(88) Wehrenfennig, C.; Eperon, G. E.; Johnston, M. B.; Snaith, H. J.; Herz, L. M. High Charge Carrier Mobilities and Lifetimes in Organolead Trihalide Perovskites. *Adv. Mater.* **2014**, *26*, 1584−1589.
(89) Johnston, M. B.; Herz, L. M. Hybrid Perovskites for Photovoltaics: Charge-Carrier Recombination, Diffusion, and Radiative Efficiencies. *Acc. Chem. Res.* **2016**, *49*, 146−154.
(90) Richter, J. M.; Abdi-Jalebi, M.; Sadhanala, A.; Tabachnyk, M.; Rivett, J. P.; Pazos-Outón, L. M.; Gödel, K. C.; Price, M.; Deschler, F.; Friend, R. H. Enhancing Photoluminescence Yields in Lead Halide Perovskites by Photon Recycling and Light out-Coupling. *Nat. Commun.* **2016**, *7*, 13941.
(91) Yang, Y.; Ostrowski, D. P.; France, R. M.; Zhu, K.; van de Lagemaat, J.; Luther, J. M.; Beard, M. C. Observation of a Hot-Phonon Bottleneck in Lead-Iodide Perovskites. *Nat. Photonics* **2016**, *10*, 53−59.
(92) Rehman, W.; Milot, R. L.; Eperon, G. E.; Wehrenfennig, C.; Boland, J. L.; Snaith, H. J.; Johnston, M. B.; Herz, L. M. Charge-Carrier Dynamics and Mobilities in Formamidinium Lead Mixed-Halide Perovskites. *Adv. Mater.* **2015**, *27*, 7938−7944.
(93) Beattie, A.; Landsberg, P. Auger Effect in Semiconductors. *Proc. R. Soc. London, Ser. A* **1959**, *249*, 16−29.
(94) Sheik-Bahae, M.; Epstein, R. I. Can Laser Light Cool Semiconductors? *Phys. Rev. Lett.* **2004**, *92*, 247403.
(95) Even, J.; Pedesseau, L.; Katan, C. Analysis of Multivalley and Multibandgap Absorption and Enhancement of Free Carriers Related to Exciton Screening in Hybrid Perovskites. *J. Phys. Chem. C* **2014**, *118*, 11566−11572.
(96) Tanaka, K.; Takahashi, T.; Ban, T.; Kondo, T.; Uchida, K.; Miura, N. Comparative Study on the Excitons in Lead-Halide-Based Perovskite-Type Crystals Ch3nh3pbbr3 Ch3nh3pbi3. *Solid State Commun.* **2003**, *127*, 619−623.
(97) Hirasawa, M.; Ishihara, T.; Goto, T.; Uchida, K.; Miura, N. Magnetoabsorption of the Lowest Exciton in Perovskite-Type Compound (Ch3nh3) Pbi3. *Phys. B* **1994**, *201*, 427−430.
(98) Lin, Q.; Armin, A.; Nagiri, R. C. R.; Burn, P. L.; Meredith, P. Electro-Optics of Perovskite Solar Cells. *Nat. Photonics* **2015**, *9*, 106−112.
(99) Miyata, A.; Mitioglu, A.; Plochocka, P.; Portugall, O.; Wang, J. T.-W.; Stranks, S. D.; Snaith, H. J.; Nicholas, R. J. Direct Measurement of the Exciton Binding Energy and Effective Masses for Charge Carriers in Organic-Inorganic Tri-Halide Perovskites. *Nat. Phys.* **2015**, *11*, 582−587.
(100) D'Innocenzo, V.; Grancini, G.; Alcocer, M. J.; Kandada, A. R.; Stranks, S. D.; Lee, M. M.; Lanzani, G.; Snaith, H. J.; Petrozza, A. Excitons Versus Free Charges in Organo-Lead Tri-Halide Perovskites. *Nat. Commun.* **2014**, *5*, 3586.
(101) Savenije, T. J.; Ponseca, C. S., Jr; Kunneman, L.; Abdellah, M.; Zheng, K.; Tian, Y.; Zhu, Q.; Canton, S. E.; Scheblykin, I. G.; Pullerits, T.; Yartsev, A.; Sundström, V. Thermally Activated Exciton Dissociation and Recombination Control the Carrier Dynamics in Organometal Halide Perovskite. *J. Phys. Chem. Lett.* **2014**, *5*, 2189−2194.
(102) Wu, K.; Bera, A.; Ma, C.; Du, Y.; Yang, Y.; Li, L.; Wu, T. Temperature-Dependent Excitonic Photoluminescence of Hybrid Organometal Halide Perovskite Films. *Phys. Chem. Chem. Phys.* **2014**, *16*, 22476−22481.
(103) Sestu, N.; Cadelano, M.; Sarritzu, V.; Chen, F.; Marongiu, D.; Piras, R.; Mainas, M.; Quochi, F.; Saba, M.; Mura, A.; Bongiovanni, G. Absorption F-Sum Rule for the Exciton Binding Energy in Methylammonium Lead Halide Perovskites. *J. Phys. Chem. Lett.* **2015**, *6*, 4566−4572.
(104) Sun, S.; Salim, T.; Mathews, N.; Duchamp, M.; Boothroyd, C.; Xing, G.; Sum, T. C.; Lam, Y. M. The Origin of High Efficiency in Low-Temperature Solution-Processable Bilayer Organometal Halide Hybrid Solar Cells. *Energy Environ. Sci.* **2014**, *7*, 399−407.
(105) Nah, S.; Spokoyny, B.; Stoumpos, C.; Soe, C. M. M.; Kanatzidis, M.; Harel, E. Spatially Segregated Free-Carrier and Exciton Populations in Individual Lead Halide Perovskite Grains. *Nat. Photonics* **2017**, *11*, 285−288.
(106) Gélvez-Rueda, M. C.; Hutter, E. M.; Cao, D. H.; Renaud, N.; Stoumpos, C. C.; Hupp, J. T.; Savenije, T. J.; Kanatzidis, M. G.; Grozema, F. C. Interconversion between Free Charges and Bound Excitons in 2d Hybrid Lead Halide Perovskites. *J. Phys. Chem. C* **2017**, *121*, 26566−26574.

DOI: 10.1021/acs.chemrev.9b00107
Chem. Rev. 2019, 119, 7444−7477

(107) de Mello, J. C.; Wittmann, H. F.; Friend, R. H. An Improved Experimental Determination of External Photoluminescence Quantum Efficiency. *Adv. Mater.* **1997**, *9*, 230−232.
(108) Deschler, F.; Price, M.; Pathak, S.; Klintberg, L. E.; Jarausch, D.-D.; Higler, R.; Hüttner, S.; Leijtens, T.; Stranks, S. D.; Snaith, H. J.; et al. High Photoluminescence Efficiency and Optically Pumped Lasing in Solution-Processed Mixed Halide Perovskite Semiconductors. *J. Phys. Chem. Lett.* **2014**, *5*, 1421−1426.
(109) Pan, J.; Quan, L. N.; Zhao, Y.; Peng, W.; Murali, B.; Sarmah, S. P.; Yuan, M.; Sinatra, L.; Alyami, N. M.; Liu, J.; et al. Highly Efficient Perovskite-Quantum-Dot Light-Emitting Diodes by Surface Engineering. *Adv. Mater.* **2016**, *28*, 8718−8725.
(110) Liu, F.; Zhang, Y.; Ding, C.; Kobayashi, S.; Izuishi, T.; Nakazawa, N.; Toyoda, T.; Ohta, T.; Hayase, S.; Minemoto, T.; Yoshino, K.; Dai, S.; Shen, Q. Highly Luminescent Phase-Stable Cspbi3 Perovskite Quantum Dots Achieving near 100% Absolute Photoluminescence Quantum Yield. *ACS Nano* **2017**, *11*, 10373−10383.
(111) Hattori, T.; Taira, T.; Era, M.; Tsutsui, T.; Saito, S. Highly Efficient Electroluminescence from a Heterostructure Device Combined with Emissive Layered-Perovskite and an Electron-Transporting Organic Compound. *Chem. Phys. Lett.* **1996**, *254*, 103−108.
(112) Kim, Y. H.; Cho, H.; Heo, J. H.; Kim, T. S.; Myoung, N.; Lee, C. L.; Im, S. H.; Lee, T. W. Multicolored Organic/Inorganic Hybrid Perovskite Light-Emitting Diodes. *Adv. Mater.* **2015**, *27*, 1248.
(113) Li, G.; Tan, Z. K.; Di, D.; Lai, M. L.; Jiang, L.; Lim, J. H.; Friend, R. H.; Greenham, N. C. Efficient Light-Emitting Diodes Based on Nanocrystalline Perovskite in a Dielectric Polymer Matrix. *Nano Lett.* **2015**, *15*, 2640−2644.
(114) Li, J.; Bade, S. G.; Shan, X.; Yu, Z. Single-Layer Light-Emitting Diodes Using Organometal Halide Perovskite/Poly(Ethylene Oxide) Composite Thin Films. *Adv. Mater.* **2015**, *27*, 5196.
(115) Park, M.-H.; Jeong, S.-H.; Seo, H.-K.; Wolf, C.; Kim, Y.-H.; Kim, H.; Byun, J.; Kim, J. S.; Cho, H.; Lee, T.-W. Unravelling Additive-Based Nanocrystal Pinning for High Efficiency Organic-Inorganic Halide Perovskite Light-Emitting Diodes. *Nano Energy* **2017**, *42*, 157−165.
(116) Cho, H.; Kim, J. S.; Wolf, C.; Kim, Y.-H.; Yun, H. J.; Jeong, S.-H.; Sadhanala, A.; Venugopalan, V.; Choi, J. W.; Lee, C.-L.; et al. High-Efficiency Polycrystalline Perovskite Light-Emitting Diodes Based on Mixed Cations. *ACS Nano* **2018**, *12*, 2883−2892.
(117) Zhang, S.; Yi, C.; Wang, N.; Sun, Y.; Zou, W.; Wei, Y.; Cao, Y.; Miao, Y.; Li, R.; Yin, Y.; Zhao, N.; Wang, J.; Huang, W. Efficient Red Perovskite Light-Emitting Diodes Based on Solution-Processed Multiple Quantum Wells. *Adv. Mater.* **2017**, *29*, 1606600.
(118) Rehman, W.; McMeekin, D. P.; Patel, J. B.; Milot, R. L.; Johnston, M. B.; Snaith, H. J.; Herz, L. M. Photovoltaic Mixed-Cation Lead Mixed-Halide Perovskites: Links between Crystallinity, Photo-Stability and Electronic Properties. *Energy Environ. Sci.* **2017**, *10*, 361−369.
(119) Kulkarni, S. A.; Muduli, S.; Xing, G.; Yantara, N.; Li, M.; Chen, S.; Sum, T. C.; Mathews, N.; White, T. J.; Mhaisalkar, S. G. Modulating Excitonic Recombination Effects through One-Step Synthesis of Perovskite Nanoparticles for Light-Emitting Diodes. *ChemSusChem* **2017**, *10*, 3818−3824.
(120) Protesescu, L.; Yakunin, S.; Bodnarchuk, M. I.; Krieg, F.; Caputo, R.; Hendon, C. H.; Yang, R. X.; Walsh, A.; Kovalenko, M. V. Nanocrystals of Cesium Lead Halide Perovskites (Cspbx(3), X = Cl, Br, and I): Novel Optoelectronic Materials Showing Bright Emission with Wide Color Gamut. *Nano Lett.* **2015**, *15*, 3692−3696.
(121) Li, G.; Rivarola, F. W.; Davis, N. J.; Bai, S.; Jellicoe, T. C.; de la Pena, F.; Hou, S.; Ducati, C.; Gao, F.; Friend, R. H.; et al. Highly Efficient Perovskite Nanocrystal Light-Emitting Diodes Enabled by a Universal Crosslinking Method. *Adv. Mater.* **2016**, *28*, 3528−3534.
(122) Song, J.; Li, J.; Li, X.; Xu, L.; Dong, Y.; Zeng, H. Quantum Dot Light-Emitting Diodes Based on Inorganic Perovskite Cesium Lead Halides (Cspbx3). *Adv. Mater.* **2015**, *27*, 7162−7167.
(123) Li, J.; Xu, L.; Wang, T.; Song, J.; Chen, J.; Xue, J.; Dong, Y.; Cai, B.; Shan, Q.; Han, B.; et al. 50-Fold Eqe Improvement up to 6.27% of Solution Processed All-Inorganic Perovskite Cspbbr3 Qleds Via Surface Ligand Density Control. *Adv. Mater.* **2017**, *29*, 1603885.
(124) Zhang, X.; Liu, H.; Wang, W.; Zhang, J.; Xu, B.; Karen, K. L.; Zheng, Y.; Liu, S.; Chen, S.; Wang, K.; et al. Hybrid Perovskite Light-Emitting Diodes Based on Perovskite Nanocrystals with Organic-Inorganic Mixed Cations. *Adv. Mater.* **2017**, *29*, 1606405.
(125) Yuan, S.; Wang, Z.-K.; Zhuo, M.-P.; Tian, Q.; Jin, Y.; Liao, L.-S. Self-Assembled High Quality Cspbbr3 Quantum Dot Films toward Highly Efficient Light-Emitting Diodes. *ACS Nano* **2018**, *12*, 9541−9548.
(126) Protesescu, L.; Yakunin, S.; Kumar, S.; Bär, J.; Bertolotti, F.; Masciocchi, N.; Guagliardi, A.; Grotevent, M.; Shorubalko, I.; Bodnarchuk, M. I.; Shih, C.-J.; Kovalenko, M. V. Dismantling the "Red Wall" of Colloidal Perovskites: Highly Luminescent Formamidinium and Formamidinium−Cesium Lead Iodide Nanocrystals. *ACS Nano* **2017**, *11*, 3119−3134.
(127) Kim, Y.-H.; Lee, G.-H.; Kim, Y.-T.; Wolf, C.; Yun, H. J.; Kwon, W.; Park, C. G.; Lee, T.-W. High Efficiency Perovskite Light-Emitting Diodes of Ligand-Engineered Colloidal Formamidinium Lead Bromide Nanoparticles. *Nano Energy* **2017**, *38*, 51−58.
(128) Kim, Y.-H.; Wolf, C.; Kim, Y.-T.; Cho, H.; Kwon, W.; Do, S.; Sadhanala, A.; Park, C. G.; Rhee, S.-W.; Im, S. H.; Friend, R. H.; Lee, T.-W. Highly Efficient Light-Emitting Diodes of Colloidal Metal−Halide Perovskite Nanocrystals Beyond Quantum Size. *ACS Nano* **2017**, *11*, 6586−6593.
(129) Chin, X. Y.; Perumal, A.; Bruno, A.; Yantara, N.; Veldhuis, S. A.; Martínez-Sarti, L.; Chandran, B.; Chirvony, V.; Lo, A. S.-Z.; So, J.; Soci, C.; Grätzel, M.; Bolink, H. J.; Mathews, N.; Mhaisalkar, S. G. Self-Assembled Hierarchical Nanostructured Perovskites Enable Highly Efficient Leds Via an Energy Cascade. *Energy Environ. Sci.* **2018**, *11*, 1770−1778.
(130) Yang, J.; Siempelkamp, B. D.; Mosconi, E.; De Angelis, F.; Kelly, T. L. Origin of the Thermal Instability in Ch3nh3pbi3 Thin Films Deposited on Zno. *Chem. Mater.* **2015**, *27*, 4229−4236.
(131) Wang, J.; Wang, N.; Jin, Y.; Si, J.; Tan, Z. K.; Du, H.; Cheng, L.; Dai, X.; Bai, S.; He, H.; et al. Interfacial Control toward Efficient and Low-Voltage Perovskite Light-Emitting Diodes. *Adv. Mater.* **2015**, *27*, 2311.
(132) Chih, Y. K.; Wang, J. C.; Yang, R. T.; Liu, C. C.; Chang, Y. C.; Fu, Y. S.; Lai, W. C.; Chen, P.; Wen, T. C.; Huang, Y. C.; et al. Niox Electrode Interlayer and Ch3nh2 /Ch3nh3pbbr3 Interface Treatment to Markedly Advance Hybrid Perovskite-Based Light-Emitting Diodes. *Adv. Mater.* **2016**, *28*, 8687−8694.
(133) Seo, H. K.; Kim, H.; Lee, J.; Park, M. H.; Jeong, S. H.; Kim, Y. H.; Kwon, S. J.; Han, T. H.; Yoo, S.; Lee, T. W. Efficient Flexible Organic/Inorganic Hybrid Perovskite Light-Emitting Diodes Based on Graphene Anode. *Adv. Mater.* **2017**, *29*, 1605587.
(134) Lee, B. R.; Yu, J. C.; Park, J. H.; Lee, S.; Mai, C.-K.; Zhao, B.; Wong, M. S.; Jung, E. D.; Nam, Y. S.; Park, S. Y.; DiNuzzo, D.; Kim, J. Y.; Stranks, S. D.; Bazan, G. C.; Choi, H.; Song, M. M.; Friend, R. H. Conjugated Polyelectrolytes as Efficient Hole Transport Layers in Perovskite Light-Emitting Diodes. *ACS Nano* **2018**, *12*, 5826−5833.
(135) Zhang, L.; Yang, X.; Jiang, Q.; Wang, P.; Yin, Z.; Zhang, X.; Tan, H.; Yang, Y. M.; Wei, M.; Sutherland, B. R.; et al. Ultra-Bright and Highly Efficient Inorganic Based Perovskite Light-Emitting Diodes. *Nat. Commun.* **2017**, *8*, 15640.
(136) Yan, F.; Xing, J.; Xing, G.; Quan, L.; Tan, S. T.; Zhao, J.; Su, R.; Zhang, L.; Chen, S.; Zhao, Y.; Huan, A.; Sargent, E. H.; Xiong, Q.; Demir, H. V. Highly Efficient Visible Colloidal Lead-Halide Perovskite Nanocrystal Light-Emitting Diodes. *Nano Lett.* **2018**, *18*, 3157−3164.
(137) Lu, L. P.; Kabra, D.; Johnson, K.; Friend, R. H. Charge-Carrier Balance and Color Purity in Polyfluorene Polymer Blends for Blue Light-Emitting Diodes. *Adv. Funct. Mater.* **2012**, *22*, 144−150.
(138) Nguyen, W. H.; Bailie, C. D.; Unger, E. L.; McGehee, M. D. Enhancing the Hole-Conductivity of Spiro-Ometad without Oxygen

DOI: 10.1021/acs.chemrev.9b00107
Chem. Rev. 2019, 119, 7444−7477

or Lithium Salts by Using Spiro (Tfsi) 2 in Perovskite and Dye-Sensitized Solar Cells. *J. Am. Chem. Soc.* **2014**, *136*, 10996−11001.
(139) Hoye, R. L.; Chua, M. R.; Musselman, K. P.; Li, G.; Lai, M. L.; Tan, Z. K.; Greenham, N. C.; MacManus-Driscoll, J. L.; Friend, R. H.; Credgington, D. Enhanced Performance in Fluorene-Free Organometal Halide Perovskite Light-Emitting Diodes Using Tunable, Low Electron Affinity Oxide Electron Injectors. *Adv. Mater.* **2015**, *27*, 1414−1419.
(140) Chih, Y. K.; Wang, J. C.; Yang, R. T.; Liu, C. C.; Chang, Y. C.; Fu, Y. S.; Lai, W. C.; Chen, P.; Wen, T. C.; Huang, Y. C.; Tsao, C.-S.; Guo, T.-F. Niox Electrode Interlayer and Ch3nh2/Ch3nh3pbbr3 Interface Treatment to Markedly Advance Hybrid Perovskite-Based Light-Emitting Diodes. *Adv. Mater.* **2016**, *28*, 8687−8694.
(141) Liang, D.; Peng, Y.; Fu, Y.; Shearer, M. J.; Zhang, J.; Zhai, J.; Zhang, Y.; Hamers, R. J.; Andrew, T. L.; Jin, S. Color-Pure Violet-Light-Emitting Diodes Based on Layered Lead Halide Perovskite Nanoplates. *ACS Nano* **2016**, *10*, 6897−6904.
(142) Xing, J.; Zhao, Y. B.; Askerka, M.; Quan, L. N.; Gong, X. W.; Zhao, W. J.; Zhao, J. X.; Tan, H. R.; Long, G. K.; Gao, L.; Yang, Z.; Voznyy, O.; Tang, J.; Lu, Z.-H.; Xiong, Q.; Sargent, E. H. Color-Stable Highly Luminescent Sky-Blue Perovskite Light-Emitting Diodes. *Nat. Commun.* **2018**, *9*, 3541.
(143) Kim, H. P.; Kim, J.; Kim, B. S.; Kim, H.-M.; Kim, J.; Yusoff, A. R. b. M.; Jang, J.; Nazeeruddin, M. K. High-Efficiency, Blue, Green, and near-Infrared Light-Emitting Diodes Based on Triple Cation Perovskite. *Adv. Opt. Mater.* **2017**, *5*, 1600920.
(144) Pan, J.; Quan, L. N.; Zhao, Y.; Peng, W.; Murali, B.; Sarmah, S. P.; Yuan, M.; Sinatra, L.; Alyami, N. M.; Liu, J.; Yassitepe, E.; Yang, Z.; Voznyy, O.; Comin, R.; Hedhili, M. N.; Mohammed, O. F.; Lu, Z. H.; Kim, D. H.; Sargent, E. H.; Bakr, O. M. Highly Efficient Perovskite-Quantum-Dot Light-Emitting Diodes by Surface Engineering. *Adv. Mater.* **2016**, *28*, 8718−8725.
(145) Hou, S. C.; Gangishetty, M. K.; Quan, Q. M.; Congreve, D. N. Efficient Blue and White Perovskite Light-Emitting Diodes Via Manganese Doping. *Joule* **2018**, *2*, 2421−2433.
(146) Li, Z. C.; Chen, Z. M.; Yang, Y. C.; Xue, Q. F.; Yip, H. L.; Cao, Y. Modulation of Recombination Zone Position for Quasi-Two-Dimensional Blue Perovskite Light-Emitting Diodes with Efficiency Exceeding 5%. *Nat. Commun.* **2019**, *10*, 1027.
(147) Kim, Y. H.; Cho, H.; Heo, J. H.; Kim, T. S.; Myoung, N.; Lee, C. L.; Im, S. H.; Lee, T. W. Multicolored Organic/Inorganic Hybrid Perovskite Light-Emitting Diodes. *Adv. Mater.* **2015**, *27*, 1248−1254.
(148) Li, G.; Tan, Z.-K.; Di, D.; Lai, M. L.; Jiang, L.; Lim, J. H.-W.; Friend, R. H.; Greenham, N. C. Efficient Light-Emitting Diodes Based on Nanocrystalline Perovskite in a Dielectric Polymer Matrix. *Nano Lett.* **2015**, *15*, 2640.
(149) Meng, L.; Yao, E. P.; Hong, Z.; Chen, H.; Sun, P.; Yang, Z.; Li, G.; Yang, Y. Pure Formamidinium-Based Perovskite Light-Emitting Diodes with High Efficiency and Low Driving Voltage. *Adv. Mater.* **2017**, *29*, 1603826.
(150) Li, J.; Bade, S. G. R.; Shan, X.; Yu, Z. Single-Layer Light-Emitting Diodes Using Organometal Halide Perovskite/Poly (Ethylene Oxide) Composite Thin Films. *Adv. Mater.* **2015**, *27*, 5196−5202.
(151) Li, J.; Xu, L.; Wang, T.; Song, J.; Chen, J.; Xue, J.; Dong, Y.; Cai, B.; Shan, Q.; Han, B.; Zeng, H. 50-Fold Eqe Improvement up to 6.27% of Solution-Processed All-Inorganic Perovskite Cspbbr3 Qleds Via Surface Ligand Density Control. *Adv. Mater.* **2017**, *29*, 1603885.
(152) Zhao, L.; Yeh, Y.-W.; Tran, N. L.; Wu, F.; Xiao, Z.; Kerner, R. A.; Lin, Y. L.; Scholes, G. D.; Yao, N.; Rand, B. P. In Situ Preparation of Metal Halide Perovskite Nanocrystal Thin Films for Improved Light-Emitting Devices. *ACS Nano* **2017**, *11*, 3957.
(153) Cho, H.; Jeong, S.-H.; Park, M.-H.; Kim, Y.-H.; Wolf, C.; Lee, C.-L.; Heo, J. H.; Sadhanala, A.; Myoung, N.; Yoo, S.; et al. Overcoming the Electroluminescence Efficiency Limitations of Perovskite Light-Emitting Diodes. *Science* **2015**, *350*, 1222−1225.
(154) Lee, S.; Park, J. H.; Nam, Y. S.; Lee, B. R.; Zhao, B.; Di Nuzzo, D.; Jung, E. D.; Jeon, H.; Kim, J.-Y.; Jeong, H. Y.; Friend, R. H.; Song, M. H. Growth of Nanosized Single Crystals for Efficient Perovskite Light-Emitting Diodes. *ACS Nano* **2018**, *12*, 3417−3423.
(155) Yan, F.; Xing, J.; Xing, G.; Quan, L. N.; Tan, S. T.; Zhao, J.; Su, R.; Zhang, L.; Chen, S.; Zhao, Y.; Huan, A.; Sargent, E. H.; Xiong, Q.; Demir, H. V. Highly Efficient Visible Colloidal Lead-Halide Perovskite Nanocrystal Light-Emitting Diodes. *Nano Lett.* **2018**, *18*, 3157.
(156) Zou, Y.; Huang, Q.; Yang, Y.; Ban, M.; Li, S.; Han, Y.; Wu, T.; Tan, Y.; Gao, X.; Song, T.; Sun, B. Efficient Perovskite Light-Emitting Diodes Via Tuning Nanoplatelet Distribution and Crystallinity Orientation. *Adv. Mater. Interfaces* **2018**, *5*, 1801030.
(157) Yang, X.; Zhang, X.; Deng, J.; Chu, Z.; Jiang, Q.; Meng, J.; Wang, P.; Zhang, L.; Yin, Z.; You, J. Efficient Green Light-Emitting Diodes Based on Quasi-Two-Dimensional Composition and Phase Engineered Perovskite with Surface Passivation. *Nat. Commun.* **2018**, *9*, 570.
(158) Cheng, L. P.; Huang, J. S.; Shen, Y.; Li, G. P.; Liu, X. K.; Li, W.; Wang, Y. H.; Li, Y. Q.; Jiang, Y.; Gao, F.; Lee, C.-S.; Tang, J.-X. Efficient Cspbbr3 Perovskite Light-Emitting Diodes Enabled by Synergetic Morphology Control. *Adv. Opt. Mater.* **2019**, *7*, 1801534.
(159) Ban, M.; Zou, Y.; Rivett, J. P.; Yang, Y.; Thomas, T. H.; Tan, Y.; Song, T.; Gao, X.; Credgington, D.; Deschler, F.; Sirringhaus, H.; Sun, B. Solution-Processed Perovskite Light Emitting Diodes with Efficiency Exceeding 15% through Additive-Controlled Nanostructure Tailoring. *Nat. Commun.* **2018**, *9*, 3892.
(160) Yuan, S.; Wang, Z. K.; Zhuo, M. P.; Tian, Q. S.; Jin, Y.; Liao, L. S. Self-Assembled High Quality Cspbbr3 Quantum Dot Films toward Highly Efficient Light-Emitting Diodes. *ACS Nano* **2018**, *12*, 9541−9548.
(161) Song, J. Z.; Fang, T.; Li, J. H.; Xu, L. M.; Zhang, F. J.; Han, B. N.; Shan, Q. S.; Zeng, H. B. Organic-Inorganic Hybrid Passivation Enables Perovskite Qleds with an Eqe of 16.48%. *Adv. Mater.* **2018**, *30*, 1805409.
(162) Lin, K.; Xing, J.; Quan, L. N.; de Arquer, F. P. G.; Gong, X.; Lu, J.; Xie, L.; Zhao, W.; Zhang, D.; Yan, C.; Li, W.; Liu, X.; Lu, Y.; Kirman, J.; Sargent, E. H.; Xiong, Q.; Wei, Z. Perovskite Light-Emitting Diodes with External Quantum Efficiency Exceeding 20 Per Cent. *Nature* **2018**, *562*, 245−248.
(163) Li, G.; Rivarola, F. W. R.; Davis, N. J.; Bai, S.; Jellicoe, T. C.; de la Peña, F.; Hou, S.; Ducati, C.; Gao, F.; Friend, R. H.; Greenham, N. C.; Tan, Z.-K. Highly Efficient Perovskite Nanocrystal Light-Emitting Diodes Enabled by a Universal Crosslinking Method. *Adv. Mater.* **2016**, *28*, 3528−3534.
(164) Qasim, K.; Wang, B.; Zhang, Y.; Li, P.; Wang, Y.; Li, S.; Lee, S. T.; Liao, L. S.; Lei, W.; Bao, Q. Solution-Processed Extremely Efficient Multicolor Perovskite Light-Emitting Diodes Utilizing Doped Electron Transport Layer. *Adv. Funct. Mater.* **2017**, *27*, 1606874.
(165) Lu, M.; Zhang, X.; Bai, X.; Wu, H.; Shen, X.; Zhang, Y.; Zhang, W.; Zheng, W.; Song, H.; Yu, W. W.; et al. Spontaneous Silver Doping and Surface Passivation of Cspbi3 Perovskite Active Layer Enable Light-Emitting Devices with an External Quantum Efficiency of 11.2. *ACS Energy Lett.* **2018**, *3*, 1571−1577.
(166) Lu, M.; Zhang, X. Y.; Zhang, Y.; Guo, J.; Shen, X. Y.; Yu, W. W.; Rogach, A. L. Simultaneous Strontium Doping and Chlorine Surface Passivation Improve Luminescence Intensity and Stability of Cspbi3 Nanocrystals Enabling Efficient Light-Emitting Devices. *Adv. Mater.* **2018**, *30*, 1804691.
(167) Chiba, T.; Hayashi, Y.; Ebe, H.; Hoshi, K.; Sato, J.; Sato, S.; Pu, Y. J.; Ohisa, S.; Kido, J. Anion-Exchange Red Perovskite Quantum Dots with Ammonium Iodine Salts for Highly Efficient Light-Emitting Devices. *Nat. Photonics* **2018**, *12*, 681−687.
(168) Tan, Z.-K.; Moghaddam, R. S.; Lai, M. L.; Docampo, P.; Higler, R.; Deschler, F.; Price, M.; Sadhanala, A.; Pazos, L. M.; Credgington, D.; Hanusch, F.; Bein, T.; Snaith, H. J.; Friend, R. H. Bright Light-Emitting Diodes Based on Organometal Halide Perovskite. *Nat. Nanotechnol.* **2014**, *9*, 687−692.
(169) Wang, J.; Wang, N.; Jin, Y.; Si, J.; Tan, Z. K.; Du, H.; Cheng, L.; Dai, X.; Bai, S.; He, H.; Ye, Z.; Lai, M. L.; Friend, R. H.; Huang, W. Interfacial Control toward Efficient and Low-Voltage Perovskite Light-Emitting Diodes. *Adv. Mater.* **2015**, *27*, 2311−2316.

DOI: 10.1021/acs.chemrev.9b00107
Chem. Rev. 2019, 119, 7444−7477

(170) Yuan, M.; Quan, L. N.; Comin, R.; Walters, G.; Sabatini, R.; Voznyy, O.; Hoogland, S.; Zhao, Y.; Beauregard, E. M.; Kanjanaboos, P.; Lu, Z.; Kim, D. H.; Sargent, E. H. Perovskite Energy Funnels for Efficient Light-Emitting Diodes. *Nat. Nanotechnol.* **2016**, *11*, 872−877.
(171) Cao, Y.; Wang, N.; Tian, H.; Guo, J.; Wei, Y.; Chen, H.; Miao, Y.; Zou, W.; Pan, K.; He, Y.; et al. Perovskite Light-Emitting Diodes Based on Spontaneously Formed Submicrometre-Scale Structures. *Nature* **2018**, *562*, 249−253.
(172) Xu, W.; Hu, Q.; Bai, S.; Bao, C.; Miao, Y.; Yuan, Z.; Borzda, T.; Barker, A. J.; Tyukalova, E.; Hu, Z.; Kawecki, M.; Wang, H.; Yan, Z.; Liu, X.; Shi, X.; Uvdal, K.; Fahlman, M.; Zhang, W.; Duchamp, M.; Liu, J.-M.; Petrozza, A.; Wang, J.; Liu, L.-M.; Huang, W.; Gao, F. Rational Molecular Passivation for High-Performance Perovskite Light-Emitting Diodes. *Nat. Photonics* **2019**, DOI: 10.1038/s41566-019-0390-x.
(173) Wood, V.; Bulović, V. Colloidal Quantum Dot Light-Emitting Devices. *Nano Rev.* **2010**, *1*, 5202.
(174) Zhao, L.; Rolston, N.; Lee, K. M.; Zhao, X.; Reyes-Martinez, M. A.; Tran, N. L.; Yeh, Y. W.; Yao, N.; Scholes, G. D.; Loo, Y. L.; Selloni, A.; Dauskardt, R. H.; Rand, B. P. Influence of Bulky Organo-Ammonium Halide Additive Choice on the Flexibility and Efficiency of Perovskite Light-Emitting Devices. *Adv. Funct. Mater.* **2018**, *28*, 1802060.
(175) Dai, X.; Zhang, Z.; Jin, Y.; Niu, Y.; Cao, H.; Liang, X.; Chen, L.; Wang, J.; Peng, X. Solution-Processed, High-Performance Light-Emitting Diodes Based on Quantum Dots. *Nature* **2014**, *515*, 96−99.
(176) Zeng, W.; Lai, H. Y.; Lee, W. K.; Jiao, M.; Shiu, Y. J.; Zhong, C.; Gong, S.; Zhou, T.; Xie, G.; Sarma, M.; Wong, K.-T.; Wu, C.-C.; Yang, C. Achieving Nearly 30% External Quantum Efficiency for Orange−Red Organic Light Emitting Diodes by Employing Thermally Activated Delayed Fluorescence Emitters Composed of 1, 8-Naphthalimide-Acridine Hybrids. *Adv. Mater.* **2018**, *30*, 1704961.
(177) Yang, Y.; Zheng, Y.; Cao, W.; Titov, A.; Hyvonen, J.; Manders, J. R.; Xue, J.; Holloway, P. H.; Qian, L. High-Efficiency Light-Emitting Devices Based on Quantum Dots with Tailored Nanostructures. *Nat. Photonics* **2015**, *9*, 259−266.
(178) Di, D.; Romanov, A. S.; Yang, L.; Richter, J. M.; Rivett, J. P.; Jones, S.; Thomas, T. H.; Abdi Jalebi, M.; Friend, R. H.; Linnolahti, M.; Bochmann, M.; Credgington, D. High-Performance Light-Emitting Diodes Based on Carbene-Metal-Amides. *Science* **2017**, *356*, 159−163.
(179) Xing, J.; Zhao, Y.; Askerka, M.; Quan, L. N.; Gong, X.; Zhao, W.; Zhao, J.; Tan, H.; Long, G.; Gao, L.; Yang, Z.; Voznyy, O.; Tang, J.; Lu, Z.-H.; Xiong, Q.; Sargent, E. H. Color-Stable Highly Luminescent Sky-Blue Perovskite Light-Emitting Diodes. *Nat. Commun.* **2018**, *9*, 3541.
(180) Lee, C. W.; Lee, J. Y. Above 30% External Quantum Efficiency in Blue Phosphorescent Organic Light-Emitting Diodes Using Pyrido [2, 3-B] Indole Derivatives as Host Materials. *Adv. Mater.* **2013**, *25*, 5450−5454.
(181) Zhao, L.; Yeh, Y. W.; Tran, N. L.; Wu, F.; Xiao, Z.; Kerner, R. A.; Lin, Y. L.; Scholes, G. D.; Yao, N.; Rand, B. P. In Situ Preparation of Metal Halide Perovskite Nanocrystal Thin Films for Improved Light-Emitting Devices. *ACS Nano* **2017**, *11*, 3957−3964.
(182) *Universal Display Corporation*; Universal Display Corporation, 2018; http://www.udcoled.com/ (accessed April 3, 2019).
(183) Morgan, N. Y.; Leatherdale, C.; Drndić, M.; Jarosz, M. V.; Kastner, M. A.; Bawendi, M. Electronic Transport in Films of Colloidal Cdse Nanocrystals. *Phys. Rev. B: Condens. Matter Mater. Phys.* **2002**, *66*, 075339.
(184) Lee, J.; Sundar, V. C.; Heine, J. R.; Bawendi, M. G.; Jensen, K. F. Full Color Emission from Ii−Vi Semiconductor Quantum Dot−Polymer Composites. *Adv. Mater.* **2000**, *12*, 1102−1105.
(185) Wood, V.; Panzer, M. J.; Chen, J.; Bradley, M. S.; Halpert, J. E.; Bawendi, M. G.; Bulović, V. Inkjet-Printed Quantum Dot−Polymer Composites for Full-Color Ac-Driven Displays. *Adv. Mater.* **2009**, *21*, 2151−2155.
(186) Kagan, C.; Murray, C.; Bawendi, M. Long-Range Resonance Transfer of Electronic Excitations in Close-Packed Cdse Quantum-Dot Solids. *Phys. Rev. B: Condens. Matter Mater. Phys.* **1996**, *54*, 8633.
(187) Borchardt, J. K. Developments in Organic Displays. *Mater. Today* **2004**, *7*, 42−46.
(188) Reineke, S.; Lindner, F.; Schwartz, G.; Seidler, N.; Walzer, K.; Lüssem, B.; Leo, K. White Organic Light-Emitting Diodes with Fluorescent Tube Efficiency. *Nature* **2009**, *459*, 234−238.
(189) Kabra, D.; Lu, L. P.; Song, M. H.; Snaith, H. J.; Friend, R. H. Efficient Single-Layer Polymer Light-Emitting Diodes. *Adv. Mater.* **2010**, *22*, 3194−3198.
(190) Shimada, Y.; Ishino, J.; Shirasaki, S.; Irie, T.; Kikuchi, A. Effect of Mgzno-Bilayer/Ba-Ch3 Combination Interlayer on Emission Characteristics of Moo3/F8bt/Zno Hybrid Light Emitting Diodes Fabricated on Zno/Ag/Zno Transparent Cathode. *Displays* **2013**, *34*, 437−441.
(191) Bharathan, J.; Yang, Y. Polymer Electroluminescent Devices Processed by Inkjet Printing: I. Polymer Light-Emitting Logo. *Appl. Phys. Lett.* **1998**, *72*, 2660−2662.
(192) Aziz, H.; Popovic, Z. D.; Hu, N.-X.; Hor, A.-M.; Xu, G. Degradation Mechanism of Small Molecule-Based Organic Light-Emitting Devices. *Science* **1999**, *283*, 1900−1902.
(193) Cho, H.; Kim, Y. H.; Wolf, C.; Lee, H. D.; Lee, T. W. Improving the Stability of Metal Halide Perovskite Materials and Light-Emitting Diodes. *Adv. Mater.* **2018**, *30*, 1704587.
(194) Arora, N.; Dar, M. I.; Hinderhofer, A.; Pellet, N.; Schreiber, F.; Zakeeruddin, S. M.; Grätzel, M. Perovskite Solar Cells with Cuscn Hole Extraction Layers Yield Stabilized Efficiencies Greater Than 20%. *Science* **2017**, *358*, 768−771.
(195) Bryant, D.; Aristidou, N.; Pont, S.; Sanchez-Molina, I.; Chotchunangatchaval, T.; Wheeler, S.; Durrant, J. R.; Haque, S. A. Light and Oxygen Induced Degradation Limits the Operational Stability of Methylammonium Lead Triiodide Perovskite Solar Cells. *Energy Environ. Sci.* **2016**, *9*, 1655−1660.
(196) Eames, C.; Frost, J. M.; Barnes, P. R.; O'regan, B. C.; Walsh, A.; Islam, M. S. Ionic Transport in Hybrid Lead Iodide Perovskite Solar Cells. *Nat. Commun.* **2015**, *6*, 7497.
(197) Ahn, N.; Kwak, K.; Jang, M. S.; Yoon, H.; Lee, B. Y.; Lee, J.-K.; Pikhitsa, P. V.; Byun, J.; Choi, M. Trapped Charge-Driven Degradation of Perovskite Solar Cells. *Nat. Commun.* **2016**, *7*, 13422.
(198) Aristidou, N.; Eames, C.; Sanchez-Molina, I.; Bu, X.; Kosco, J.; Islam, M. S.; Haque, S. A. Fast Oxygen Diffusion and Iodide Defects Mediate Oxygen-Induced Degradation of Perovskite Solar Cells. *Nat. Commun.* **2017**, *8*, 15218.
(199) Fan, Z.; Xiao, H.; Wang, Y.; Zhao, Z.; Lin, Z.; Cheng, H.-C.; Lee, S.-J.; Wang, G.; Feng, Z.; Goddard, W. A., III; Huang, Y.; Duan, X. Layer-by-Layer Degradation of Methylammonium Lead Tri-Iodide Perovskite Microplates. *Joule* **2017**, *1*, 548−562.
(200) Niu, G.; Li, W.; Meng, F.; Wang, L.; Dong, H.; Qiu, Y. Study on the Stability of Ch3nh3pbi3 Films and the Effect of Post-Modification by Aluminum Oxide in All-Solid-State Hybrid Solar Cells. *J. Mater. Chem. A* **2014**, *2*, 705−710.
(201) Burschka, J.; Pellet, N.; Moon, S.-J.; Humphry-Baker, R.; Gao, P.; Nazeeruddin, M. K.; Grätzel, M. Sequential Deposition as a Route to High-Performance Perovskite-Sensitized Solar Cells. *Nature* **2013**, *499*, 316−319.
(202) Zhang, L.; Ju, M.-G.; Liang, W. The Effect of Moisture on the Structures and Properties of Lead Halide Perovskites: A First-Principles Theoretical Investigation. *Phys. Chem. Chem. Phys.* **2016**, *18*, 23174−23183.
(203) Habisreutinger, S. N.; Leijtens, T.; Eperon, G. E.; Stranks, S. D.; Nicholas, R. J.; Snaith, H. J. Carbon Nanotube/Polymer Composites as a Highly Stable Hole Collection Layer in Perovskite Solar Cells. *Nano Lett.* **2014**, *14*, 5561−5568.
(204) Ahn, N.; Kwak, K.; Jang, M. S.; Yoon, H.; Lee, B. Y.; Lee, J. K.; Pikhitsa, P. V.; Byun, J.; Choi, M. Trapped Charge-Driven Degradation of Perovskite Solar Cells. *Nat. Commun.* **2016**, *7*, 13422.

DOI: 10.1021/acs.chemrev.9b00107
Chem. Rev. 2019, 119, 7444−7477

(205) Galisteo-López, J. F.; Anaya, M.; Calvo, M.; Míguez, H. Environmental Effects on the Photophysics of Organic−Inorganic Halide Perovskites. *J. Phys. Chem. Lett.* **2015**, *6*, 2200−2205.
(206) Stranks, S. D.; Burlakov, V. M.; Leijtens, T.; Ball, J. M.; Goriely, A.; Snaith, H. J. Recombination Kinetics in Organic-Inorganic Perovskites: Excitons, Free Charge, and Subgap States. *Phys. Rev. Appl.* **2014**, *2*, 034007.
(207) Christians, J. A.; Miranda Herrera, P. A.; Kamat, P. V. Transformation of the Excited State and Photovoltaic Efficiency of Ch3nh3pbi3 Perovskite Upon Controlled Exposure to Humidified Air. *J. Am. Chem. Soc.* **2015**, *137*, 1530−1538.
(208) Gottesman, R.; Haltzi, E.; Gouda, L.; Tirosh, S.; Bouhadana, Y.; Zaban, A.; Mosconi, E.; De Angelis, F. Extremely Slow Photoconductivity Response of Ch3nh3pbi3 Perovskites Suggesting Structural Changes under Working Conditions. *J. Phys. Chem. Lett.* **2014**, *5*, 2662−2669.
(209) Merdasa, A.; Bag, M.; Tian, Y.; Källman, E.; Dobrovolsky, A.; Scheblykin, I. G. Super-Resolution Luminescence Microspectroscopy Reveals the Mechanism of Photoinduced Degradation in Ch3nh3pbi3 Perovskite Nanocrystals. *J. Phys. Chem. C* **2016**, *120*, 10711−10719.
(210) Yuan, Y.; Huang, J. Ion Migration in Organometal Trihalide Perovskite and Its Impact on Photovoltaic Efficiency and Stability. *Acc. Chem. Res.* **2016**, *49*, 286−293.
(211) Lee, S.; Park, J. H.; Lee, B. R.; Jung, E. D.; Yu, J. C.; Di Nuzzo, D.; Friend, R. H.; Song, M. H. Amine-Based Passivating Materials for Enhanced Optical Properties and Performance of Organic−Inorganic Perovskites in Light-Emitting Diodes. *J. Phys. Chem. Lett.* **2017**, *8*, 1784−1792.
(212) Back, H.; Kim, G.; Kim, J.; Kong, J.; Kim, T. K.; Kang, H.; Kim, H.; Lee, J.; Lee, S.; Lee, K. Achieving Long-Term Stable Perovskite Solar Cells Via Ion Neutralization. *Energy Environ. Sci.* **2016**, *9*, 1258−1263.
(213) Besleaga, C.; Abramiuc, L. E.; Stancu, V.; Tomulescu, A. G.; Sima, M.; Trinca, L.; Plugaru, N.; Pintilie, L.; Nemnes, G. A.; Iliescu, M.; Svavarsson, H. G.; Manolescu, A.; Pintilie, I. Iodine Migration and Degradation of Perovskite Solar Cells Enhanced by Metallic Electrodes. *J. Phys. Chem. Lett.* **2016**, *7*, 5168−5175.
(214) Zhao, L.; Kerner, R. A.; Xiao, Z.; Lin, Y. L.; Lee, K. M.; Schwartz, J.; Rand, B. P. Redox Chemistry Dominates the Degradation and Decomposition of Metal Halide Perovskite Optoelectronic Devices. *ACS Energy Lett.* **2016**, *1*, 595−602.
(215) Carrillo, J.; Guerrero, A.; Rahimnejad, S.; Almora, O.; Zarazua, I.; Mas-Marza, E.; Bisquert, J.; Garcia-Belmonte, G. Ionic Reactivity at Contacts and Aging of Methylammonium Lead Triiodide Perovskite Solar Cells. *Adv. Energy Mater.* **2016**, *6*, 1502246.
(216) Li, J.; Shan, X.; Bade, S. G. R.; Geske, T.; Jiang, Q.; Yang, X.; Yu, Z. Single-Layer Halide Perovskite Light-Emitting Diodes with Sub-Band Gap Turn-on Voltage and High Brightness. *J. Phys. Chem. Lett.* **2016**, *7*, 4059−4066.
(217) Shan, X.; Li, J.; Chen, M.; Geske, T.; Bade, S. G. R.; Yu, Z. Junction Propagation in Organometal Halide Perovskite−Polymer Composite Thin Films. *J. Phys. Chem. Lett.* **2017**, *8*, 2412−2419.
(218) Wang, X.; Ling, Y.; Chiu, Y.-C.; Du, Y.; Barreda, J. L.; Perez-Orive, F.; Ma, B.; Xiong, P.; Gao, H. Dynamic Electronic Junctions in Organic−Inorganic Hybrid Perovskites. *Nano Lett.* **2017**, *17*, 4831−4839.
(219) Diroll, B. T.; Nedelcu, G.; Kovalenko, M. V.; Schaller, R. D. High-Temperature Photoluminescence of Cspbx3 (X = Cl, Br, I) Nanocrystals. *Adv. Funct. Mater.* **2017**, *27*, 1606750.
(220) Tian, Y.; Zhou, C.; Worku, M.; Wang, X.; Ling, Y.; Gao, H.; Zhou, Y.; Miao, Y.; Guan, J.; Ma, B. Highly Efficient Spectrally Stable Red Perovskite Light-Emitting Diodes. *Adv. Mater.* **2018**, *30*, 1707093.
(221) Tsai, H.; Nie, W.; Blancon, J. C.; Stoumpos, C. C.; Soe, C. M. M.; Yoo, J.; Crochet, J.; Tretiak, S.; Even, J.; Sadhanala, A.; Azzellino, G.; Brenes, R.; Ajayan, P. M.; Bulović, V.; Stranks, S. D.; Friend, R. H.; Kanatzidis, M. G.; Mohite, A. D. Stable Light-Emitting Diodes Using Phase-Pure Ruddlesden−Popper Layered Perovskites. *Adv. Mater.* **2018**, *30*, 1704217.
(222) Kim, Y.-H.; Wolf, C.; Kim, H.; Lee, T.-W. Charge Carrier Recombination and Ion Migration in Metal-Halide Perovskite Nanoparticle Films for Efficient Light-Emitting Diodes. *Nano Energy* **2018**, *52*, 329−335.
(223) Sutherland, B. R.; Hoogland, S.; Adachi, M. M.; Kanjanaboos, P.; Wong, C. T.; McDowell, J. J.; Xu, J.; Voznyy, O.; Ning, Z.; Houtepen, A. J.; Sargent, E. H. Perovskite Thin Films Via Atomic Layer Deposition. *Adv. Mater.* **2015**, *27*, 53−58.
(224) Xing, G.; Mathews, N.; Lim, S. S.; Yantara, N.; Liu, X.; Sabba, D.; Grätzel, M.; Mhaisalkar, S.; Sum, T. C. Low-Temperature Solution-Processed Wavelength-Tunable Perovskites for Lasing. *Nat. Mater.* **2014**, *13*, 476−480.
(225) Sutherland, B. R.; Hoogland, S.; Adachi, M. M.; Wong, C. T.; Sargent, E. H. Conformal Organohalide Perovskites Enable Lasing on Spherical Resonators. *ACS Nano* **2014**, *8*, 10947−10952.
(226) Stranks, S. D.; Wood, S. M.; Wojciechowski, K.; Deschler, F.; Saliba, M.; Khandelwal, H.; Patel, J. B.; Elston, S. J.; Herz, L. M.; Johnston, M. B.; Schenning, A. P. H. J.; Debije, M. G.; Riede, M. K.; Morris, S. M.; Snaith, H. J. Enhanced Amplified Spontaneous Emission in Perovskites Using a Flexible Cholesteric Liquid Crystal Reflector. *Nano Lett.* **2015**, *15*, 4935−4941.
(227) Kao, T. S.; Chou, Y.-H.; Chou, C.-H.; Chen, F.-C.; Lu, T.-C. Lasing Behaviors Upon Phase Transition in Solution-Processed Perovskite Thin Films. *Appl. Phys. Lett.* **2014**, *105*, 231108.
(228) Yakunin, S.; Protesescu, L.; Krieg, F.; Bodnarchuk, M. I.; Nedelcu, G.; Humer, M.; De Luca, G.; Fiebig, M.; Heiss, W.; Kovalenko, M. V. Low-Threshold Amplified Spontaneous Emission and Lasing from Colloidal Nanocrystals of Caesium Lead Halide Perovskites. *Nat. Commun.* **2015**, *6*, 8056.
(229) Wang, Y.; Li, X.; Song, J.; Xiao, L.; Zeng, H.; Sun, H. All-Inorganic Colloidal Perovskite Quantum Dots: A New Class of Lasing Materials with Favorable Characteristics. *Adv. Mater.* **2015**, *27*, 7101−7108.
(230) Pan, J.; Sarmah, S. P.; Murali, B.; Dursun, I.; Peng, W.; Parida, M. R.; Liu, J.; Sinatra, L.; Alyami, N.; Zhao, C.; Alarousu, E.; Ng, T. K.; Ooi, B. S.; Bakr, O. M.; Mohammed, O. F. Air-Stable Surface-Passivated Perovskite Quantum Dots for Ultra-Robust, Single-and Two-Photon-Induced Amplified Spontaneous Emission. *J. Phys. Chem. Lett.* **2015**, *6*, 5027−5033.
(231) Eaton, S. W.; Lai, M.; Gibson, N. A.; Wong, A. B.; Dou, L.; Ma, J.; Wang, L.-W.; Leone, S. R.; Yang, P. Lasing in Robust Cesium Lead Halide Perovskite Nanowires. *Proc. Natl. Acad. Sci. U. S. A.* **2016**, *113*, 1993−1998.
(232) Klimov, V. I. Spectral and Dynamical Properties of Multiexcitons in Semiconductor Nanocrystals. *Annu. Rev. Phys. Chem.* **2007**, *58*, 635−673.
(233) Yuan, F.; Wu, Z.; Dong, H.; Xi, J.; Xi, K.; Divitini, G.; Jiao, B.; Hou, X.; Wang, S.; Gong, Q. High Stability and Ultralow Threshold Amplified Spontaneous Emission from Formamidinium Lead Halide Perovskite Films. *J. Phys. Chem. C* **2017**, *121*, 15318−15325.
(234) Fu, Y.; Zhu, H.; Schrader, A. W.; Liang, D.; Ding, Q.; Joshi, P.; Hwang, L.; Zhu, X. Y.; Jin, S. Nanowire Lasers of Formamidinium Lead Halide Perovskites and Their Stabilized Alloys with Improved Stability. *Nano Lett.* **2016**, *16*, 1000−1008.
(235) Shum, K.; Chen, Z.; Qureshi, J.; Yu, C.; Wang, J. J.; Pfenninger, W.; Vockic, N.; Midgley, J.; Kenney, J. T. Synthesis and Characterization of Cssni3 Thin Films. *Appl. Phys. Lett.* **2010**, *96*, 221903.
(236) Chung, I.; Lee, B.; He, J.; Chang, R. P. H.; Kanatzidis, M. G. All-Solid-State Dye-Sensitized Solar Cells with High Efficiency. *Nature* **2012**, *485*, 486−489.
(237) Huang, L.-y.; Lambrecht, W. R. Electronic Band Structure, Phonons, and Exciton Binding Energies of Halide Perovskites Cssncl3, Cssnbr3, and Cssni3. *Phys. Rev. B: Condens. Matter Mater. Phys.* **2013**, *88*, 165203.
(238) Hao, F.; Stoumpos, C. C.; Cao, D. H.; Chang, R. P.; Kanatzidis, M. G. Lead-Free Solid-State Organic−Inorganic Halide Perovskite Solar Cells. *Nat. Photonics* **2014**, *8*, 489−494.

DOI: 10.1021/acs.chemrev.9b00107
Chem. Rev. 2019, 119, 7444−7477

(239) Chong, W. K.; Thirumal, K.; Giovanni, D.; Goh, T. W.; Liu, X.; Mathews, N.; Mhaisalkar, S.; Sum, T. C. Dominant Factors Limiting the Optical Gain in Layered Two-Dimensional Halide Perovskite Thin Films. *Phys. Chem. Chem. Phys.* **2016**, *18*, 14701−14708.
(240) Li, M.; Wei, Q.; Muduli, S. K.; Yantara, N.; Xu, Q.; Mathews, N.; Mhaisalkar, S. G.; Xing, G.; Sum, T. C. Enhanced Exciton and Photon Confinement in Ruddlesden−Popper Perovskite Microplatelets for Highly Stable Low-Threshold Polarized Lasing. *Adv. Mater.* **2018**, *30*, 1707235.
(241) Zhu, H.; Fu, Y.; Meng, F.; Wu, X.; Gong, Z.; Ding, Q.; Gustafsson, M. V.; Trinh, M. T.; Jin, S.; Zhu, X. Y. Lead Halide Perovskite Nanowire Lasers with Low Lasing Thresholds and High Quality Factors. *Nat. Mater.* **2015**, *14*, 636−642.
(242) Zhang, Q.; Ha, S. T.; Liu, X.; Sum, T. C.; Xiong, Q. Room-Temperature near-Infrared High-Q Perovskite Whispering-Gallery Planar Nanolasers. *Nano Lett.* **2014**, *14*, 5995−6001.
(243) Liao, Q.; Hu, K.; Zhang, H.; Wang, X.; Yao, J.; Fu, H. Perovskite Microdisk Microlasers Self-Assembled from Solution. *Adv. Mater.* **2015**, *27*, 3405−3410.
(244) Jia, Y.; Kerner, R. A.; Grede, A. J.; Brigeman, A. N.; Rand, B. P.; Giebink, N. C. Diode-Pumped Organo-Lead Halide Perovskite Lasing in a Metal-Clad Distributed Feedback Resonator. *Nano Lett.* **2016**, *16*, 4624−4629.
(245) Saliba, M.; Wood, S. M.; Patel, J. B.; Nayak, P. K.; Huang, J.; Alexander-Webber, J. A.; Wenger, B.; Stranks, S. D.; Horantner, M. T.; Wang, J. T.; et al. Structured Organic-Inorganic Perovskite toward a Distributed Feedback Laser. *Adv. Mater.* **2016**, *28*, 923−929.
(246) Chen, S.; Zhang, C.; Lee, J.; Han, J.; Nurmikko, A. High-Q, Low-Threshold Monolithic Perovskite Thin-Film Vertical-Cavity Lasers. *Adv. Mater.* **2017**, *29*, 1604781.
(247) Jia, Y.; Kerner, R. A.; Grede, A. J.; Rand, B. P.; Giebink, N. C. Continuous-Wave Lasing in an Organic−Inorganic Lead Halide Perovskite Semiconductor. *Nat. Photonics* **2017**, *11*, 784−788.
(248) Gong, X.; Voznyy, O.; Jain, A.; Liu, W.; Sabatini, R.; Piontkowski, Z.; Walters, G.; Bappi, G.; Nokhrin, S.; Bushuyev, O.; Yuan, M.; Comin, R.; McCamant, D.; Kelley, S. O.; Sargent, E. H. Electron−Phonon Interaction in Efficient Perovskite Blue Emitters. *Nat. Mater.* **2018**, *17*, 550−556.

DOI: 10.1021/acs.chemrev.9b00107
Chem. Rev. 2019, 119, 7444−7477